

University of Alberta

Reynolds Number and Jet Turbulence Effects on Plume Trajectory

by

Khurrum Shahzad



A thesis submitted to the Faculty of Graduate Studies and Research in partial fulfillment
of the requirements for the degree of Master of Science

Department of Mechanical Engineering

Edmonton, Alberta
Fall 2002



National Library
of Canada

Acquisitions and
Bibliographic Services

395 Wellington Street
Ottawa ON K1A 0N4
Canada

Bibliothèque nationale
du Canada

Acquisitions et
services bibliographiques

395, rue Wellington
Ottawa ON K1A 0N4
Canada

Your file *Votre référence*

Our file *Notre référence*

The author has granted a non-exclusive licence allowing the National Library of Canada to reproduce, loan, distribute or sell copies of this thesis in microform, paper or electronic formats.

The author retains ownership of the copyright in this thesis. Neither the thesis nor substantial extracts from it may be printed or otherwise reproduced without the author's permission.

L'auteur a accordé une licence non exclusive permettant à la Bibliothèque nationale du Canada de reproduire, prêter, distribuer ou vendre des copies de cette thèse sous la forme de microfiche/film, de reproduction sur papier ou sur format électronique.

L'auteur conserve la propriété du droit d'auteur qui protège cette thèse. Ni la thèse ni des extraits substantiels de celle-ci ne doivent être imprimés ou autrement reproduits sans son autorisation.

0-612-81472-6

University of Alberta

Library Release Form

Name of Author: Khurram Shahzad

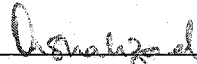
Title of Thesis: Reynolds number and jet turbulence effects on plume trajectory

Degree: Master of Science

Year this Degree Granted: 2002

Permission is hereby granted to the University of Alberta to reproduce single copies of this thesis and to lend or sell such copies for private, scholarly, or scientific research purposes only.

The author reserves all other publication and other rights in association with the copyright in the thesis, and except as herein before provided, neither the thesis nor any substantial portion thereof may be printed or otherwise reproduced in any material from whatever without the author's prior written permission.



Khurram Shahzad
440-RH, Michener Park
Edmonton, Alberta
Canada T6H 4M5

Date: May 03, 2002

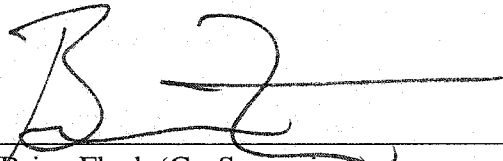
University of Alberta

Faculty of Graduate Studies and Research

The undersigned certify that they have read, and recommend to the Faculty of Graduate Studies and Research for acceptance, a thesis entitled Reynolds Number and Jet Turbulence Effects on Plume Trajectory by Khurrum Shahzad in partial fulfillment of the requirements for the degree of Master of Science.



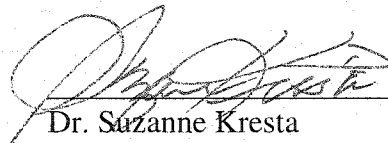
Dr. David J. Wilson (Supervisor)



Dr. Brian Fleck (Co-Supervisor)



Dr. Douglas J. Dale



Dr. Suzanne Kresta

Date: May 01, 2002

Abstract

It is important to know if modeling large systems on small-scale gives useful results in spite of the huge mismatch in Reynolds number. The primary objective of this research is to determine the Reynolds number effects on the plume trajectory from scaled-down water jets in a water channel cross-flow. A large scale and a small scale model of a vertical surface jet from turbulent source were designed and tested over a wide range of Reynolds numbers. The results show that from Reynolds number 200 to 4000 there is about a 40% increase in the entrainment coefficient, whereas from Reynolds number 4000 to 10000 the increase in entrainment coefficient is only 2%. At the higher Reynolds number range, Reynolds number effects are negligible on the plume trajectory and at low Reynolds numbers entrainment coefficient is a strong function of Reynolds numbers. Reducing the initial turbulence in the jet without changing its velocity profile caused a less than one source diameter increase in the plume trajectory rise.

Contents

1	Introduction and Literature Review.....	1
1.1	Introduction.....	1
1.1.1	Reynolds number effects.....	1
1.1.2	Design of a turbulent jet source.....	3
2	Plume Rise and Downwash Models for a Vertical Surface Jet in Crossflow.....	5
2.1	Introduction.....	5
2.2	Plume rise equations.....	5
2.3	Trajectory-averaged entrainment coefficients.....	11
2.4	Added mass acceleration effects on entrainment coefficients.....	12
2.5	Downwash velocity correction.....	13
3	Water Channel Experiment Technique.....	22
3.1	Introduction.....	22
3.2	Water channel.....	22
3.2.1	Measuring jet exit velocity profiles.....	23
3.3	Velocity and turbulence intensity measurement.....	24
3.4	Titanium dioxide seeding.....	25
3.5	Experimental set up.....	25
3.5.1	Rotameter calibration.....	25
3.6	Jet trajectory measurement.....	26
3.7	Velocity profile measurements in the jet with no crossflow.....	27
3.8	Jet image acquisition system.....	28
3.8.1	Camera.....	28
3.8.2	Analog to digital conversion of video signals.....	29
3.9	Measurement of jet trajectory using laser induced fluorescence.....	29
3.9.1	Laser induced fluorescence.....	29
3.9.2	Dye tracer.....	30
3.9.3	Calibration images.....	31
3.9.4	Laser light attenuation through a plume.....	32
3.9.5	Accounting for light attenuation in concentration measurements.....	34
3.9.6	Selecting averaging time and trajectory for jet images.....	35

4	Design of a Turbulent Jet Source.....	53
4.1	Introduction.....	53
4.2	Source design.....	54
4.2.1	Inlet holes for turbulence generation	55
4.2.2	Jet symmetry	56
4.2.3	Jet turbulence intensity	57
4.3	Velocity profile shape correction for momentum flux	57
4.3.1	Direct numerical integration for momentum	58
4.3.2	Ramp profile integration for momentum	58
5	Modeling Reynolds Number Effects on Jet Source Turbulence.....	74
5.1	Introduction.....	74
5.2	A homogeneous mixing chamber model for turbulence intensity	74
5.2.1	Reynolds number behavior of dissipation model.....	75
5.2.2	Applying the dissipation model to mixing chamber	78
6	Comparison of plume rise model to the data	86
6.1	Introduction.....	86
6.2	Interrelation effects from Reynolds number, downwash, velocity ratio and entrainment coefficient on plume rise.....	87
6.3	Validation of measurement techniques.....	87
6.4	Effects of varying entrainment coefficient to predict plume trajectories.	88
6.5	Downwash velocity correction	89
6.6	Effects of entrainment coefficient on predicting plume trajectories with downwash correction	91
6.6.1	Reynolds number effects on entrainment coefficient	91
6.6.2	Reynolds number Effects on Plume Rise.....	92
6.6.3	Jet exit to crosswind velocity ratio effects on entrainment coefficient.....	93
6.6.4	Effects of initial turbulence on the plume trajectory	94
7	Summary, Conclusions and Recommendations.....	118
7.1	Summary and conclusions	118
7.1.1	Plume rise and downwash model.....	118
7.1.2	Experimental methods and techniques.....	119
7.1.3	Design of a turbulent jet source	119
7.1.4	Modeling Reynolds Number Effects on Jet Source Turbulence.....	120
7.1.5	Comparison of plume rise model to data	121
7.2	Recommendations.....	122

List of Tables

4.1	List of LDV Experiments.....	72
6.1	List of Flow Visualization Experiments.....	116

List of Figures

2.1	Schematic of the plume showing the characteristic parameters used in the plume rise equation.....	18
2.2	Continuous downwash velocity distribution along the plume. Downwash velocity W_d decreasing with x as rising plume increases space for entrainment into bottom of bent-over plume.....	19
2.3	At Section A (above), the jet is closer to the wall and a low pressure zone produces downwash as vortex roll up induces entrainment. At Section B (below), plume is far away from the wall and no low pressure zone is induced by vortex roll up.....	20
2.4	Connection of shed vortices back to a stack tip to produce stack wake downwash velocity W_d	21
3.1	Schematic view of the water channel facility, looking down through the free water surface.....	38
3.2	Schematic side view of the water channel with the jet set-up on the bottom of the channel for LDV measurements.....	39
3.3	Range of available jet Reynolds numbers corresponding to various source velocity to cross wind velocity ratios	40
3.4	Effect of averaging time on the LDV measurements of source exit velocity for the $d_s = 12.7$ mm source with	41
3.5	Mean velocity profiles measured with two different LDV systems. Source diameter $d_s = 12.7$ mm and $W_s = 270$ mm / s	42
3.6	Calibration curve for the largest rotameter tube R-8M-25-4F-D.....	43
3.7	Calibration curve for the medium rotameter tube R-8M-25-4F- I.....	44
3.8	Calibration curve for smaller rotameter tube R-6-15-B.....	45
3.9	Calibration curve for the smallest rotameter tube R-603.....	46
3.10	Water channel velocity profiles measured across the channel at three different heights.....	47
3.11	Water channel velocity profiles measured across the channel at three different heights.....	48
3.12 a,b	Contour profiles of average images for the $d_s = 12.7$ mm source, produced from a) 200, b) 1200 consecutive images.....	49
3.12 c,d	Contour profiles of average images for the $d_s = 12.7$ mm produced from c) 1800, d) 2400 consecutive images.....	50
3.13	Profiles produced from concentration and intensity images. The rise height of pixel size is 0.5 mm / pixel.....	51
3.14	concentration and contour profiles are shown together. Jet trajectory can be determined by joining the medians of	52
4.1	Mean velocity profile with exit nozzle diameter, $d_s = 25.4$ mm and 4:1 area contraction is non uniform compared to	61
4.2	Vertical sectional view of the source.....	62

4.3	Mean velocity profile of the jet with the conical center-body is more uniform than the mean velocity profile of the jet with the cross center-body. Source diameter $d_s = 12.7$ mm	63
4.4	Turbulence intensity at jet exit is higher with small diameter inlet holes in the mixing chamber, $d_m = 3.175$ mm	64
4.5	Mean velocity profiles are almost identical similar with and without an inlet plenum chamber. Source diameter $d_s = 12.7$ mm	65
4.6	Mean velocity profiles measured at four different planes above the source are similar, which means that the jet is symmetrical.....	66
4.7	Mean velocity profiles measured for several jet Reynolds numbers show a weak dependence on Reynolds number.....	67
4.8	Comparison of mean velocity profiles measured at $z/d_s = 1$ with large and small source.....	68
4.9	Mean velocity profiles measured with and without the exit damping screen are similar. Turbulence intensity is much lower with the screen in place.....	69
4.10	Ramp profile approximation for calculating of the momentum correction factor.....	70
4.11	Momentum correction factor values calculated with direct numerical integration method are closer to the expected values for a turbulent top hat profile.....	71
5.1	Turbulence kinetic energy and mass balance flow diagram for the mixing chamber upstream of the surface jet nozzle.....	82
5.2	Dependence of dissipation to the viscosity for this model compared to the DNS (direct numerical simulation) studies of forced (boundary layer) and decaying (grid) turbulent flows	83
5.3	Turbulence intensity variation with Jet Reynolds number using Equation 5.28 with	84
5.4	Enlarged view of the inlet holes with assumed flow separation at the exit of the large diameter holes producing an area.....	85
6.1	Repeatability of data measured at velocity ratio.....	95
6.2	Repeatability of data measured at velocity ratio, $M = 16$, with a 30 day interval between experiments	96
6.3	Large source comparison between the present study data on a surface jet and measurements of Johnston and Wilson (1997)	97
6.4	Large source comparison between experimental data and the momentum rise equation (Equation 2.21) with no downwash correction. β values are much too large if no downwash correction is used.....	98
6.5	Large source comparison between experimental data and the momentum rise equation (Equation 2.21) with no downwash correction. β values are much large if no downwash correction is used.....	99
6.6	Small source comparison between experimental data and the plume rise equation (Equation 2.21) with no downwash correction.	100
6.7	Comparison between experimental data and the plume rise equation with downwash correction (Equation 6.2).....	101

6.8	Comparison between experimental data and the plume rise equation with downwash correction (Equation 6.2).....	102
6.9	Comparison between experimental data and the plume rise equation with downwash correction (Equation 6.2).....	103
6.10	In the present study the downwash correction coefficient in Equation 2.50 increases exponentially with increasing velocity ratio.....	104
6.11	Large source comparison between experimental data and the plume rise equation with downwash correction (Equation 6.2),	105
6.12	Large source comparison between experimental data and the plume rise equation with downwash correction (Equation 6.2).....	106
6.13	Small source comparison between experimental data and the plume rise equation with downwash correction (Equation 6.2),	107
6.14	Small source comparison between experimental data and the plume rise equation with downwash correction (Equation 6.2),	108
6.15	Effect of Reynolds number on entrainment coefficient normalized by the high Reynolds entrainment coefficient β_{∞}	109
6.16	Plume rise height increases with the increase in the velocity ratio. The measured and predicted height	110
6.17	Effects of Reynolds number on plume rise.....	111
6.18	Entrainment coefficient decreases as velocity ratio M increase.....	112
6.19	Effects of jet turbulence on the plume trajectory.....	113
6.20	Effects of jet turbulence on the plume trajectory.....	114
6.21	Effects of jet turbulence on the plume trajectory.....	115

Symbols and Nomenclature

A_s	Area of the source, [mm ²]
B_1	Constant in plume downwash model
B_2	Constant in plume downwash model
B_3	Downwash coefficient
B_l	Length scale constant in mixing chamber model
$B_{inertia}$	Inertial constant in mixing chamber model
$B_{viscous}$	Viscous constant in mixing chamber model
C_c	Coefficient of area contraction
C_{cal}	Tracer dye concentration of fluorescent dye in calibration box, [mg/L]
C_{ij}	Tracer dye digital pixel concentration, [counts]
$C_{ij,cal}$	Tracer dye digital pixel concentration for calibration tests, [counts]
$C_{\Delta P}$	Near wake pressure coefficient behind emerging jet
C_s	Trace dye concentration at source, [mg/mm ³]
C_x	Trace dye concentration of plume at downwind distance x , [mg/mm ³]
d_{in}	Diameter of inlet holes into the mixing chamber, [mm]
d_{eff}	Effective diameter of inlet holes, [mm]
d_{plume}	Plume diameter at given distance x , [mm]
d_s	Exit diameter of the turbulent jet source, [mm]

F_m	Vertical momentum flux from the source, $[\text{mm}^4/\text{s}^2]$
G_{ij}	Gain factor for pixel ij , $[\text{mg/L/counts}]$
h	Total rise of the plume, $[\text{mm}]$
h_m	Plume rise height due to momentum, $[\text{mm}]$
h_{max}	Maximum plume rise at maximum Reynolds number, $[\text{mm}]$
$h _{\text{downwash}}$	Rise of the plume with downwash, $[\text{mm}]$
$h _{\text{no downwash}}$	Rise of the plume with no downwash, $[\text{mm}]$
$(I_{\text{back},ij})_{\text{camera}}$	Background camera intensity at each pixel, $[\text{counts}]$
$(I_{ij})_{\text{camera}}$	Camera intensity at each pixel, $[\text{counts}]$
$(I_{ij,C_0})_{\text{camera}}$	Camera intensity at each pixel with zero concentration, $[\text{counts}]$
$(I_{ij,C_{\text{cal}}})_{\text{camera}}$	Camera intensity at each pixel at a known concentration, $[\text{counts}]$
I_e	Laser light intensity at given position in the dye mixture, $[\text{W/mm}^2]$
I_0	Laser light intensity entering the fluorescent dye mixture, $[\text{W/mm}^2]$
l	Turbulence length scale of the large energetic eddies, $[\text{mm}]$
M	Density averaged velocity ratio between jet and crossflow
N_{in}	Number of inlet holes into the mixing chamber
n	Exponent of wake decay in downwash model
P_x	Wake pressure behind the jet at downstream distance x , $[\text{Pa}]$
P_{∞}	Pressure in undisturbed flow, $[\text{Pa}]$

\mathbb{P}	Production of turbulence kinetic energy, [W/kg]
Q_{in}	Volume flow into the mixing chamber, [mm ³ /s]
Q_{out}	Volume flow out of the source, [mm ³ /s]
Q_p	Plume volume flow rate, [mm ³ /s]
Q_{rot}	Rotameter flow rate, [ml/s]
R_0	Initial radius of fully bent over plume [mm]
R_p	Plume radius at given distance x , [mm]
R_s	Exit radius of the turbulent jet source, [mm]
Re_d	Reynolds number at jet exit, [$W_s d_s / \nu$]
Re_l	Reynolds number of turbulence, [$u_s l / \nu$]
Re_{λ_g}	Taylor's microscale Reynolds number, [$u_s \lambda_g / \nu$]
S_{rot}	Rotameter scale setting
t	Time, [s]
U_a	Ambient fluid velocity, [mm/s]
U_{in}	Velocity of the jets coming into the mixing chamber, [mm/s]
U, V, W	Mean velocities, [mm/s]
u', v', w'	RMS Velocities, [mm/s]
u, v, w	Fluctuating velocities about the means U, V, W , [mm/s]
u_s	Turbulence velocity scale, [mm/s]
V	Volume of the mixing chamber, [mm ³]

V_e	Entrainment Velocity, [mm/s]
W_s	Velocity of the jet coming out of the source, [mm/s]
W_0	Jet centreline velocity, [mm/s]
W_d	Plume downwash velocity, [mm/s]
W_p	Plume momentum rise velocity with no downwash, [mm/s]
x	Downstream distance, [mm]
y_{ij}	Distance travelled by laser sheet from the inner side of the water channel side wall to each pixel, [mm]
y_1	Distance between the Powell lens and the outer side of the water channel sidewall, [mm]
z	Distance above the source, [mm]
α_m	Momentum correction factor
β	Entrainment coefficient
β_∞	Entrainment coefficient at maximum Reynolds number
ε	Dissipation of turbulence kinetic energy, [W/kg]
ε_a	Attenuation coefficient for fluorescein, $[\text{mg/L}]^{-1} [\text{mm}]^{-1}$
$\varepsilon_{inertia}$	Dissipation of turbulence kinetic energy due to inertia, [W/kg]
$\varepsilon_{viscous}$	Dissipation of turbulence kinetic energy due to viscosity, [W/kg]
δ	Shear layer thickness, [mm]
Λ_f	Streamwise integral length scale of eddies, [mm]
λ_f	Streamwise turbulence Taylor microscale, [mm]

λ_g	Crossstream turbulence Taylor microscale, [mm]
ν	Kinematic viscosity, [mm ² /s]
ρ_a	Crossflow fluid density, [kg/mm ³]
ρ_p	Plume fluid density, [kg/mm ³]
ρ_s	Source fluid density, [kg/mm ³]
θ	Angle of the plume to the horizontal x axis, [degree]

Chapter 1

Introduction and Literature Review

1.1 Introduction

The jet in cross flow is a basic flowfield which is relevant to a wide variety of applications, such as plume dispersion, industrial mixing and emergency venting. One characteristic which received early attention was the determination of the jet trajectory. The problem of estimating the trajectory of turbulent plume in a cross flow arises in a number of practical applications. For example, while estimating the ground level concentration of the pollutants emitted from the stack or ground level source, it is important to know how rapidly the plume from a stack or ground level source rises and where it levels off.

1.1.1 Reynolds number effects

In developing engineering models all experiments are done on small-scale in wind tunnels or water channels. It is important to know if modeling large systems on a small-scale gives useful results in spite of the huge mismatch in Reynolds number. In the past, almost no work has been done to document the effects of jet exit Reynolds number on the trajectory of the bent-over surface jets. The current practice is to simply ignore the effect due to jet Reynolds number mismatch between scaled down models and full scale prototypes. The primary objective of the thesis research was to determine the Reynolds number effects on the plume trajectory from scaled-down water jets in a water channel crossflow. In order to study these effects, a large scale and a small scale model of a

ground level turbulent jet source were designed, built and tested over a wide range of Reynolds numbers in water channel experiments.

One of the first analytical studies dealing with entrainment in a rising plume was carried out by Morton, Taylor and Turner (1956), who introduced the concept of entrainment coefficient making the entrainment velocity proportional to the rate of plume rise. Since that time, most methods for modeling the rise of a plume have been developed. These models are based on the concept of an entrainment velocity constant of proportionality β between the local rate of plume rise dh/dt and the apparent "velocity" V_e at which ambient fluid mixes into the plume at that point in space. In this thesis, the objective is to study the Reynolds number and velocity ratio effects on β by using existing models to predict the plume trajectory. The plume rise model used was developed by Briggs (1975). His approach to derive the plume rise equation was used later by Weil (1988), Davidson (1989), Synder and Lawson (1991) and Johnston and Wilson (1997).

There have been a number of laboratory experiments on plumes and jets in a cross flow. Callahan and Ruggari (1951) studied the trajectory of a heated air jet discharging into a channel with a cross flow. Bryant and Cowdrey (1955) studied the trajectory of heated air plume in a wind tunnel. Keffer and Baines (1963), Pratte and Baines (1967), Hoehne and Luce (1970), Kamotani and Greber (1972) and Johnston and Wilson (1997) have shown that the main parameter influencing the trajectory and the entrainment coefficient β is the jet to cross flow velocity ratio. No one has yet determined the Reynolds number effects caused by the modeling large full-scale jets in small scale.

Kamotani & Gerber (1972) and Haniu & Ramaprian (1989) show that the trajectory obtained based on maximum local velocity is always higher than the corresponding scalar concentration trajectory. Smith and Mungal (1998) measured the trajectory based upon the local maximum mean concentration and not upon local velocity measurements. In their study, Johnston and Wilson (1997) also used the concentration measurements to determine the plume trajectory.

1.1.2 Design of a turbulent jet source

In order to study these effects, a model of a ground level turbulent source was designed for this study. The objective was to design a source with an easy reproducible inner geometry which would be easy to fabricate at any scale to produce the same jet exit profile and turbulence intensity regardless the size of the source and the flow rate. In previous studies, experiments were done using a round tube as a stack or a machined nozzle as a ground level source to produce a jet. Kamotani and Gerber (1972) injected a surface jet in the cross flow with a 6 mm diameter nozzle. Andreopoulos and Rodi (1984) studied the surface jets in a cross flow by producing a jet from a brass tube of 50 mm internal diameter. Alton et al. (1993) used round tubes of 5mm and 10mm diameter in their experiments to produce stack jet. Johnston and Wilson (1997) used a 8.8 mm inner diameter tube and an internal turbulence generator to produce a turbulent stack jet with a relatively flat exit velocity profile. Smith and Mungal (1998) in their study of surface jets in crossflow used a jet plenum arrangement with inside diameter of 16 cm and nozzle diameter varying from 2 mm to 20 mm. There are few reported details of the inner geometry and operating characteristic of these sources.

It would be interesting to know if the initial turbulence in a jet source could affect jet trajectory. With this in mind, the present study will use an exit screen to reduce the turbulence from the emerging jet without effecting the velocity profiles of the jet.

A simple mathematical model will be developed to predict the turbulence intensity in the jet coming out of the turbulent source and the values obtained from this model will be compared with the experimental data and also to some data available in the literature collected by Sreenivasan (1998).

Chapter 2

Plume Rise and Downwash Models for a Vertical Surface Jet in Crossflow

2.1 Introduction

One of the first analytical studies dealing with entrainment in a rising plume was carried out by Morton, Taylor and Turner (1956). Since that time, many different methods for modeling the rise of a plume have been developed. In this thesis, the object was to study the Reynolds number and velocity ratio effects using existing models to predict the plume trajectory. To account for the influence of the nearby surface on the jet, a downwash velocity correction model, with some modifications, developed by Johnston and Wilson (1997) was introduced in the plume rise equation.

2.2 Plume rise equations

The plume rise model for a momentum jet used in this thesis is the same model used by Briggs (1975). His approach to derive the plume rise equation was used by Weil (1988), Davidson (1989), Synder and Lawson (1991) and Johnston and Wilson (1997). Briggs' modeling of plume was based on the balance of mass and momentum through a cylindrical plume element. The model includes several key approximations.

- The plume is "fully bent-over" with its axis parallel to wind direction for its entire rise; and has a circular cross section in the plane perpendicular to its axis.

- The density difference between the plume fluid and the ambient fluid is negligible (no buoyant plumes).
- The free stream (crossflow) velocity is constant, and the bent-over plume is carried downstream at the ambient fluid speed, U_a .
- Plume trajectory is not affected by the ambient turbulence.
- Entrainment coefficient, β , is the same constant for all plume cross-section locations.

As the plume rises, it entrains ambient fluid at its edges and increases its volume. The entrainment is modeled by an entrainment velocity, V_e . Figure 2.1 illustrates the entrainment velocity concept and other basic qualities used in the balances. The subscript, s , indicates a source quantity, subscript, p , a plume quantity and subscript, a , quantities from the atmosphere.

Conservation of mass for the plume can be determined by examining a cylindrical control volume through which the plume passes. The cross-section in Figure 2.1 also illustrates how entrainment is modeled using the entrainment velocity. Over the control volume, the increase in plume volume flux from air entrainment is

$$\frac{dQ_e}{dx} = 2\pi R_p V_e \quad (2.1)$$

This equation states the increase of the total volume flux is equal to the total inflow at the plume outer surface. The π in the RHS of Equation 2.1 is sometimes absorbed into the entrainment velocity to follow the notation of Morton, Taylor and Turner (1956).

The trajectory of the vertical jet in Figure 2.1 with upward velocity W_s and density ρ_s issuing from a round jet with a radius R_s is determined by its momentum

flux. The momentum flux is defined as the product of the source jet momentum per unit volume ($\rho_s W_s$) and its volume flow rate ($\pi R_s^2 W_s$). Dividing this product by ρ_a and dropping the π yields the conventional definition of vertical momentum flux.

$$F_m = \alpha_m \frac{\rho_s}{\rho_a} W_s^2 R_s^2 \quad (2.2)$$

where α_m is the momentum correction factor that adjusts for a non-uniform velocity profile across the jet exit hole. $\alpha_m = 1.00$ for uniform top hat profiles and $\alpha_m > 1.00$ for experimental non-uniform exit velocity profiles. In the present study, the jet fluid density ρ_s was the same as the ambient fluid density ρ_a .

Using the fully bent-over plume assumption that the plume cross section area in Figure 2.1 is perpendicular to the wind direction, the volume flux for the plume will be

$$Q_p = \pi R_p^2 U_a \quad (2.3)$$

When the plume is in the fully bent-over stage the horizontal plume velocity is U_a .

Conservation of momentum flux is found through a control volume approach, following Briggs (1975) or Weil (1988). The momentum flux at any point on the vertical plume trajectory is proportional to the vertical plume velocity W_p , and is equal to the initial vertical jet exit flux at velocity W_s from the source

$$F_m = \alpha_m W_s^2 R_s^2 = W_p U_a R_p^2 \quad (2.4)$$

This momentum flux can also be written as

$$F_m = W_p (R_p^2 U_a) \quad (2.5)$$

Using Morton, Taylor and Turner's (1956) definition the entrainment velocity, V_e

$$V_e = \beta W_p \quad (2.6)$$

where β is an entrainment coefficient, constant with x , and the vertical plume velocity is

$$W_p = \frac{dh}{dt} \quad (2.7)$$

where h is the plume height above the jet source exit on the surface.

From Figure 2.1, the volume flux dQ_e entrained into the circular control volume of length dx is

$$dQ_e = V_e 2\pi R_p dx \quad (2.8)$$

substituting Equations 2.6 & 2.7 into Equation 2.8

$$dQ_e = \beta 2\pi R_p \frac{dh}{dt} dx \quad (2.9)$$

substituting $dx/dt = U$ into Equation 2.9

$$dQ_e = 2\pi \beta R_p U_a dh \quad (2.10)$$

from Equation 2.3 the change in volume flux Q_p for the plume into the control volume

dx

$$\frac{dQ_p}{dx} = 2\pi R_p U_a \frac{dR_p}{dx} \quad (2.11)$$

now in the control volume dx the entrained volume flux from outside should be equal to the inside change in the volume flux,

$$dQ_e = dQ_p \quad (2.12)$$

substituting Equations 2.10 & 2.11 into Equation 2.12

$$2\pi \beta R_p U_a dh = 2\pi R_p U_a dR_p \quad (2.13)$$

simplifying Equation 2.13

$$\beta dh = dR_p \quad (2.14)$$

integrating both sides yields

$$R_p = \beta h \quad (2.15)$$

which if substituted in Equation 2.5, result is

$$F_m = \beta^2 U_a h^2 W_p \quad (2.16)$$

Equation 2.7 is substituted in Equation 2.16 to yield

$$F_m = \beta^2 h^2 U_a \frac{dh}{dt} \quad (2.17)$$

using travel time to travel distance relationship $\frac{dh}{dt} = U_a \frac{dh}{dx}$ and rearranging the equation

for integration

$$\int_0^x \frac{F_m}{\beta^2 U_a^2} dx = \int_0^{h_m} h^2 dh \quad (2.18)$$

performing this integration for β assumed constant with x (a key assumption), and

solving for h

$$h_m = \left(\frac{3 F_m}{\beta^2 U_a^2} x \right)^{1/3} \quad (2.19)$$

In fact, β varies from about 0.1 at the source to about 1.0 far along the trajectory, and the constant value of β used in the plume model is "trajectory-averaged" effective

entrainment constant that will vary with the velocity ratio W_s/U_a . This is the well-

known "1/3 Law" for momentum rise. A new variable, M , the "density averaged velocity ratio" can be defined as

$$M = \alpha_m^{1/2} \left(\frac{\rho_s}{\rho_a} \right)^{1/2} \left(\frac{W_s}{U_a} \right) \quad (2.20)$$

substituting Equation 2.4 and 2.20 into Equation 2.19 and then dividing both sides by the jet source diameter d_s yields the final normalized form of the plume rise equation

$$\frac{h_m}{d_s} = \left(\frac{3}{4\beta^2} M^2 \frac{x}{d_s} \right)^{1/3} \quad (2.21)$$

The assumption that the plume is emitted from a point source with $R_p = 0$ when $h = 0$ in Equation 2.15 is not strictly correct. To account for this, a correction is added to the Equation 2.15. A virtual initial radius, R_0 , must be included to accommodate the jet exit mass flux; so that the new expression for the growth of the plume is

$$R_p = \beta h + R_0 \quad (2.22)$$

R_0 is found by conserving mass from the vertical exit conditions with W_s at the source to the bent-over case with horizontal velocity U_a passing through bent-over radius R_0 is defined by a mass flux balance for the actual and virtual (bent-over) sources

$$\rho_s \pi R_s^2 W_s = \rho_a \pi R_0^2 U_a \quad (2.23)$$

$$R_0 = \left(\frac{W_s}{U_a} \right)^{1/2} R_s \quad (2.24)$$

If Equation 2.22 is substituted in Equation 2.5 instead of Equation 2.15 in the derivation of the momentum rise, Equation 2.16 would become

$$F_m = (\beta h + R_0)^2 U_a W_p \quad (2.25)$$

substituting Equation 2.7 into Equation 2.25 and expanding the terms

$$F_m = \frac{dh}{dt} \left(U_a (\beta^2 h^2 + 2\beta h R_0 + R_0^2) \right) \quad (2.26)$$

rearranging the terms, substituting for the time derivative and integrating gives

$$F_m x = U_a^2 \left(\frac{\beta^2 h_m^3}{3} + \beta h_m^2 R_0 + R_0^2 h_m \right) \quad (2.27)$$

transposing U_a and β produces

$$\frac{3}{\beta^2} \frac{F_m}{U_a^2} x = h_m^3 + 3 \frac{R_0}{\beta} h_m^2 + 3 \left(\frac{R_0}{\beta} \right)^2 \quad (2.28)$$

The RHS of Equation 2.27 can be put into the form $(h + R_0/\beta)^3$ by adding a $(R_0/\beta)^3$ to both sides

$$\frac{3}{\beta^2} \frac{F_m}{U_a^2} x + \left(\frac{R_0}{\beta} \right)^3 = \left(h_m + \left(\frac{R_0}{\beta} \right) \right)^3 \quad (2.29)$$

finally by solving for h_m

$$h_m = \left(\frac{3}{\beta^2} \frac{F_m}{U_a^2} x + \left(\frac{R_0}{\beta} \right)^3 \right)^{1/3} - \left(\frac{R_0}{\beta} \right) \quad (2.30)$$

Where R_0 is defined by Equation 2.24. In the present experiments the R_0 terms were considered to be self-canceling and $R_0=0$ was used.

2.3 Trajectory-averaged entrainment coefficients

The choice of the trajectory-averaged entrainment coefficient for a plume has a large effect on the predicted trajectory. Some investigators, such as Hoult and Weil (1972) and Weil(1988) suggest that the entrainment coefficient should be a constant, $\beta = 0.6$, while Briggs (1975) suggested that β should have some dependence on the velocity ratio W_s/U_a . Fay, Escudier and Hoult (1970) found a dependence on velocity ratio up to $M = 1.2$, after which they suggest β would be constant. Johnston and

Wilson (1997) found a continuous dependence of β on the velocity ratio, with a weakening influence of M as M increases beyond about $M=4$.

In this study, the entrainment coefficient was allowed to vary as a function of velocity ratio, M , and jet exit Reynolds number, Re_d . The reason for varying β with velocity ratio is that as M increases, more of the rise of the plume is near vertical and β will be smaller, so introducing a dependence on M is a simple way of varying entrainment coefficient. The reason for allowing β to vary with nozzle exit Reynolds number is that as the Reynolds number increases the jet becomes more turbulent and might entrain more ambient fluid, increasing the trajectory-averaged entrainment coefficient β .

2.4 Added mass acceleration effects on entrainment coefficients

When the entrainment coefficient β is set to match trajectory mass balances, β always over-predicts the actual concentration. The concept of *added mass* is used in several plume models to compensate for that problem. The added mass approach multiplies the effective mass in a plume cross-section of length dx by a factor of $(1+f)$, to account for the force required to displace ambient fluid as the plume accelerates vertically. This added mass approach was used by Escudier and Maxworthy (1973), Briggs (1975), Weil (1988) and Davidson (1989) in their derivation of the plume rise equations. For a fully bent-over plume, an analogy for the application of added mass is a log rising in water. As a log rises, it will accelerate due to buoyancy. Fluid will be pushed out of the way and added mass term would be necessary. In Davidson (1989) the

plume rise equations were derived including the added mass where the result was expressed as a variation of the entrainment coefficient so,

$$\beta = (1 + f)^{1/2} \beta_{dilution} \quad (2.31)$$

Briggs (1975) suggested a value of $f = 1.3$, which means β would be 1.5 times larger than the entrainment coefficient needed for dilution. Using the added mass concept allows a single entrainment coefficient to be used for both trajectory and dilution predictions. In the present study, no dilution calculations were performed, so values of f were not determined.

2.5 Downwash velocity correction

A new concept was developed in the present study to account for the influence of the low pressure zone on the surface jet trajectory "Wilson 2001, private communication". That low pressure zone was developed on the wall downwind of the jet exit, see Figure 2.2. A physically realistic spatially-varying downwash velocity W_d model is introduced in the plume rise equation. The explanation for downwash is that the low pressure area behind the plume affects the plume's ability to rise. The emerging vertical jet produces a low pressure wake which acts like an obstacle in the path of the ambient fluid.

This distributed pressure downwash model for the surface jet was inspired by the work of Johnston and Wilson (1997) in wakes behind circular stack jets. They used the same type of downwash model for the stack, although the physics of stack-induced downwash is quite different. For stacks, downwash is caused by the interaction of the plume and a counter rotating vortex pair shed from the stack and bent-over parallel to the

plume trajectory because vortex remains attached to stack tip, see Figure 2.4. For surface jets interacting with a large flat wall, the downwash effect appears to be caused by a low pressure region on the surface immediately behind the exit hole. This is also known as the Coanda effect. Figure 2.2 illustrates this downwash concept and other basic quantities. As Figure 2.2 shows, the plume is induced into the low pressure zone by an effective downwash velocity W_d . This downwash velocity decreases with x as the low pressure P_{low} decreases into the wake.

Section A and section B in Figure 2.2 are shown in Figure 2.3. Section A is where the plume is near to the wall and the entrainment into the plume causes the low pressure zone to form behind the jet exit hole. Section B is where the plume is far away from the wall and the low pressure zone induced by vortex roll up is much weaker.

An equation for the downwash velocity can be derived from the assumption that near surface downwash is caused by a low pressure region on the wall behind the plume. The plume downwash velocity W_d can be written in terms of pressure differences as

$$W_d = \frac{dh}{dt} \Big|_{downwash} \propto \left(\frac{2(P_\infty - P_x)}{\rho} \right)^{1/2} \quad (2.32)$$

where P_x is the wake pressure behind the jet at downstream distance x and P_∞ is the pressure in undisturbed flow.

The pressure loss can be related to the source radius R_s and downstream distance x as a dynamic pressure coefficient that is assumed to decay as x^{-2n} ,

$$(P_\infty - P_x) = C_{\Delta P} \left(\frac{\rho U_a^2}{2} \right) \left(\frac{R_s}{x} \right)^{2n} \quad (2.33)$$

where $C_{\Delta P}$ is a dynamic pressure coefficient. Substituting Equation 2.33 into Equation 2.32, the $\rho/2$ cancels and

$$W_d = B_1 U_a \left(\frac{R_s}{x} \right)^n \quad (2.34)$$

where B_1 is a constant of proportionality. For unimpeded plume rise, the plume upward momentum rise velocity, W_p , with no downwash is

$$W_p = \left. \frac{dh}{dt} \right|_{\text{no downwash}} \quad (2.35)$$

from Figure 2.3

$$W_{\text{net}} = W_p - W_d \quad (2.36)$$

$$\frac{dh}{dt} = \left. \frac{dh}{dt} \right|_{\text{no downwash}} - \left. \frac{dh}{dt} \right|_{\text{downwash}} \quad (2.37)$$

$$\frac{dh}{dt} = \left. \frac{dh}{dt} \right|_{\text{no downwash}} - B_1 U_a \left(\frac{R_s}{x} \right)^n \quad (2.38)$$

multiply Equation 2.38 by $\frac{1}{U_a}$

$$\frac{1}{U_a} \frac{dh}{dt} = \frac{1}{U_a} \left. \frac{dh}{dt} \right|_{\text{no downwash}} - \frac{B_1 U_a}{U_a} \left(\frac{R_s}{x} \right)^n \quad (2.39)$$

$$U_a dt = dx \quad (2.40)$$

$$\frac{dh}{dx} = \left. \frac{dh}{dx} \right|_{\text{no downwash}} - B_1 \left(\frac{R_s}{x} \right)^n \quad (2.41)$$

integrating on both sides

$$h = \int_0^x \left. \frac{dh}{dx} \right|_{\text{no downwash}} dx - \int_0^x \frac{B_1 R_s^n}{x^n} dx \quad (2.42)$$

$$h = h_{no\ downwash} - \frac{B_1 R_s^n x^{1-n}}{1-n} \quad (2.43)$$

$$B_2 = \frac{B_1}{1-n} \quad (2.44)$$

dividing both sides of the Equation 2.43 by d_s

$$\frac{h}{d_s} = \frac{h|_{no\ downwash}}{d_s} - (B_2 x^{1-n}) \frac{R_s^n}{d_s} \quad (2.45)$$

substituting $R_s = \frac{d_s}{2}$

$$\frac{h}{d_s} = \frac{h|_{no\ downwash}}{d_s} - (B_2 x^{1-n}) \frac{d_s^n}{2^n d_s} \quad (2.46)$$

$$B_3 = \frac{B_2}{2^n} \quad (2.47)$$

where B_3 is the downwash coefficient

$$\frac{h}{d_s} = \frac{h|_{no\ downwash}}{d_s} - B_3 \left(\frac{x}{d_s} \right)^{1-n} \quad (2.48)$$

from Equation 2.21, for a point source momentum jet with $R_0 = 0$, the 1/3 law for plume rise is

$$\frac{h|_{no\ downwash}}{d_s} = \left(\frac{3}{4\beta^2} M^2 \frac{x}{d_s} \right)^{1/3} \quad (2.49)$$

substituting Equation 2.49 into Equation 2.48

$$\frac{h}{d_s} = \left(\frac{3}{4\beta^2} M^2 \frac{x}{d_s} \right)^{1/3} - B_3 \left(\frac{x}{d_s} \right)^{1-n} \quad (2.50)$$

Equation 2.50 is the non-dimensional plume rise equation for a fully bent-over non-buoyant momentum jet, accounting for jet wake pressure-induced downwash.

The value of the exponent $(1 - n)$ varies, depending on whether the wake is two dimensional or three dimensional and the behavior of the nearwake recirculation region downstream of the jet hole.

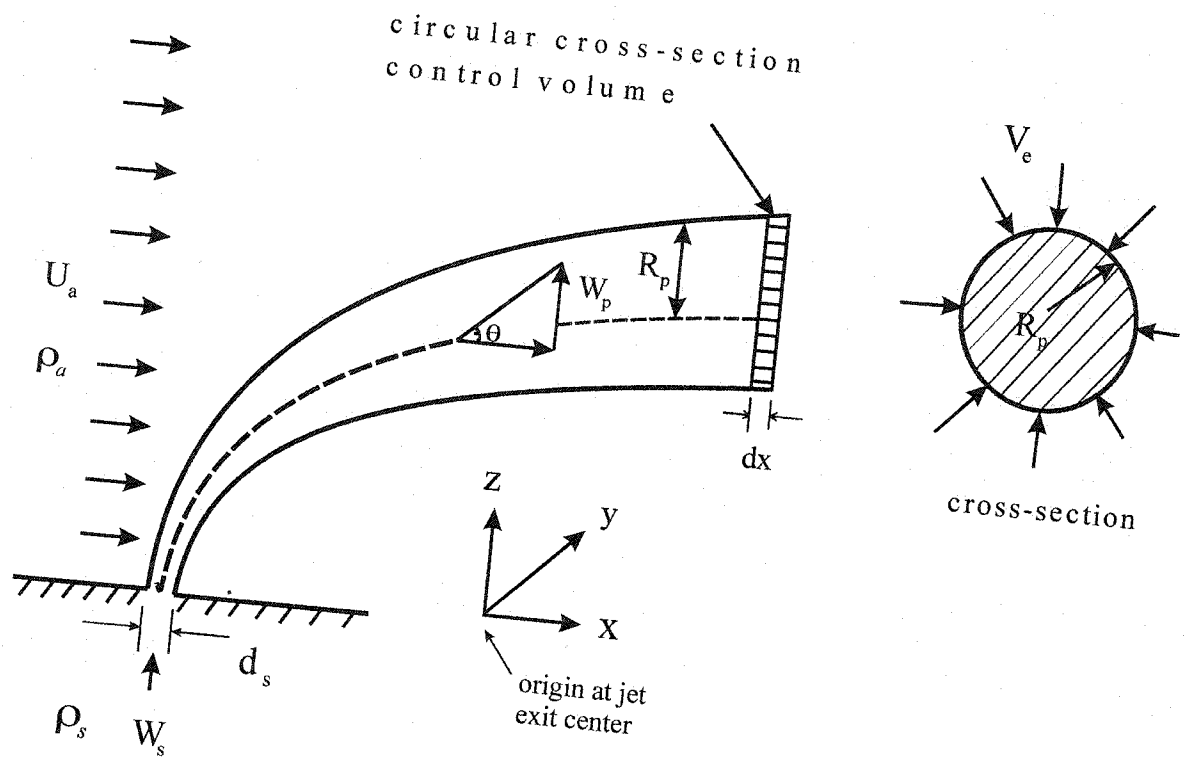


Figure 2.1 Schematic of the plume showing the characteristic parameters used in the plume rise equation.

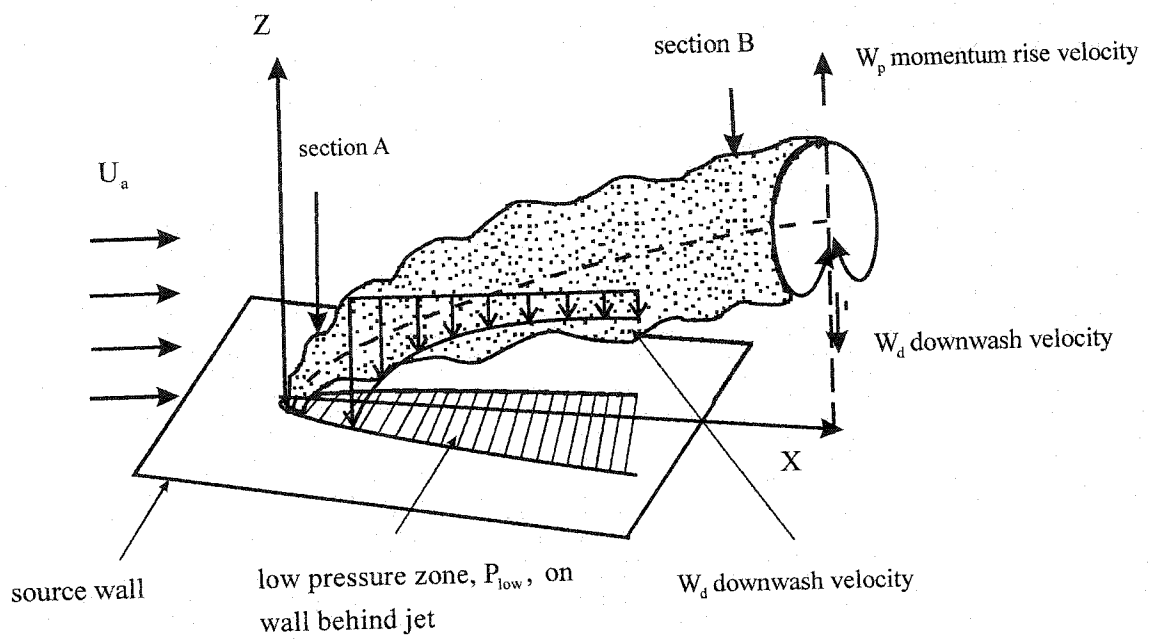
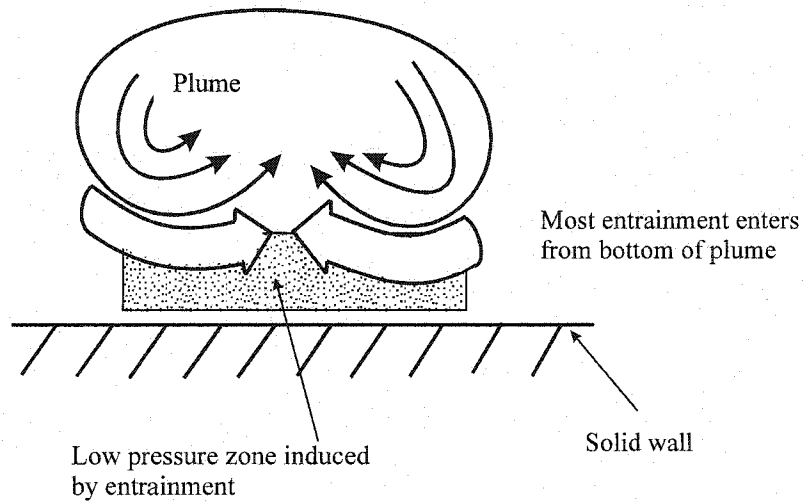


Figure 2.2 Continuous downwash velocity distribution along the plume. Downwash velocity W_d decreasing with x as rising plume increases space for entrainment into bottom of bent-over plume.

Cross section A Bent-over Jet near wall



Cross Section B Bent-over Jet far from wall

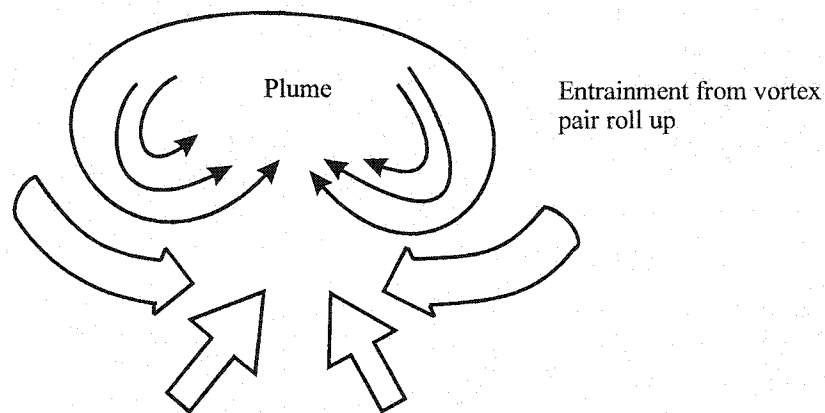


Figure 2.3 At Section A (above), the jet is closer to the wall and a low pressure zone produces downwash as vortex roll up induces entrainment. At Section B (below), plume is far away from the wall and low pressure zone induced by vortex roll up is much weaker.

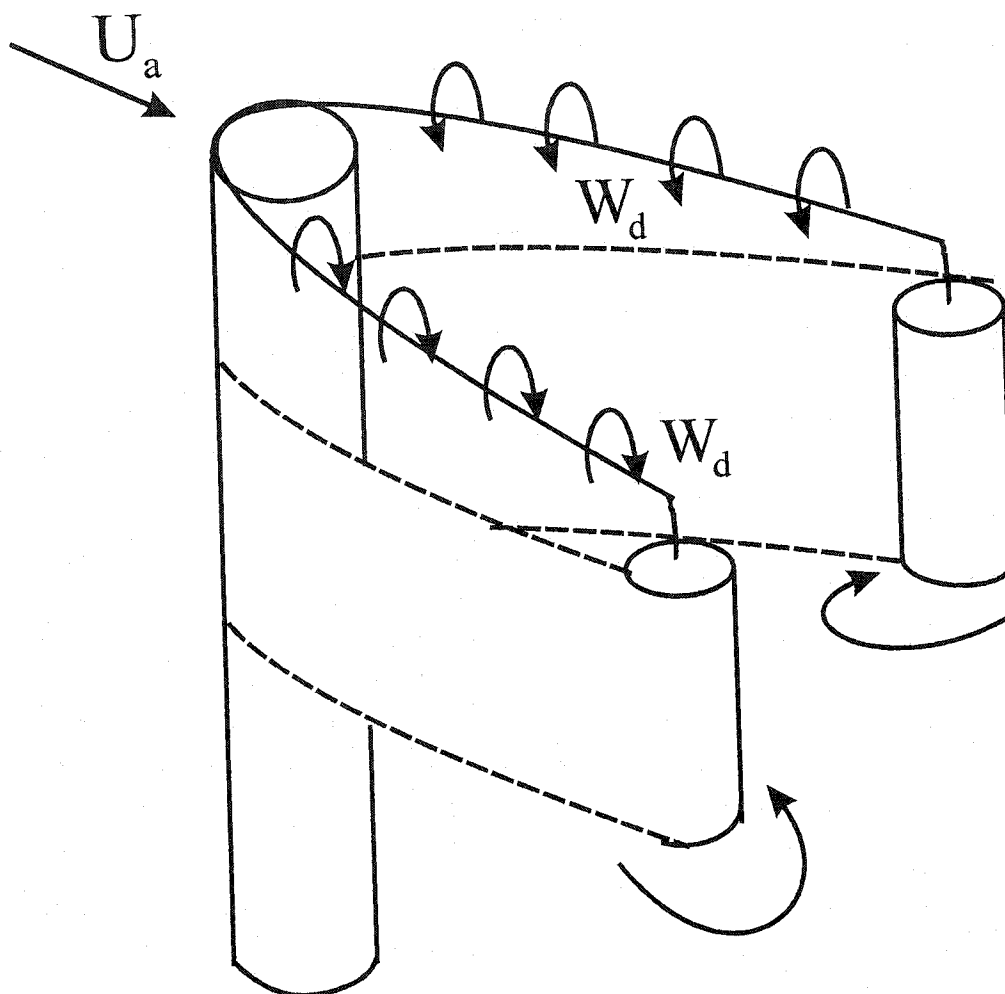


Figure 2.4 Connection of shed vortices back to a stack tip to produce stack wake downwash velocity W_d .

Chapter 3

Water Channel Experiment Technique

3.1 Introduction

The experimental method and equipment used to simulate and measure the plume trajectory and velocity profiles will be discussed in this chapter.

- Mean velocity and turbulence intensity measurements using *Laser Doppler Velocimeter* (LDV).
- Plume trajectory measurements using a laser sheet lighting dye trace fluorescence flow visualization technique.

Each of these techniques provided valuable data such as mean velocity, turbulence intensity and plume centerline concentration.

3.2 Water channel

All the experiments in this study were conducted in the Mechanical Engineering water channel. The water channel test section is 5000mm long x 680mm wide x 476mm deep. A schematic of the water channel is shown in Figure 3.1 & 3.2. These Figures are described in details later. Two stainless steel tanks are attached to the ends of the test section. Using two 3.7 kW pumps, water was circulated from tank to tank through a 152mm I.D. return pipe lying under the test section. The flow rate through the water channel was monitored using a manometer across an orifice plate, placed in the return pipe. The flow rate in the water channel was controlled by valves on the pump outlet, and by operating one or both pumps at a time.

Air bubbles were removed from the orifice plate and manometer tubes to obtain accurate readings. When there was no flow in the water channel, the water level was set at equal heights in both manometer columns. For details of the water channel see Johnston (1994).

It was possible to operate the water channel through a range of mean velocities of 3 to 18 cm/s. Exit jet velocities were calculated for large ($d_s = 12.7 \text{ mm}$) and small sources ($d_s = 3.175 \text{ mm}$) for the velocity ratios of 1,2,4,8 and 16 within the water channel velocity range. As Figure 3.3 shows, it was possible to maintain the same Reynolds number for some of the exit velocity to crossflow velocity conditions with both large and small sources.

3.2.1 Measuring jet exit velocity profiles

Jet exit velocity profiles were measured with stagnant ambient fluid in the water channel. For experimental convenience, the source was placed at the bottom of the water channel and the jet was vertical as shown in Figure 3.2. The coordinate system for the horizontal jets in crossflow (Figure 3.1) was rotated so z was along the jet axis in both cases. The source jet position was measured from the sidewall of the water channel. To determine the location of the edges of the source nozzle, the four laser beams of the LDV were aimed as a point on the sidewall of the water channel and the traverse scale was set to zero. Then the source distance from the water channel and its center were measured by inserting a rod into the jet exit hole. This rod had exactly the same diameter as of the source hole with a shoulder machined at the end to hold it vertical. Then the LDV laser beams were moved horizontally to intersect on the aimed rod. This distance was verified

using a scale. To set the laser beams as close as possible to the source exit, the 4 beam (2 component, 2 color) LDV probe was rotated at 45° angle. The closest possible distance to the outlet was 3 mm, i.e., roughly 1/4 diameter above the large source ($d_s = 12.7$ mm) and 1 diameter size of the small source ($d_s = 3.175$ mm).

The sample duration was selected by taking the time averages of the LDV readings over 10, 30 and 100 seconds. Figure 3.4 shows the ratios between local mean velocities measured over 10, 30 and 100 seconds with typical sampling rate of approximately 1000 points per second. The variation is only $\pm 3\%$, so a moderate duration average time period of 30 seconds was selected for velocity readings.

3.3 Velocity and turbulence intensity measurement

The mean velocity and turbulence intensity measurements were made using a LDV. Two types of TSI Laser LDV systems, 1 component and 2 component, were used to collect the velocity data. Although both these equipments had different set up procedures and two different soft ware packages were used to analyze the data, the results are very close to each other. Figure 3.5 shows that these two-velocity profiles are similar. Mean velocity, W , of the jet in the z direction was normalized by its centerline velocity W_0 ; and the radial distance x was normalized by the source diameter d_s . The difference is only $\pm 3\%$ except at the edges where the difference is very large (about 80 %). At the edges the velocity profiles taken with 2 component LDV were better than the 1 component, therefore for the rest of the experiments velocity profiles were taken by the 2 component LDV.

3.4 Titanium dioxide seeding

The particle seeding used for the LDV in the water channel and in the jet supply was titanium dioxide. About 2 grams of TiO_2 powder were added in the water channel and then the water channel was allowed to run for 3 to 4 minutes to mix the seeding. Care was taken to avoid over-seeding in the water channel. Over seeding was easy to spot as the water would become cloudy (like very diluted milk) and when the water was over-seeded the laser beams from the LDV would be absorbed before reaching across the channel.

3.5 Experimental set up

Figures 3.1 & 3.2 show the experimental configuration for LDV and LIF (Laser induced fluorescence) flow visualization measurements. Disodium fluorescein for flow visualization, or titanium dioxide for LDV seeding, was stored in a pressurized tank with a volume of approximately 75 liters. To get the same seeding properties as water in the water channel, the tank was filled directly from the water channel. Air above the mixture was pressurized by connecting a valve on the top of the tank to a pressure line maintained at 30 psi. The pressurized air forced the mixture out of the tank through an opening at the base to a hose leading to the rotameter control panel. The flow passed through valves of the control panel to one of the four rotameters and then to the source through a flexible rubber hose.

3.5.1 Rotameter calibration

To calibrate each of the four rotameters, flow from the rotameters was ejected into a beaker and the time taken to fill the beaker with a particular volume of water was

measured. Readings were taken at a number of settings over the range of each rotameter. Figure 3.6 to 3.9 show plots of calibration for each of the four rotameters. A straight line adequately fitted the calibration points for all four rotameters. Listed below are the calibration functions for each rotameter tube. S_{rot} is the scale setting (at the center of the ball or on the top of the float) on the rotameter tube reading and Q_{rot} is the rotameter flow rate in mL/second.

$$\text{Rotameter R-8M-25-4F-D} \quad Q_{rot} = 1.560 S_{rot} + 0.711 \quad (3.1)$$

$$\text{Rotameter R-8M-25-4F-I} \quad Q_{rot} = 0.904 S_{rot} + 1.670 \quad (3.2)$$

$$\text{Rotameter R-6-15-B} \quad Q_{rot} = 1.522 S_{rot} - 1.212 \quad (3.3)$$

$$\text{Rotameter R -603} \quad Q_{rot} = 0.016 S_{rot} + 0.24 \quad (3.4)$$

Equations 3.1 to 3.4 were used to find the appropriate rotameter setting for a specified jet exit flow rate.

3.6 Jet trajectory measurement

Measurements of the jet trajectory were made by injecting a non-buoyant momentum jet from the turbulent source into a cross flow at the same water temperature. As shown in Figure 3.1, a splitter plate (a false floor flush with the source exit plume) was placed over the source to avoid the wake and other disturbances caused by the source in the cross flow. All the measurements were taken over the flat splitter plate that formatted the surface. The source was mounted flush with the flat plate. Velocity profiles were measured to determine the boundary layer effects on the source splitter

plate in the water channel at different positions with or without placing the source in the path of the flow.

The source shown in the Figure 3.1 extended horizontally outwards 90 mm from one of the sidewalls. The source was placed at 220 mm above the bottom of the water channel, slightly above the mid point of the 400 mm water depth. At that height, the mean velocity profile of the crossflow was measured across the channel to observe the boundary layer effect over the flat splitter plate. Water channel mean velocity profiles were measured again, at 50 mm to each side of the source hole centerline. Figure 3.10 shows that all these water channel crossflow velocity profiles are within 2.5% of one another. Figure 3.11 shows the distance up to $z = 200$ above the splitter plate and as shown in figure the water channel velocity profile in this portion is almost flat.

In order to get the laser beams to interact across most of the 680 mm width of the water channel, a lens with a focal length of 514.5 mm was used to cross the LDV beams. The average crossflow velocity measured from the water channel LDV data was only 10% lower than the average bulk velocity calculated from the orifice volume flow rate read from the manometer reading across the orifice in the return pipe.

3.7 Velocity profile measurements in the jet with no crossflow

Figure 3.2 shows the experimental set up to measure jet exit velocity profiles. For experimental convenience the source was placed at the bottom of the water channel but the same coordinate system was used as was in the case of jet trajectory measurements, shown in the Figure 3.2. Velocity profiles were measured with the 2 component LDV with no cross flow in the water channel, with and without a splitter plate above the source. The objective was to measure the velocity profiles in the very near region of the

source in order to lessen the ambient fluid entrainment effects on the velocity profiles. The laser beams were rotated 45° to measure the velocity profiles as close as possible to the jet exit, at a distance of 3mm above the source. In terms of source diameter 3 mm is $0.25 d_s$ for the large source and $1.0 d_s$ for the small source. Because the small source velocity profiles were measured at the 1.0 diameter distance (3mm) above the source, for the comparison purposes with the large source, velocity profiles were also measured at the 1 diameter distance (12mm) above the large source.

3.8 Jet image acquisition system

3.8.1 Camera

Images were collected by a Hitachi KP-M1 CCD (charge-couple device) monochrome (black and white) video camera using a filter. The filter is described in section 3.9.2. The lens was a 12.5 to 75 mm zoom lens with aperture F1.8 to F22. For the large source, $d_s = 12.7$ mm, the camera was set to a focal length of 20 mm and an aperture of F1.8. For the small source, $d_s = 3.175$ mm, the camera was set to a focal length of 12 mm and an aperture of F1.8. Images were collected at a shutter speed of $1/30$ s. Fabris (1998) showed that for this camera, the measured brightness output was linear with the dye concentration.

The camera was placed normal to the cross flow. The field view of the camera is shown in Figure 3.1. Pixel size was measured by focusing the camera in the $x-z$ plane of the source and acquiring an image of known scale. The centerline trajectory of the source jet was determined from the average intensity of 1800 images recorded at rate of 6 images per second for 300 seconds using the video camera.

3.8.2 Analog to digital conversion of video signals

The analog signal from the camera was digitized by a computer video board (Matrox Pulsar version 1.0) to produce images with a light intensity resolution of 10 bits (1024 intensity levels) and spatial resolution of 640 pixels horizontally and 480 pixels vertically. To acquire the images, a Visual Basic program developed by Majeski (2000) was used. Image processing was employed using Matlab 6.0 with the image processing toolbox.

3.9 Measurement of jet trajectory using laser induced fluorescence

The objective of the present study was to determine the velocity ratio and Reynolds number effects on the jet trajectory and entrainment rate. Fluorescent tracer dye illuminated by laser sheets was used to track the dispersion of the jet exiting in the cross flow. To record video images, the camera was placed roughly 80 to 100 cm (depending on the source size) above the water surface looking down on the source, see Figure 3.1. Six frames per second of 640 x 480 pixels were grabbed from the camera by the Matrox Pulsar Board that digitized each pixel output with 10 bit resolution, with brightness values from 0 to 1023.

3.9.1 Laser induced fluorescence

Disodium fluorescein was used as the dye tracer in the water channel experiments. The fluorescent dye was injected out of the source hole to simulate the jet. A 30⁰ Powell lens was used to obtain a practically uniform laser light sheet from a 4 watt argon-ion laser. When dye molecules pass through the laser light sheet, they fluoresce and the resulting fluorescent light intensity was measured by pixels of the video camera.

The laser light sheet had a minimum thickness of approximately 2 mm. The overall power transmission efficiency from laser output to light sheet of this system was approximately 60%-65%.

3.9.2 Dye tracer

Disodium fluorescein dye was used as a tracer to track the jet dispersion. The fluorescent dye was stored in a 75L tank connected to a pressure line. Flexible tubing carried the dye mixture from the tank through one of four rotameters to control the flow rate. The dye was then carried from the rotameter through flexible tube to the source. The fluorescent dye absorbs laser light at green-blue wavelengths around 488 nm and its peak fluorescence emission is in the green-yellow around 515nm. This difference in emission and absorption wavelengths allowed a yellow gel filter (Kodak 15) over the camera lens to pass light near the emission wavelength and block light near the absorption or laser wavelength, thus allowing the camera to see mostly fluorescent light from the dye tracer, and negligible reflected light from the laser. In this way noise was reduced by filtering out the direct laser light reflected from micro bubbles of air in the water.

Fluorescein dye has the advantage of being relatively insensitive to the temperature. Walker (1987) shows the variation of fluorescent intensity to be 0.3% per K. The dye has been shown, however, to be sensitive to pH changes produced by water when the value of pH is below about 7.5. However, in this study, only jet trajectories were measured so pH was not an important factor.

3.9.3 Calibration images

A closed calibration box was made by placing two tight fit plastic sheets on the upstream and downstream sides of the source in the water channel. Gaskets were placed between the water channel side walls and plastic sheets. The inside dimensions of the calibration box were 900 mm long by 680 mm wide with length in the direction of the flow. The height of the water in the closed volume was 340 mm. This yielded a calibration volume of 208 liters.

After the laser had been turned on and properly aligned with the source center, a background image of 200 frames at 6 frame per second was taken using the frame grabber software with no fluorescent dye in the water. Once the background had been recorded, calibration images were taken with three different concentrations of fluorescent dye in the enclosed volume around the source. The three concentrations used for all calibrations in the present study were 0.4 mg/L, 0.04 mg/L and 0.009 mg/L for large source ($d_s = 12.7 \text{ mm}$) and for small source ($d_s = 3.175 \text{ mm}$) were 1.6 mg/L, 0.16 mg/L and 0.016 mg/L. From the volume of the box, the amount of fluorescent dye required to produce the above concentrations could be calculated. The appropriate amount of powdered fluorescein dye was measured by weight on an electronic balance.

The calibration images were taken at 6 frames per second using the frame grabber software. The calibration and the experiment were done in sequence so that camera and laser sheet remained aligned, allowing background images to be subtracted from jet images. The pixel size was calculated by putting a known scale in the view and thus taking the pictures of this scale in x and z directions.

3.9.4 Laser light attenuation through a plume

As a beam of laser light travels through a concentration of fluorescein dye, the intensity of the beam gradually decreases as photons are absorbed by the dye particles and water. The attenuation of the beam at a certain point depends upon the concentration profile over the entire beam length up to that point. For a plume with a highly intermittent concentration profile, correcting for laser beam attenuation would be very difficult, as it would require knowledge of the concentration profile at each point in time. The experiments were arranged so that the plume concentration would never be large enough to cause significant attenuation.

Negligible light attenuation through the plume was achieved by choosing an appropriate value for the source jet concentration. To estimate the attenuation through a plume, consider a source of diameter d_s emitting at a uniform concentration C_s . The diameter of the plume grows roughly in proportion to downstream distance x from the source

$$d_{plume} = d_s + Ax \quad (3.5)$$

Mass conservation then requires that the concentration C_x at a downwind position obey the relation:

$$C_x \frac{\pi d_{plume}^2}{4} = C_s \frac{\pi d_s^2}{4} \quad (3.6)$$

For a coherent beam of laser light, the decay of beam intensity I_e goes like

$$I_e = I_0 \exp\left(-\epsilon_a \int_0^y C(y) dy\right) \quad (3.7)$$

Where I_0 is the initial intensity of the beam at $y=0$ and ε_a is the attenuation coefficient.

The value of the attenuation coefficient for fluorescein in water is $\varepsilon_a = 0.023$

$[\text{mg/L}]^{-1} [\text{mm}]^{-1}$ calculated from linescan video data by Hilderman (private communication, 2001) in his experiments in the same water channel. The attenuation will be negligible if the integral of concentration with distance is less than some critical value

$$\int_0^y C(y) dy < \text{crit} \quad (3.8)$$

The critical value will depend on what maximum acceptable concentration across the plume is required. For a uniform concentration C_s at the source, the integral of the concentration across the source diameter is

$$\int_0^{d_s} C_s dy = C_s d_s \quad (3.9)$$

Then at any downstream position x

$$\int_0^{d_{plume}} C_x dy = C_x d_{plume} \quad (3.10)$$

from Equation 3.6

$$C_x d_{plume} = C_s \left(\frac{d_s^2}{d_{plume}} \right) \quad (3.11)$$

since d_{plume} is always larger than d_s , from Equation 3.8 then

$$C_x d_{plume} = C_s d_s \left(\frac{d_s}{d_{plume}} \right) < C_s d_s \quad (3.12)$$

Then for a given source size d_s , fixing the value of C_s guaranteed that there was negligible attenuation at the source. This ensures that there is negligible attenuation at all downstream locations.

For the source, $d_s = 12.7$ mm, the inlet concentration was fixed at 0.4 mg/L.

Similarly for the small source, $d_s = 3.175$ mm, the inlet concentration was fixed at

1.6 mg/L. This gives an attenuation factor of

$$\frac{I_e}{I_0} = \exp[-\varepsilon_a C(y) d_s] = 0.89 \quad (3.13)$$

or 11% attenuation across the source, which was determined to be acceptable. At all downstream locations, the attenuation will be less than 11%.

3.9.5 Accounting for light attenuation in concentration measurements

A gain G_{ij} was calculated for each pixel so that the concentration at any point C_{ij} is related to the observed intensity as

$$C_{ij,cal} = G_{ij} \left(\frac{(I_{ij,C_{cal}} - I_{ij,C_0})_{camera}}{\exp(-\varepsilon_a C_{cal} (y_1 + y_{ij}))} \right) \quad (3.14)$$

$(I_{ij,C_{cal}})_{camera}$ = Camera intensity at each pixel at a known concentration.

$(I_{ij,C_0})_{camera}$ = Camera intensity at each pixel with zero concentration.

y_1 = Distance between the Powell lens and the outer (air) side of the water channel side wall.

y_{ij} =Distance traveled by laser sheet from the inner (water) side of the water channel sidewall to each pixel.

The laser light was attenuated due to two reasons

- Attenuation due to spread of laser sheet both in x and z directions.
- Attenuation due to the concentration as the light traveled towards the jet source.

As the laser light spreading was same in both the calibration and in the experiment images, this effect is accounted for during calibration. For this reason, only attenuation due to concentration in the jet was considered in post processing.

Concentration C_{ij} was calculated from the following equation

$$C_{ij} = G_{ij} (I_{ij} - I_{back,ij})_{camera} \quad (3.15)$$

where $(I_{ij})_{camera}$ is the camera intensity at each pixel for a certain case and $(I_{back,ij})_{camera}$ is the camera intensity taken by the image when there is no jet released.

From Equation 3.14 G_{ij} was calculated and substituted in the Equation 3.15

$$C_{ij} = \frac{C_{ij,cal} \left[(I_{ij} - I_{back,ij})_{camera} \left(\exp(-\epsilon_a C_{cal} (y_1 + y_{ij})) \right) \right]}{(I_{C_{cal},ij} - I_{C_0,ij})_{camera}} \quad (3.16)$$

from Equation 3.16 the concentration was calculated at each pixel.

3.9.6 Selecting averaging time and trajectory for jet images

To select an appropriate averaging time, for jet images, video images were collected for 33, 200, 300 and 400 seconds. The number of images related to each test were 200, 1200, 1800 and 2400 images at the constant frame grabbing rate of 6 images per second. Four different average images were produced. As shown in Figure 3.12a the

contour profiles of the average image produced from 200 images were not very clear. Instead of contours there were small patches which did not tell any trend. The contour profiles of the average image produced from 1200 images were better but still there were small bumps in the contour profiles. Figure 3.12c is the contour profiles of the average image produced from 1800 images and the contour profiles in this case are relatively uniform. The contour profile images produced from 1800 and 2400 images were very close to each other so an averaging time 300 seconds to produce 1800 images per test run was an appropriate choice to reduce dye injection time. All these images are an average of 1/30 sec video frames, taken 1/6 s apart (6 frames/s), in a crossflow with velocity $U_a = 180 \text{ mm/s}$, which is 14 source diameter/s.

There is one interesting observation shown in Figure 3.12 c, marked as A, B and C. There is high concentration on points A and C and on point B the concentration is low. This can also be seen in Figure 3.12 b and d. The cause of this is probably the side to side meandering of vortex pair plume with two off-axis concentration maxima. Point B is just the region where the meandering is reduced and the low concentration between the vortex pair becomes dominant. Video images were used only to determine the plume centerline trajectory therefore these changes in iso intensity contours did not make any difference in the final results, see Figure 3.14.

Figure 3.13 shows the medians calculated from the intensity and concentration images; note how the values from both cases are the same. It is important to note that these median values are the concentration profile area median of the z value and not the median of the concentration itself. Median values will ignore the values in the tails of the distribution. Median can be defined as

$$\int_0^{z_{median}} c(z) dz = 0.5 \int_0^{\infty} c(z) dz \quad (3.17)$$

The trajectory calculated from the average intensity image therefore matched completely with the average concentration image calculated by converting the light intensity image to a concentration image. This result corroborates the result of Fabris (1998), cited previously. The profiles shown in Figures 3.12 & 3.13 are combined in Figure 3.14. Intensity (or concentration) profiles were plotted on the average intensity (or concentration) image and the median of each concentration profile was subsequently determined. These medians are determined in the plume image as shown in Figure 3.14. The jet trajectory was drawn by joining the median of each intensity or concentration profile.

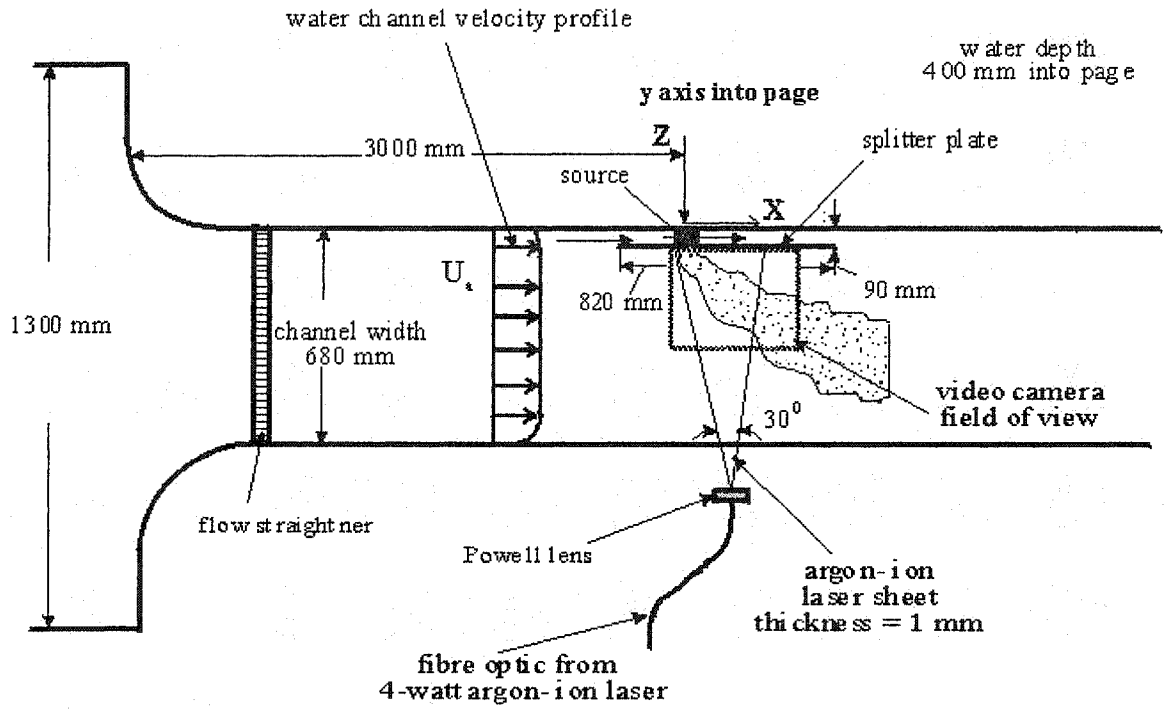


Figure 3.1 Schematic view of the water channel facility, looking down through the free water surface.

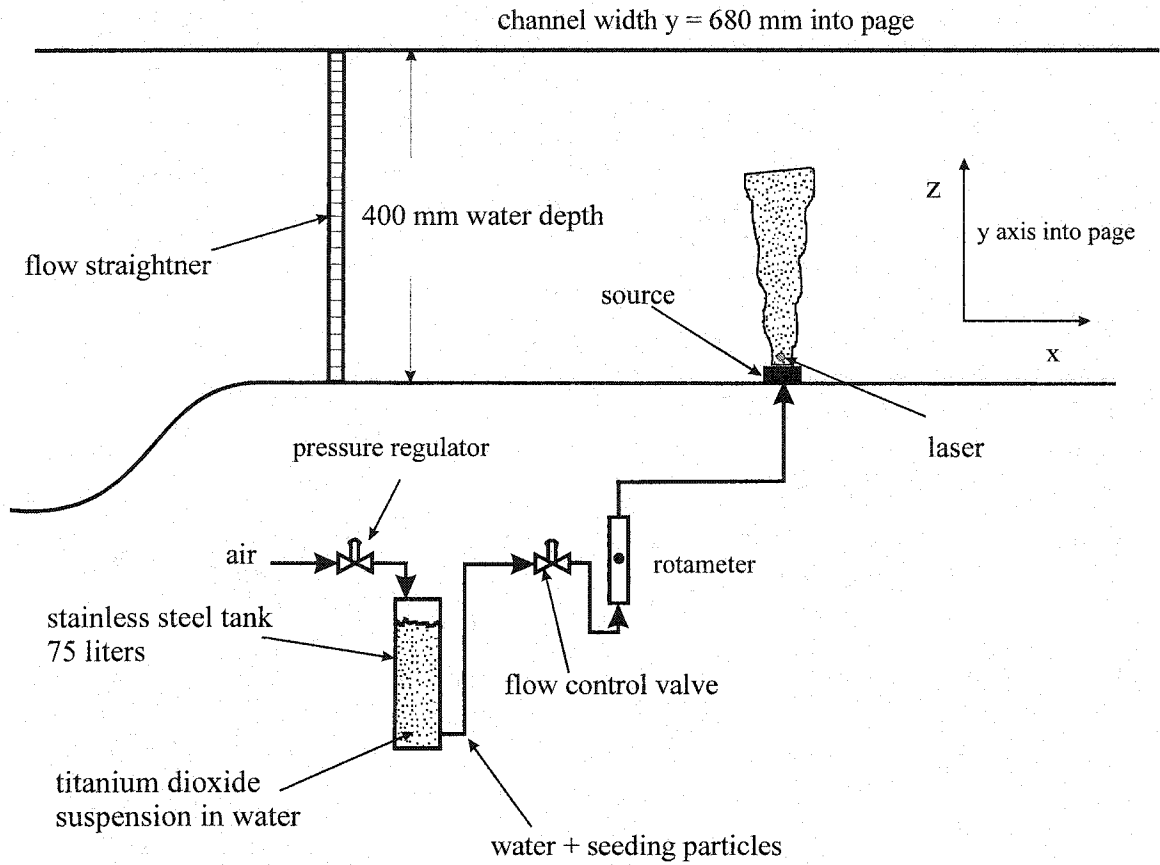


Figure 3.2 Schematic side view of the water channel with the jet set-up on the bottom of the channel for LDV measurements.

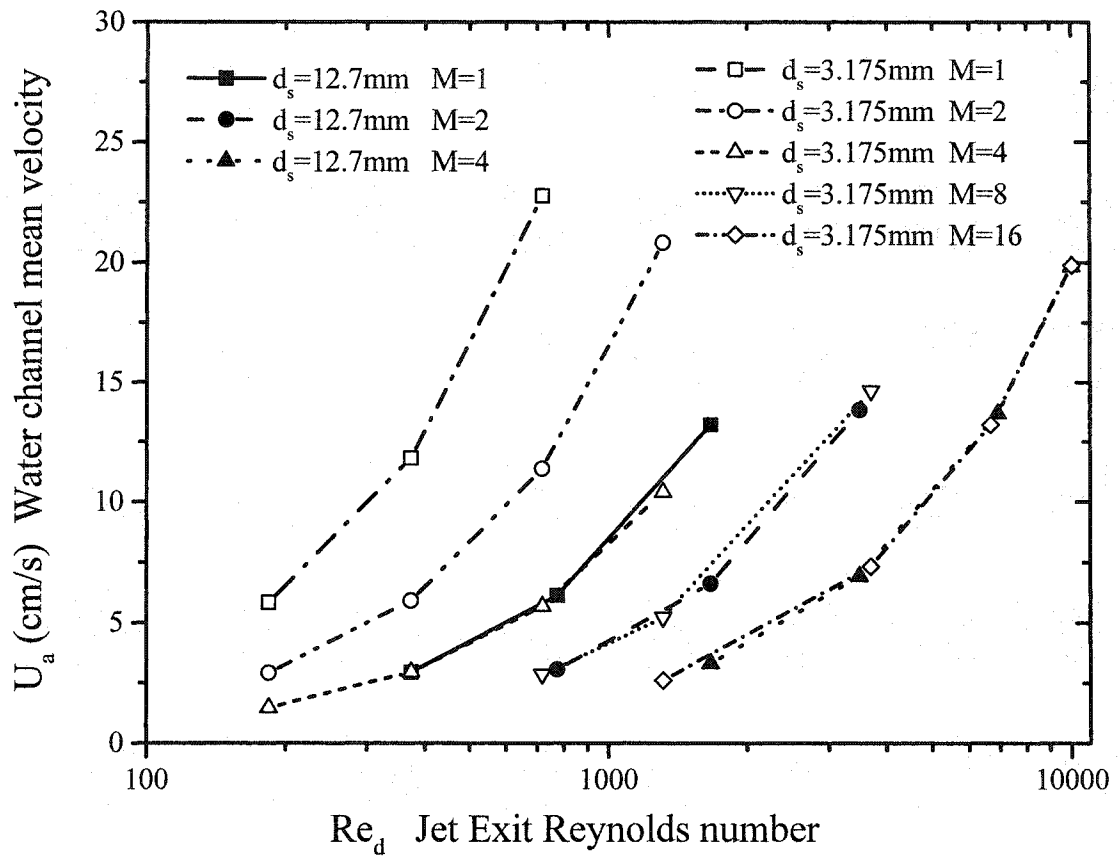


Figure 3.3 Range of available jet Reynolds numbers corresponding to various source velocity to cross wind velocity ratios $M = W_s / U_a$ to crosswind velocity U_a ratios, M . Limits of curves are set by source jet operating range.

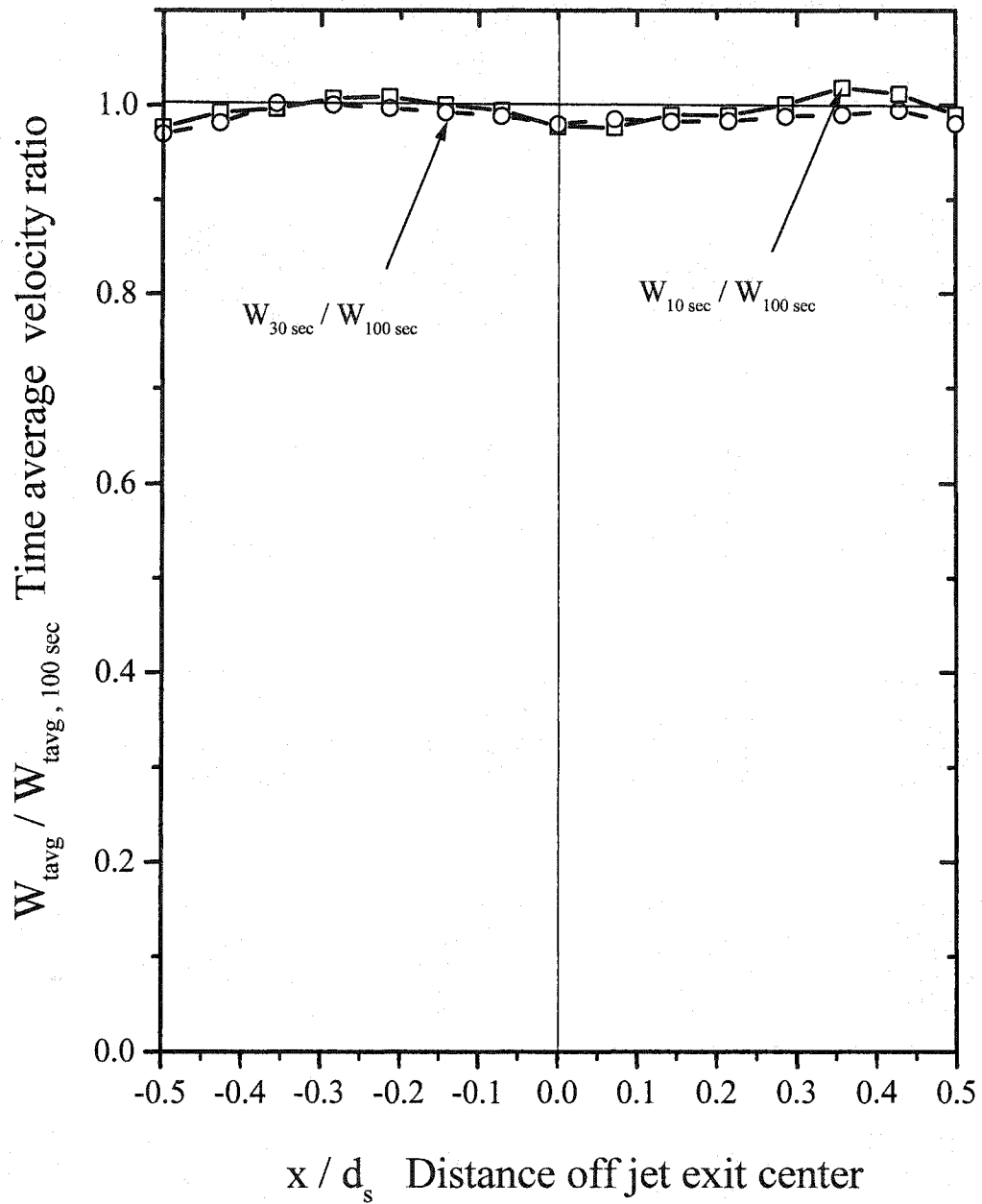


Figure 3.4 Effect of averaging time on the LDV measurements of source exit velocity for the $d_s = 12.7$ mm source with $W_{\text{avg}, 100 \text{ sec}} = 66$ mm / s on jet centerline.

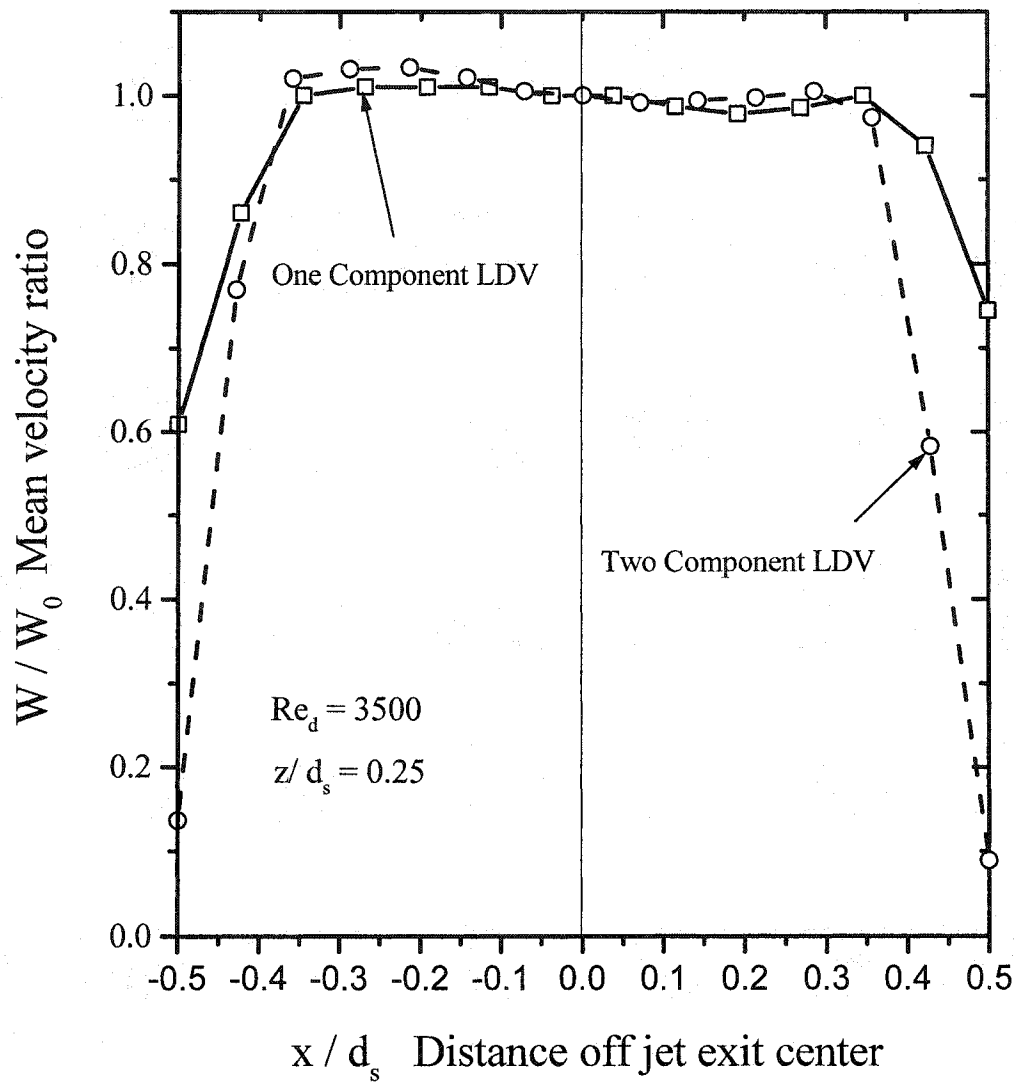


Figure 3.5 Mean velocity profiles measured with two different LDV systems. Source diameter $d_s = 12.7$ mm and $W_s = 270$ mm / s.

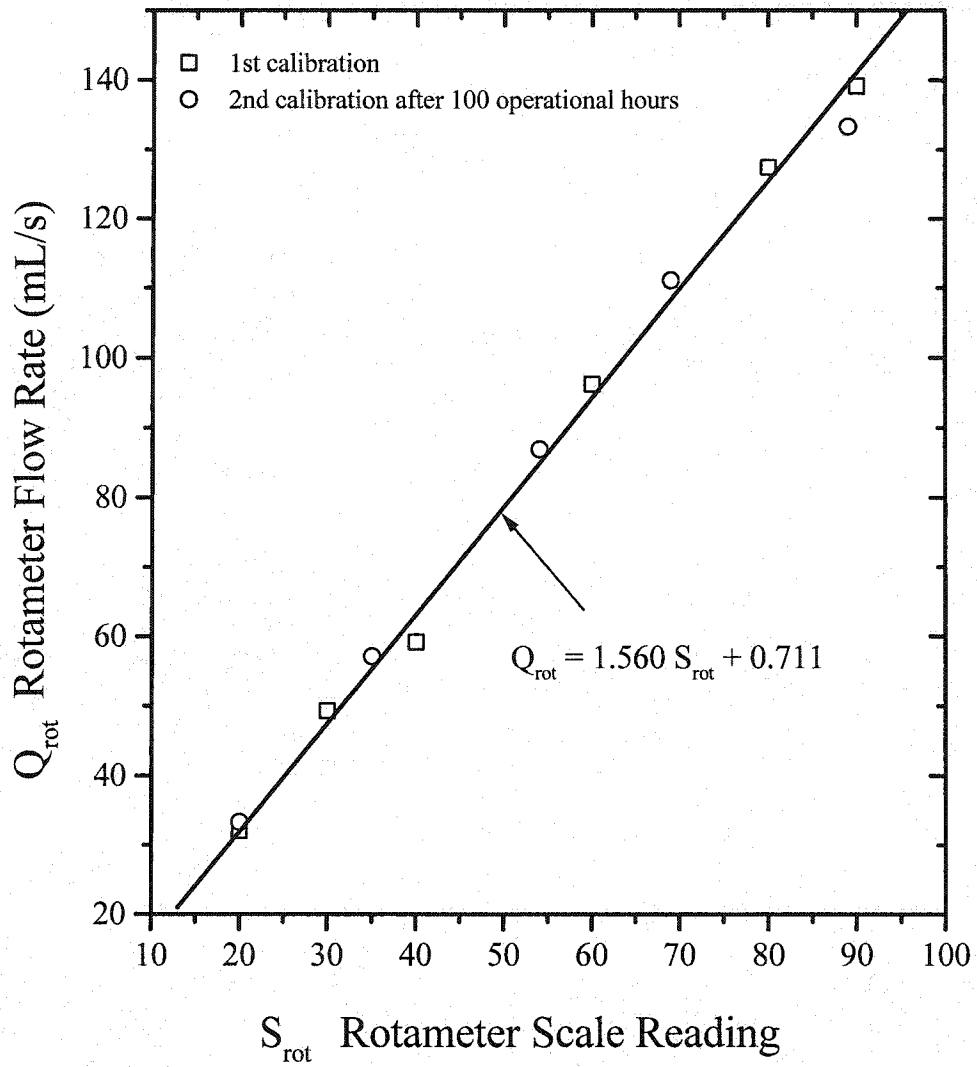


Figure 3.6 Calibration curve for the largest rotameter tube R-8M-25-4F-D.

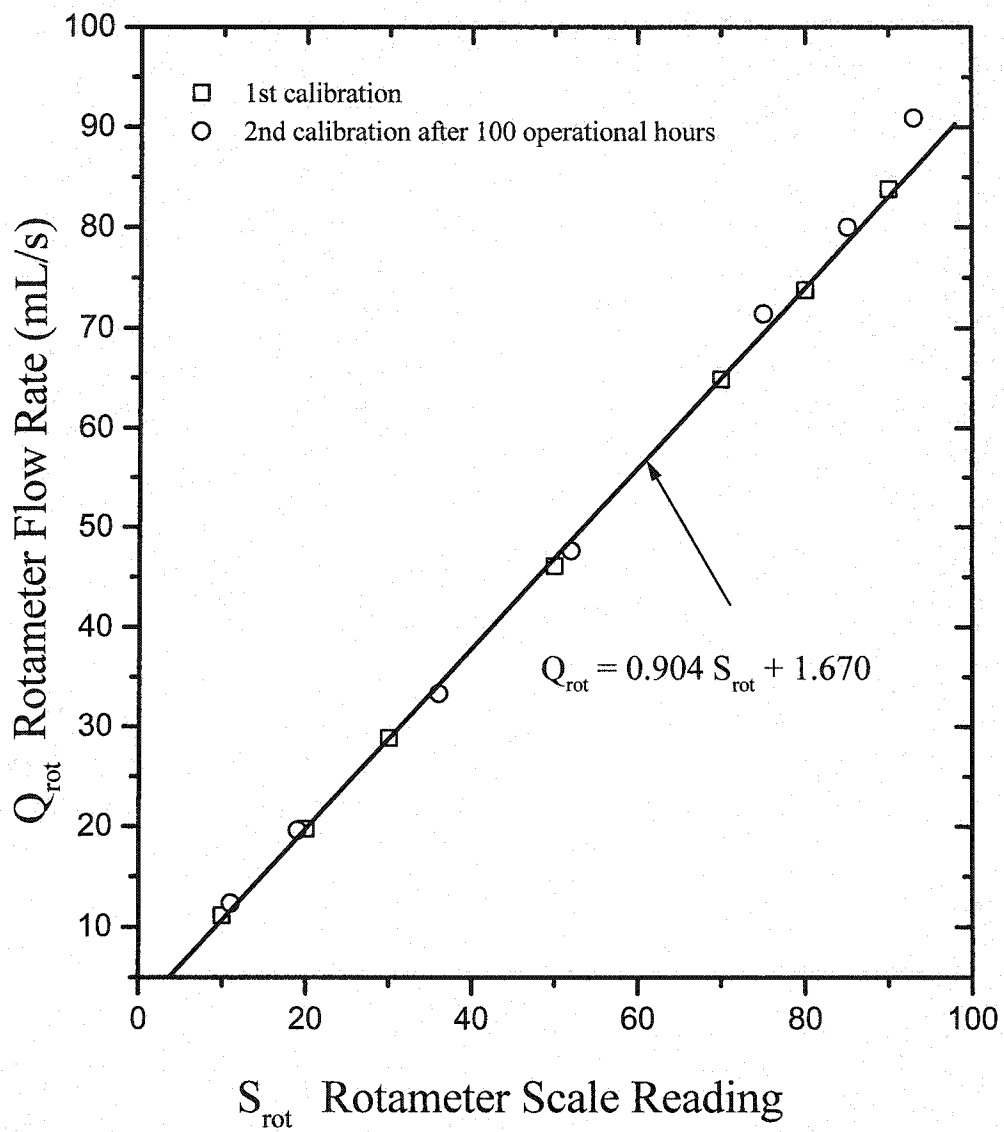


Figure 3.7 Calibration curve for the medium rotameter tube R-8M-25-4F-I.

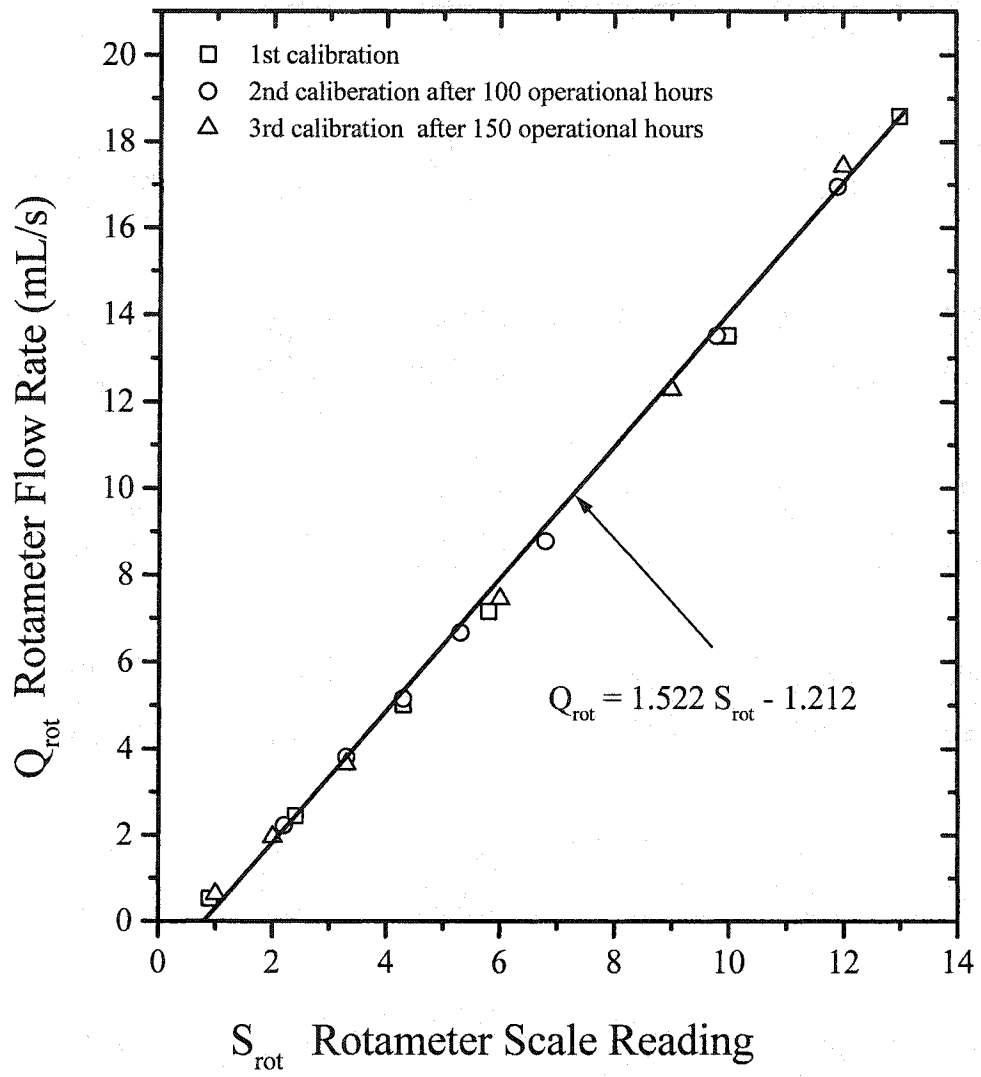


Figure 3.8 Calibration curve for smaller rotameter tube R-6-15-B.

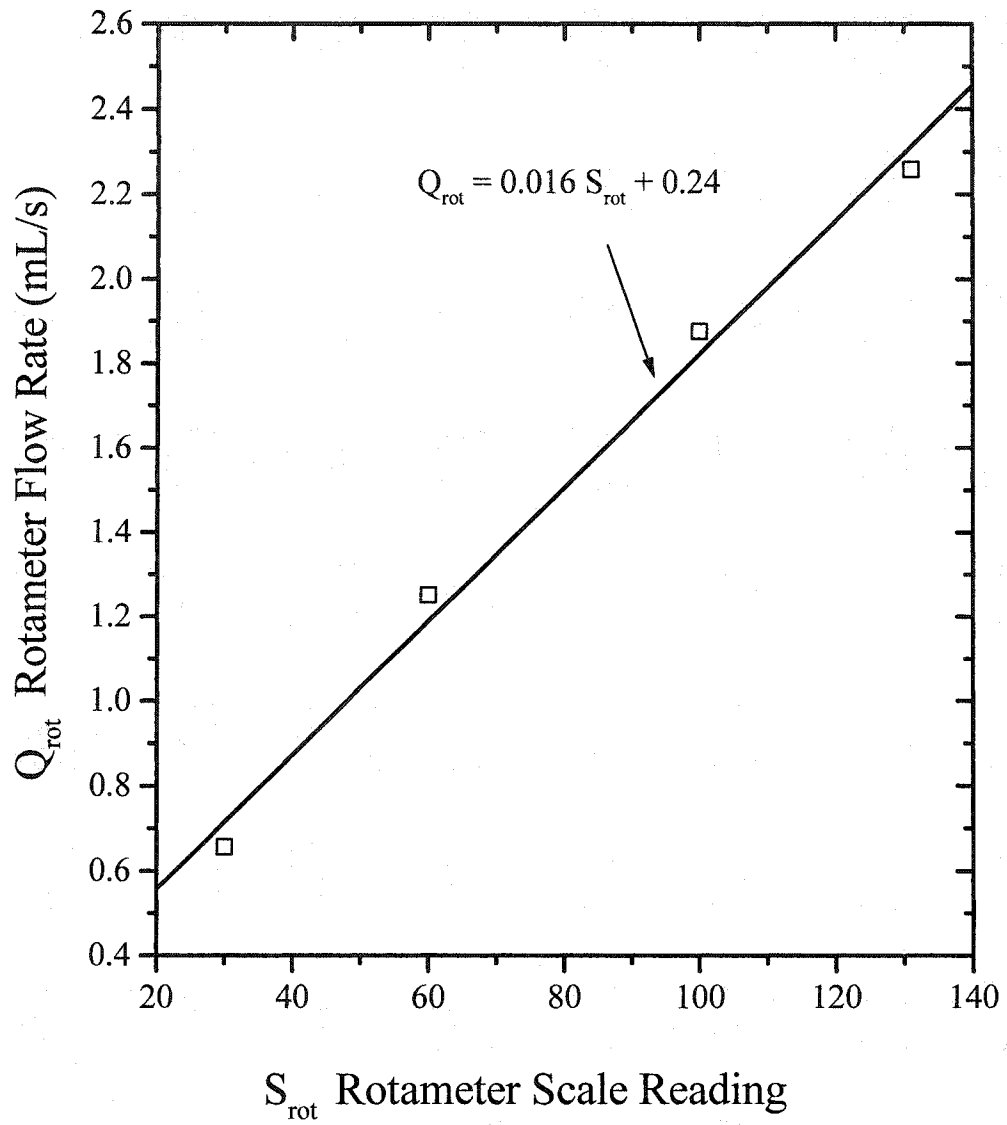


Figure 3.9 Calibration curve for the smallest rotameter tube R-603.

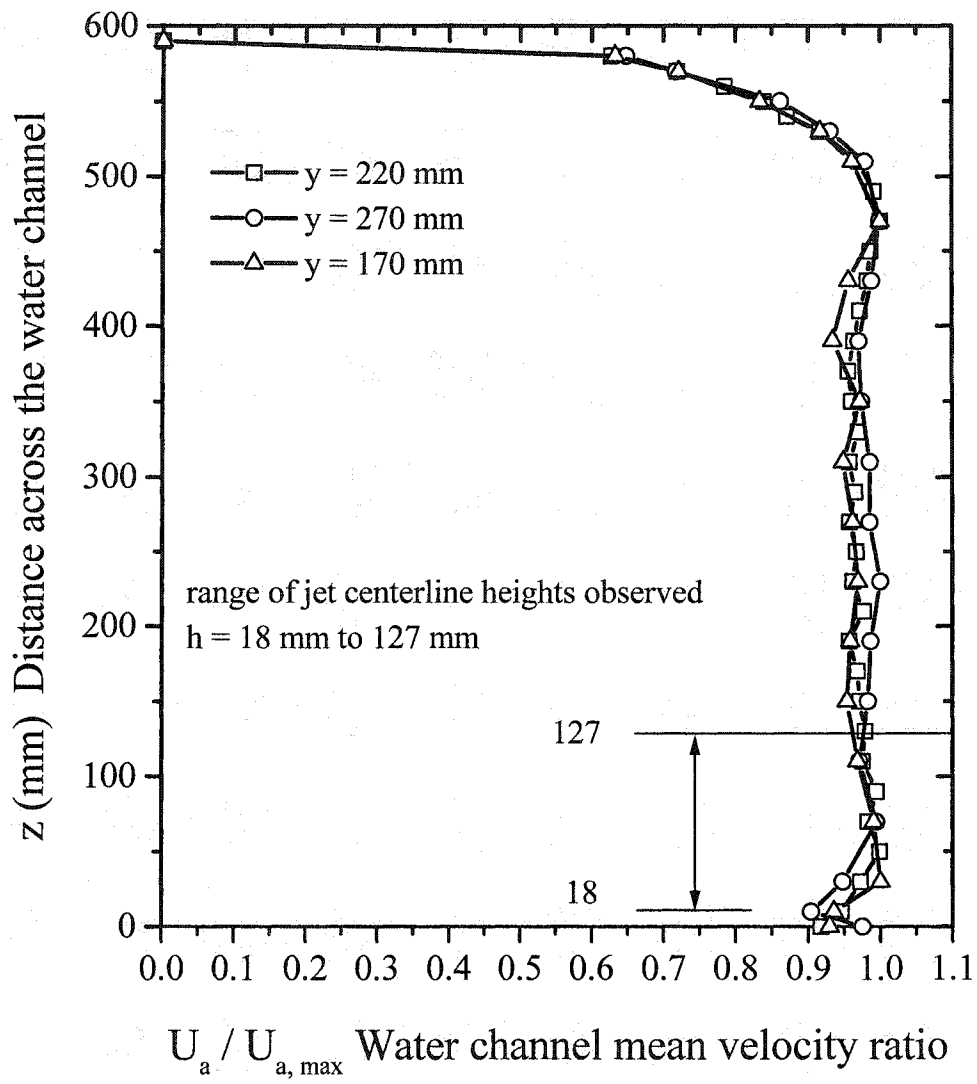


Figure 3.10 Water channel velocity profiles measured across the channel at three different heights.

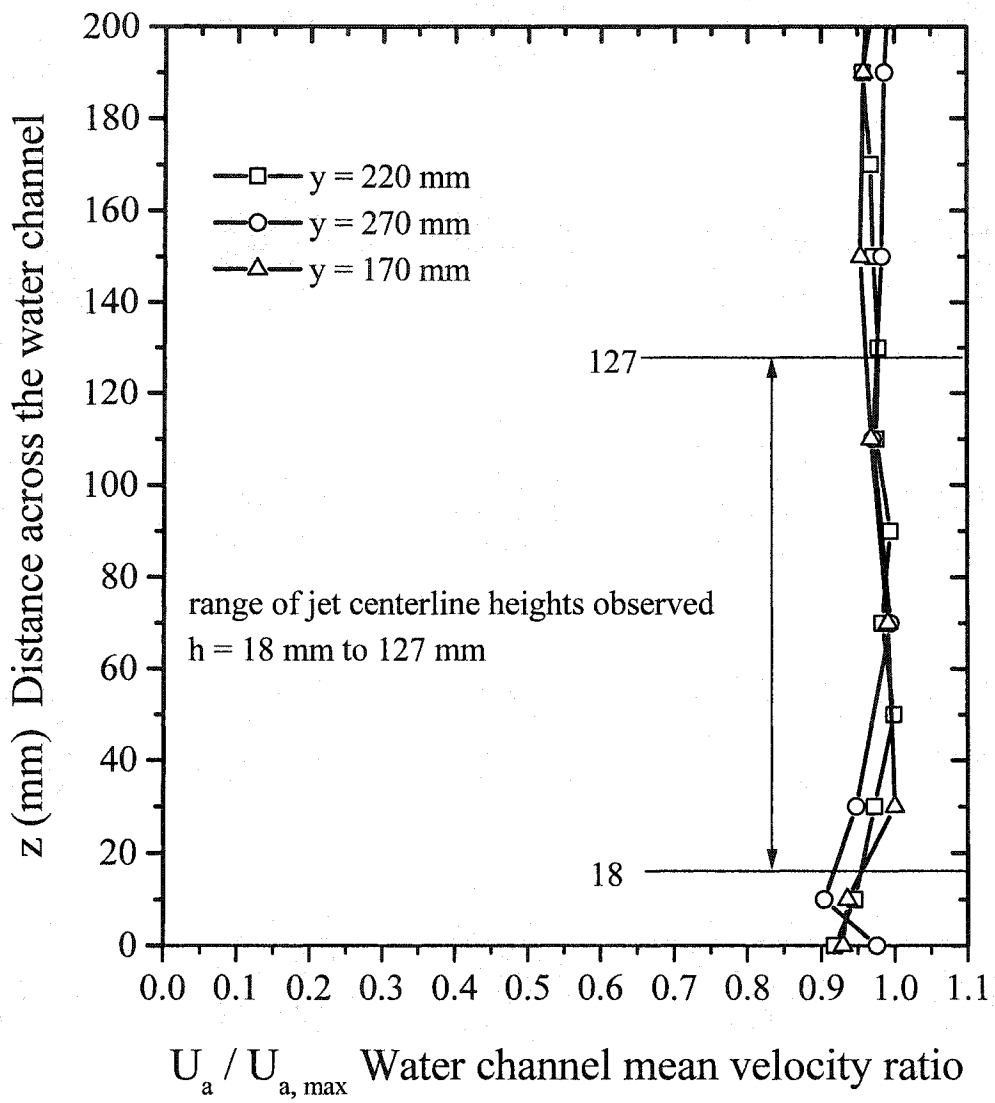


Figure 3.11 Water channel velocity profiles measured across the channel at three different heights.

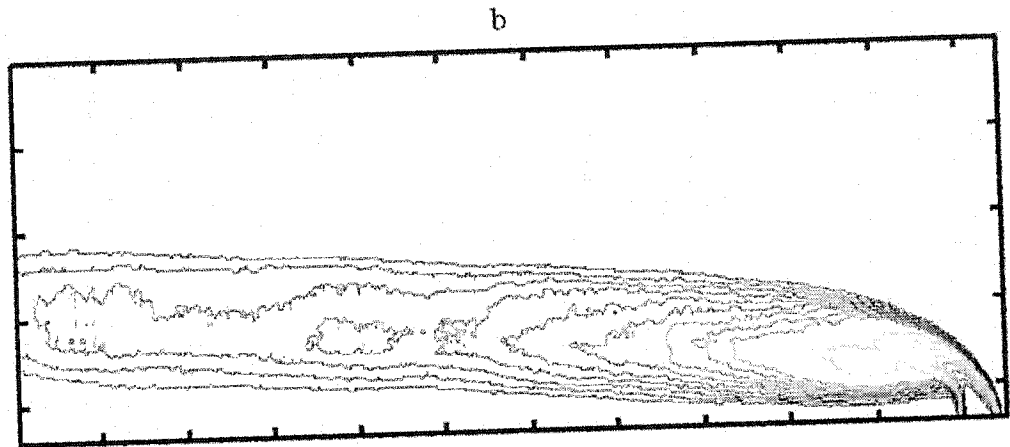
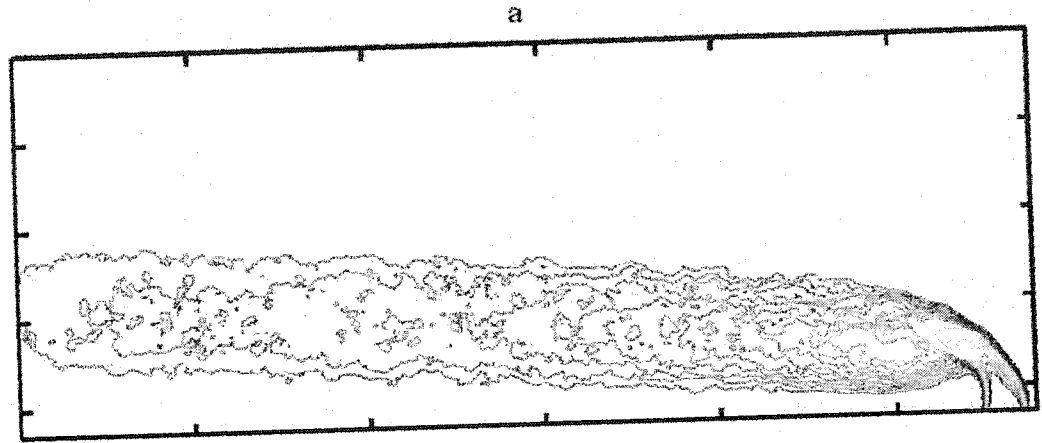


Figure 3.12a.b. Contour profiles of average images for the $d_s = 12.7$ mm source, produced from a) 200, b) 1200 consecutive images. $M = 4.0$, $Re_d = 9100$. The images are average of $1/30$ s video frame taken $1/6$ s apart (6 frames/s), in a crossflow with velocity $U_a = 180$ mm/s, which is 14 source diameter/s.

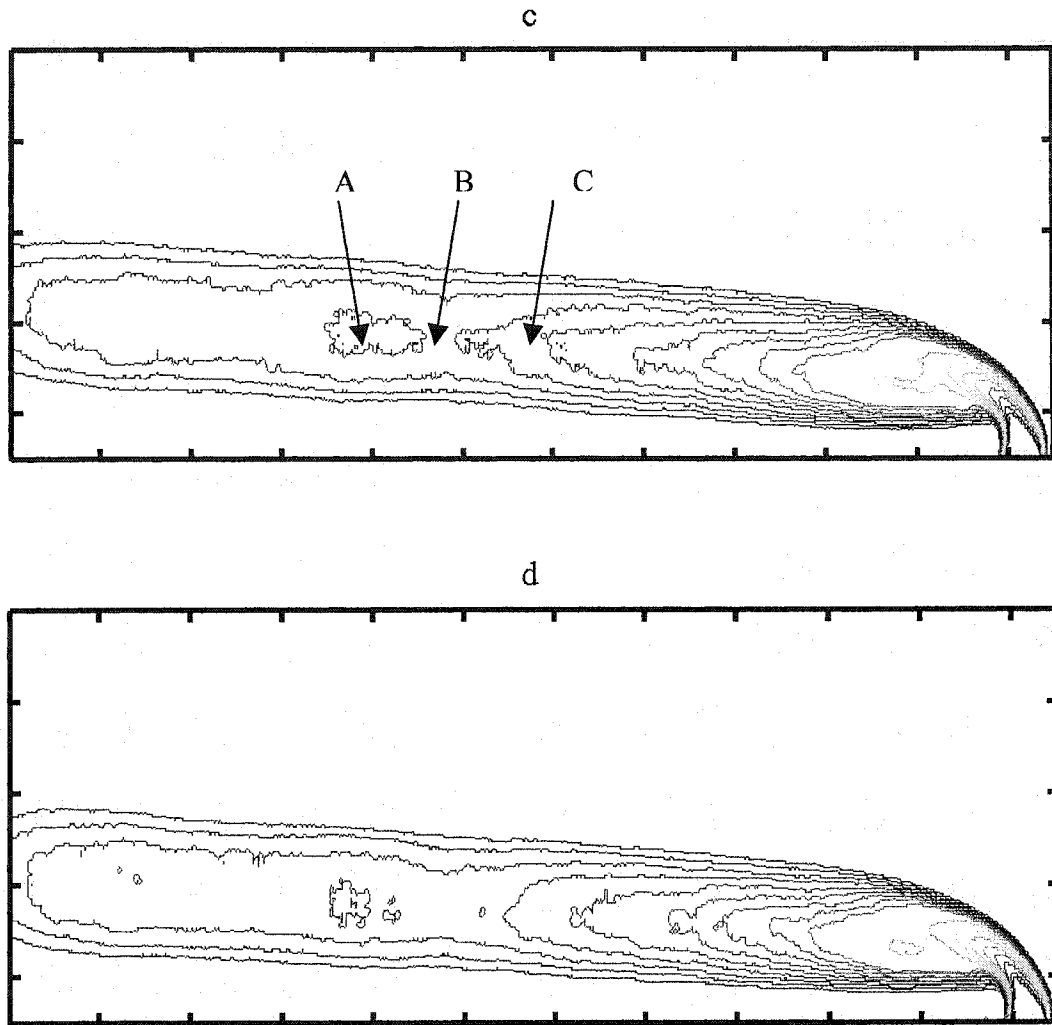


Figure 3.12c.d. Contour profiles of average images for the $d_s = 12.7$ mm source, produced from c) 1800, d) 2400 consecutive images. $M = 4.0$, $Re_a = 9100$. The images are average of $1/30$ s video frame taken $1/6$ s apart (6 frames/s), in a crossflow with velocity $U_a = 180$ mm/s, which is 14 source diameter/s.

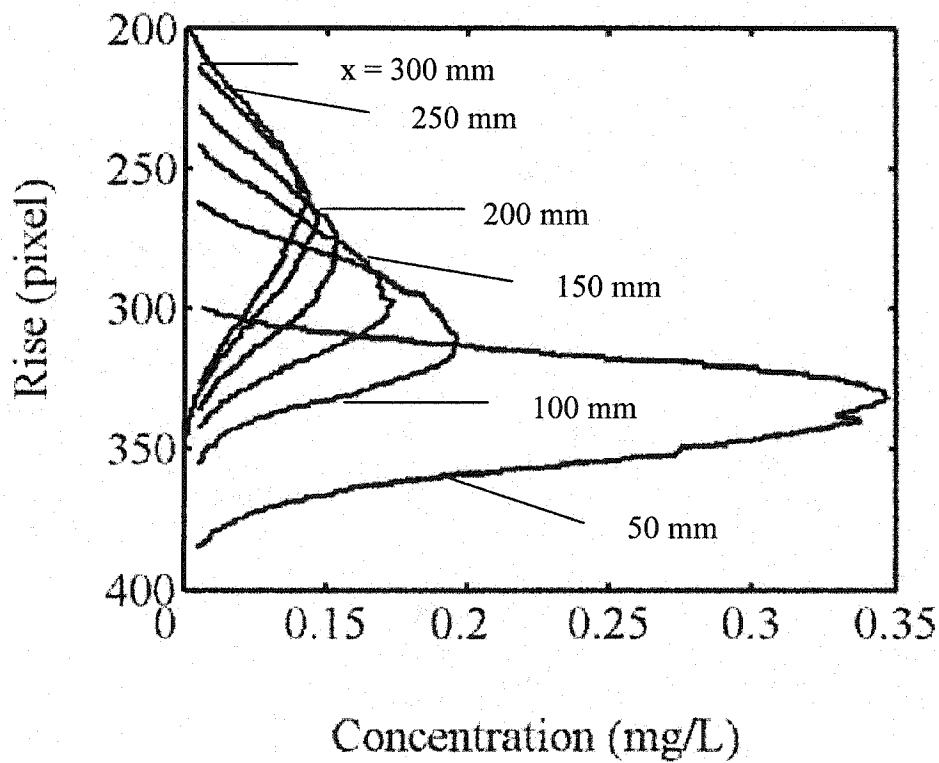
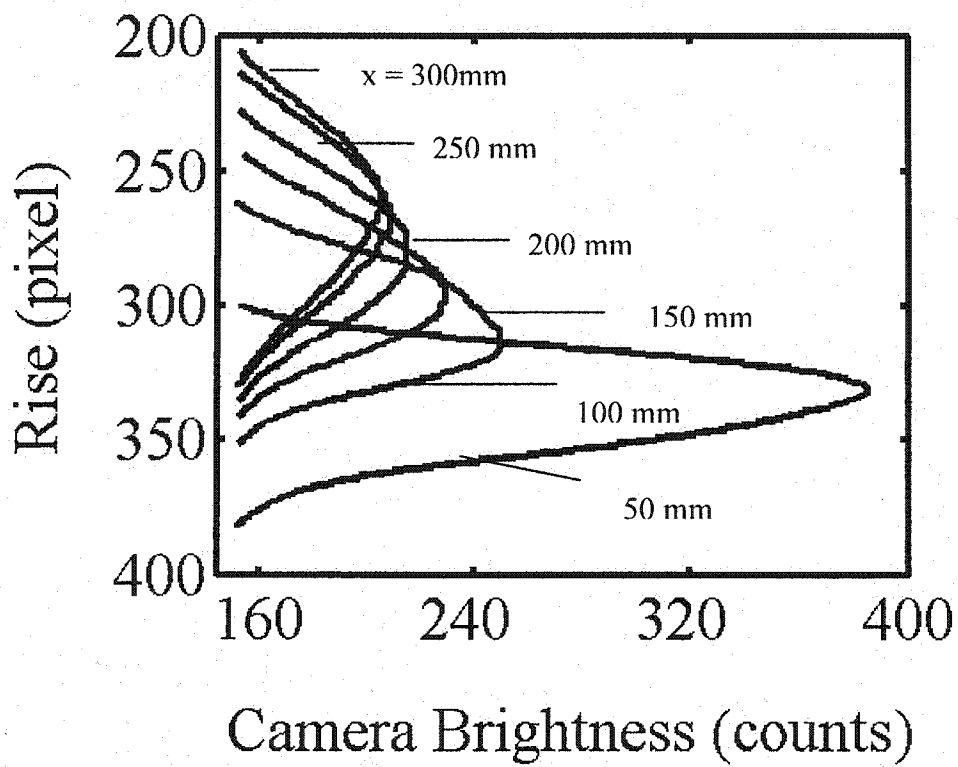


Figure 3.13 Profiles produced from concentration and intensity images. The rise height of pixel size is 0.5 mm/pixel.

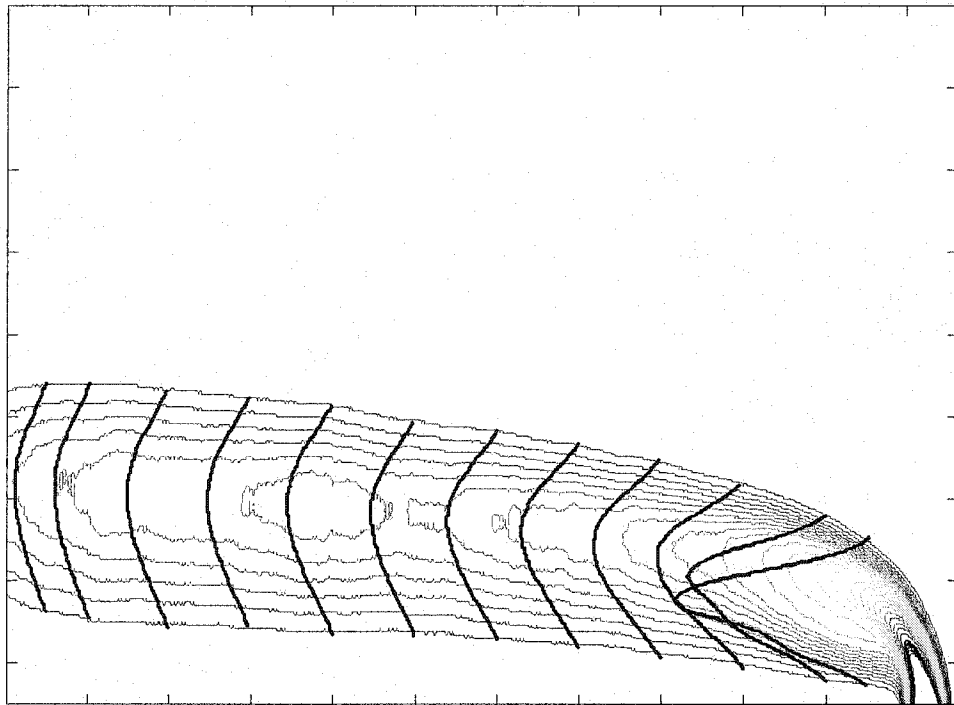


Figure 3.14 Concentration and contour profiles are shown together. Jet trajectory can be determined by joining the medians of these concentration profiles.

Chapter 4

Design of a Turbulent Jet Source

4.1 Introduction

A turbulent jet source was developed in this study to produce a turbulent jet with a flat exit velocity profile that was relatively independent of the jet Reynolds number. The jet produced by the source had approximately 10-15% turbulence intensity as the velocity ratio with the cross flow varied from 1 to 16. The effects of the initial conditions on the jet development were also studied.

In previous studies, experiments were done using a round tube or a machined nozzle as a source to produce a jet but there are few details of inner geometry of these sources. In their study, Kamotani and Gerber (1972) injected a surface jet in the cross flow with a 6 mm diameter nozzle. Andreopoulos and Rodi (1984) studied surface jets in a cross flow by producing a jet from a brass tube of 50 mm internal diameter. Alton et al. (1993) used round tubes of 5mm and 10mm diameter in their experiments to produce stack jets. Johnston and Wilson (1997) used a 8.8 mm inner diameter tube and an internal turbulence generator to produce a turbulent stack jet with a relatively flat exit velocity profile. Smith and Mungal (1998) in their study of surface jets in crossflows used a jet plenum arrangement with an inside diameter of 16 cm and a nozzle diameter varying from 2 mm to 20 mm.

Table 4.1 shows all the experiments done with the LDV.

4.2 Source design

In the present study, several different design options were built and tested. Simplicity was an important factor in the source design because with a simple design it was easy to build a larger or smaller source with exactly the same geometry. Three different source sizes with $d_s = 3.175$ mm, 12.7 mm and 25.4 mm were fabricated and compared. Initially a "very large" exit diameter ($d_s = 25.4$ mm) source was designed and fed by an external manifold of 4 plastic tubes. The "large" source and some of its dimensions are shown in Figure 4.2.

Figure 4.1 compares the two outlet nozzle sizes: $d_s = 25.4$ mm of the "very large" source and $d_s = 12.7$ mm of the "large" source. It is obvious from Figure 4.1 that the jet velocity profile from the source, $d_s = 25.4$ mm, is not as uniform as that of the source $d_s = 12.7$ mm. With only a 4:1 area contraction there was not enough room for the fluid to mix uniformly inside the mixing chamber and the result was that non-uniform profile for the 25.4 mm jet. Therefore that "very large" source was replaced with a "large" source with $d_s = 12.7$ mm diameter nozzle to give a 16:1 area contraction from mixing chamber.

The reason for initially choosing the larger source was that an LDV system was used to measure the mean velocity profiles. The diameter of the laser beam at crossing was 1 mm. Hence, a source with the large enough nozzle diameter was built so that there would be enough spatial resolution available to have precise measurements above that source. A "small" source, with all dimensions reduced by a factor of 4 from the "large" source, was also built. The results from "large" and "small" source were compared to see

if the scaling geometry of the source mixing chamber and inlet distribution plenum had any effects on the jet properties.

Before finalizing the source in Figure 4.2, several other options were also tested. As shown in Figure 4.2, fluid entered in the inner mixing chamber through four inlet holes. Without any obstacle between the incoming jets, the impinging jets were unstable, produced a non-uniform velocity profile across the nozzle exit. To produce uniform flat exit velocity profiles for Reynolds numbers of 200 to 10,000, two different center-body shapes were tested as obstacles to stabilize the four incoming jets. One of these obstacles had a conical-shape and the other was cross-shaped. Figure 4.3 shows the velocity profiles of the jets coming out of the exit nozzle. The profile with the conical shaped center-body is more uniform and closer to the ideal uniform profile than with the cross shaped center-body. The cone shaped stabilizer shown in Figure 4.2 was used in the final design. The cone shaped center-body had the additional advantage that it was easier to build in the reduced scale of the "small" scale $d_s = 3.175$ mm source, and easier to align than the cross shaped center-body.

4.2.1 Inlet holes for turbulence generation

The function of the mixing chamber inlet holes shown in Figure 4.2 was to produce a high level of turbulence intensity inside the mixing chamber. To select the proper size of the inlet holes that fed the mixing chamber, two different sizes $d_{in} = 6.35$ mm and $d_{in} = 3.175$ mm were tested. The small size inlet holes increased the velocity of the fluid entering into the inner mixing chamber, which eventually would produce a high level of turbulence intensity inside the chamber. As expected, Figure 4.4 shows that the 3.175 mm diameter hole produced more turbulence intensity without any

loss of exit velocity uniformity. The small inlet holes $d_{in} = 3.175$ mm were used in the final design.

To supply the fluid from main supply to the inlet holes, two different kinds of inlet supply systems were used. The one system was made of four flexible tubes of 6 mm diameter connected to the inlet holes of the mixing chamber. These tubes had equal length. The other system was a plenum design. Figure 4.5 is the comparison of the velocity profiles of the jet from these two setups. The difference between the velocity profiles from these systems was minor ($< 5\%$) for all Reynolds numbers except at the lowest Reynolds number 370, where it was approximately 10%. Hence it shows that the way fluid was supplied to the jet inlets did not have a significant effect on the jet exit velocity profiles. The reason for selecting an internal plenum rather than an external hose manifold was that it was convenient for the source to be designed at different size scales.

4.2.2 Jet symmetry

To confirm that the jet was symmetric, the velocity profiles were measured in two different planes by rotating the source 90° each time to repeat the measurements a second time. As shown in Figure 4.6, these two planes were measured at an angle $\theta = 45^\circ$ to the inlet holes. Figure 4.6 shows that all these velocity profiles are similar to each other which means that the flow is symmetric with no bias due to the inside conditions of the source. Figure 4.7 shows the velocity profiles measured at different Reynolds number ranging from 370 to 10,000. These profiles were measured for both "large" and "small" sources, $d_s = 12.7$ mm and $d_s = 3.175$ mm, above the source. All these profiles are almost identical and only weakly dependent on the jet Reynolds

number. For the LDV, the closest distance possible above the small source was $z=3.175$ mm . For comparison velocity profiles were measured at $z = 12.7$ mm (one diameter) above the large source $d_s=12.7$ mm . Figure 4.8 shows the comparison with good agreement between them except at the edges. The probable reason for the difference was that diameter of the measuring laser beam was 1/3 of the small source exit diameter d_s , giving poor spatial resolution above the small source.

4.2.3 Jet turbulence intensity

Effects of jet turbulence on the mean velocity exit jet profiles were studied for the "large" ($d_s=12.7$ mm) source. The jet turbulence intensity was reduced by placing a very fine copper screen between the inner mixing chamber and the jet nozzle. The copper screen was made of 0.064 mm wires with a 0.101 mm spacing between them. Figure 4.9 shows the comparison of mean velocity profiles measured with and without the copper screen. As shown in Figure 4.9, the difference between these two mean velocity profiles is about 3% when the turbulence intensity was reduced to 2% with the screen, compared to roughly 10% without screen.

4.3 Velocity profile shape correction for momentum flux

The velocity ratio in Equation 2.20 is based on the assumption that the source exit velocity was a uniform top-hat profile. This means that the average velocity could be used in the calculation of both the mass and the momentum fluxes. As shown in the previous section, the source exit velocity profiles were not quite uniform. In order to use the average source exit velocity in momentum calculations, a momentum correction

factor, α_m , was included in Equation 2.20 for momentum flux. Two different methods were used to calculate this correction factor.

4.3.1 Direct numerical integration for momentum

A direct numerical integration of the measured velocity profiles were used to calculate the momentum correction factor. The momentum correction factor is defined by

$$\alpha_m = \frac{\sum_{i=1}^{i=N} \rho W^2 2\pi r \Delta r}{\rho \bar{W}^2 \pi R_s^2} \quad (4.1)$$

where $\Delta r = (R_{s_{i+1}} - R_{s_i})$ and \bar{W} is defined using

$$\bar{W} = \frac{\sum_{i=1}^{i=N} W 2\pi r \Delta r}{\pi R_s^2} \quad (4.2)$$

The average velocity \bar{W} of the velocity profile was calculated by numerical integration using the trapezoidal rule which expresses W as

$$W = W_i + \left(\frac{W_{i+1} - W_i}{R_{s_{i+1}} - R_{s_i}} \right) (r - R_{s_i}) \quad (4.3)$$

4.3.2 Ramp profile integration for momentum

Another method was used to calculate the momentum correction factor α_m . As shown in Figure 4.10, velocity profile is divided into two regions, a core and an outer shear layer. The velocity in the core region is the centerline velocity W_0 and is constant. In the shear layer region velocity is calculated as

$$W_{sl} = \frac{W_0}{2\delta} (R_s + \delta - r) \quad (4.4)$$

where δ is the shear layer thickness. The volume flow rate in the shear layer region is

$$Q_{shear\ layer} = \rho \int_{r=R_s-\delta}^{r=R_s+\delta} W_{sl} 2\pi r dr \quad (4.5)$$

where the shear layer velocity W_{sl} is defined as

$$W_{sl} = \frac{W_0}{2\delta} (R_s + \delta - r) \quad (4.6)$$

volume flow in the core region is

$$Q_{core} = \rho \int_{r=0}^{r=R_s-\delta} W_0 2\pi r dr \quad (4.7)$$

substituting Equation 4.6 into Equation 4.5

$$Q_{shear\ layer} = \rho \int_{r=R_s-\delta}^{r=R_s+\delta} \frac{W_0}{2\delta} (R_s + \delta - r) 2\pi r dr \quad (4.8)$$

The volume flow rate coming out of the source is equal to the sum of the volume flow rate of the core and the shear layer region.

$$Q_s = Q_{core} + Q_{shear\ layer} \quad (4.9)$$

$$Q_s = \rho \alpha_m W_s^2 \pi R_s^2 \quad (4.10)$$

substituting Equations 4.7, 4.8 & 4.10 into 4.9

$$\rho \alpha_m W_s^2 \pi R_s^2 = \left(\rho \int_{r=0}^{r=R_s-\delta} W_0 2\pi r dr \right) + \left(\rho \int_{r=R_s-\delta}^{r=R_s+\delta} \frac{W_0}{2\delta} (R_s + \delta - r) 2\pi r dr \right) \quad (4.11)$$

integrating Equation 4.11 and simplifying the terms yields

$$\alpha_m W_s^2 \pi R_s^2 = \pi W_0^2 (R_s - \delta)^2 + \frac{8}{3} \pi W_0^2 \delta (R_s - \delta) \quad (4.12)$$

where

$$W_{s,avg}^2 = \frac{\int_0^{R_s} W_0^2 2\pi r dr}{\pi R_s^2} \quad (4.13)$$

From Equation 4.12, the momentum correction factor values can be calculated.

This correction is also used in other studies such as Neiman (1979), Johnston and Wilson (1997) and Fabris (1998). The extreme values of α_m would be 2.0 for a laminar parabolic profile and 1.0 for a uniform flat profile.

This appears in Equation 2.20 for the corrected velocity ratio

$$M = \alpha_m^{1/2} \left(\frac{\rho_s}{\rho_a} \right)^{1/2} \left(\frac{W_s}{U_a} \right) \quad (4.14)$$

Figure 4.11 shows the measured variation of the momentum factor α_m with respect to Reynolds number in the present study. The momentum correction factor values calculated from the direct numerical integration method were between 1.0 and 1.1 for all Reynolds number except $Re_d = 373$ where $\alpha_m = 1.17$. On the other hand, the momentum correction factor values from the ramp profile method were between 1.2 and 1.3. The values of α_m calculated from the direct numerical integration method are 5 to 16% higher than the ideal value of α_m , which is 1. On the other hand, values of α_m calculated from the ramp profile method are always 20 to 30% higher than the ideal value of α_m . In the rest of the present study the direct numerical integration method was used to calculate the momentum correction factor values. The momentum correction term was included in the calculations to determine the flow rates used in the experiments to produce the desired value of M in Equations 4.14 and 2.20.

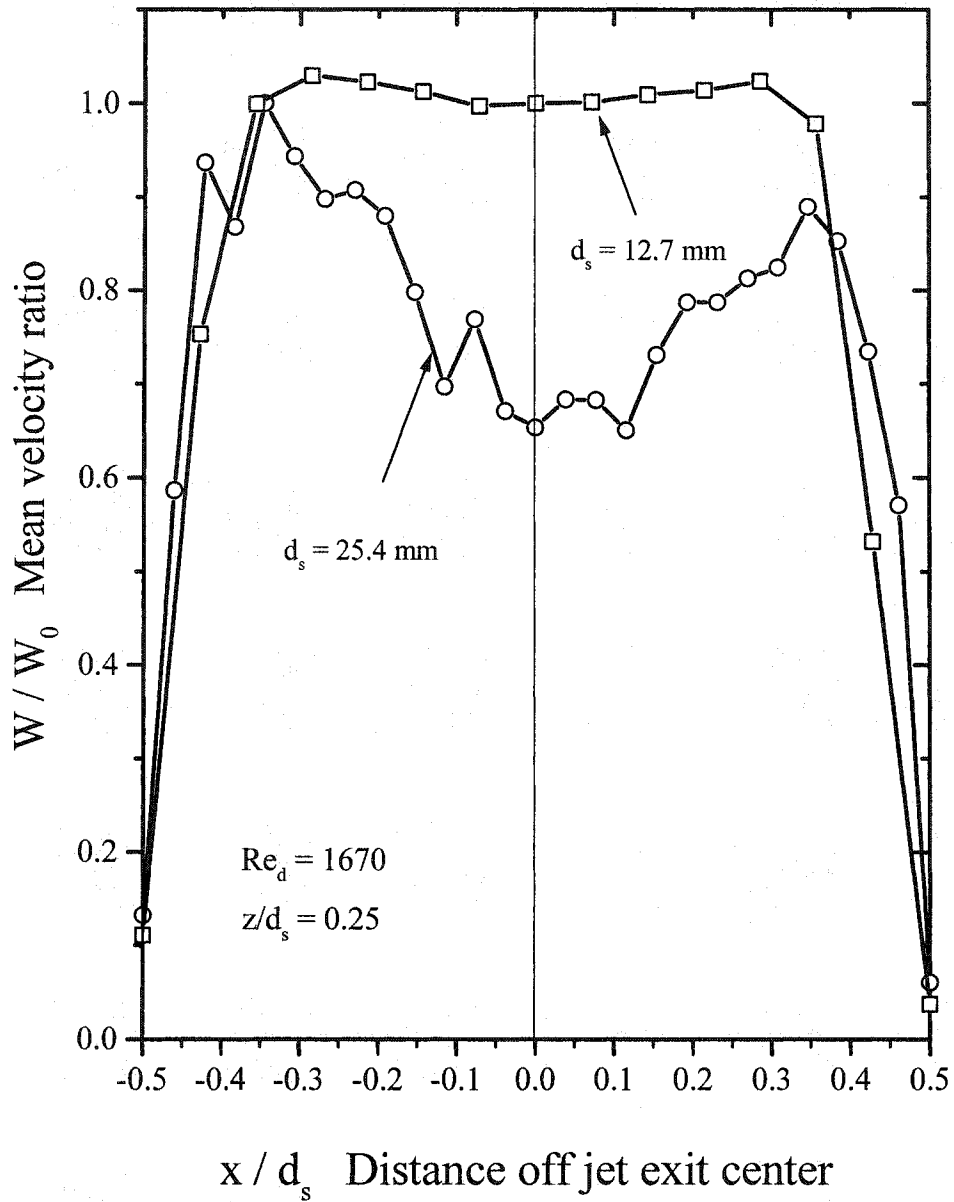


Figure 4.1 Mean velocity profile with exit nozzle diameter , $d_s = 25.4$ mm and 4:1 area contraction is non uniform compared to $d_s = 12.7$ mm and 16:1 area contraction from the 50.8 mm diameter mixing chamber

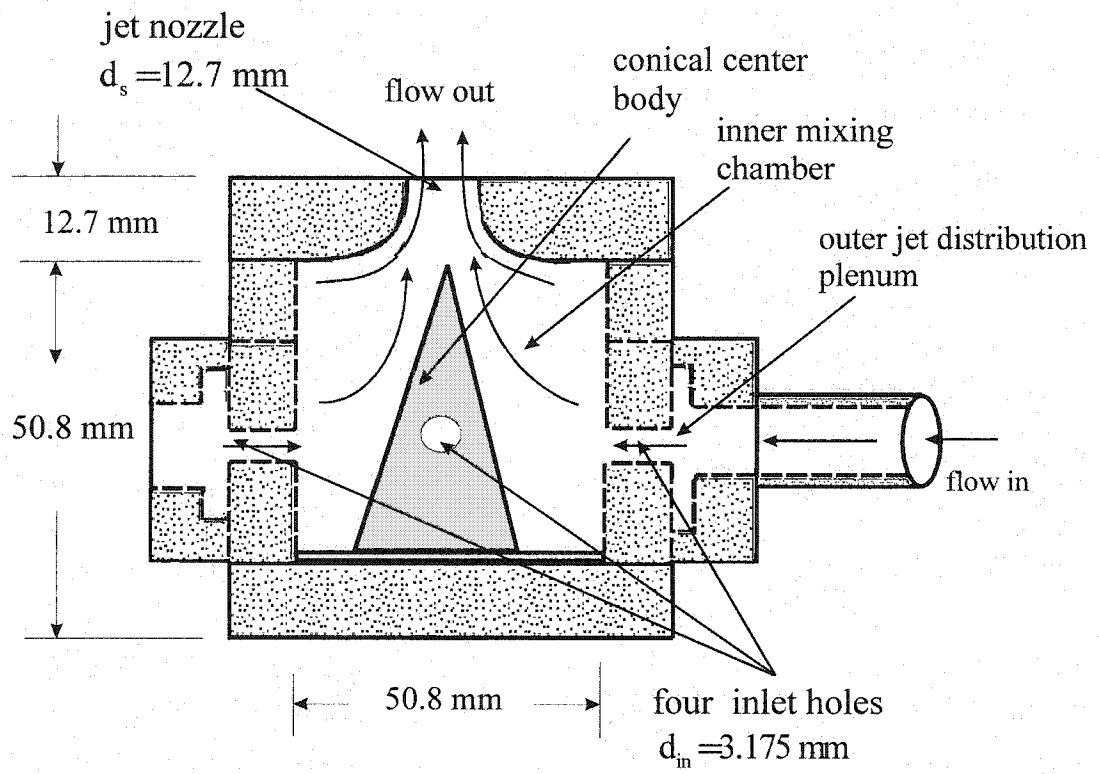


Figure 4.2 Vertical sectional view of the source

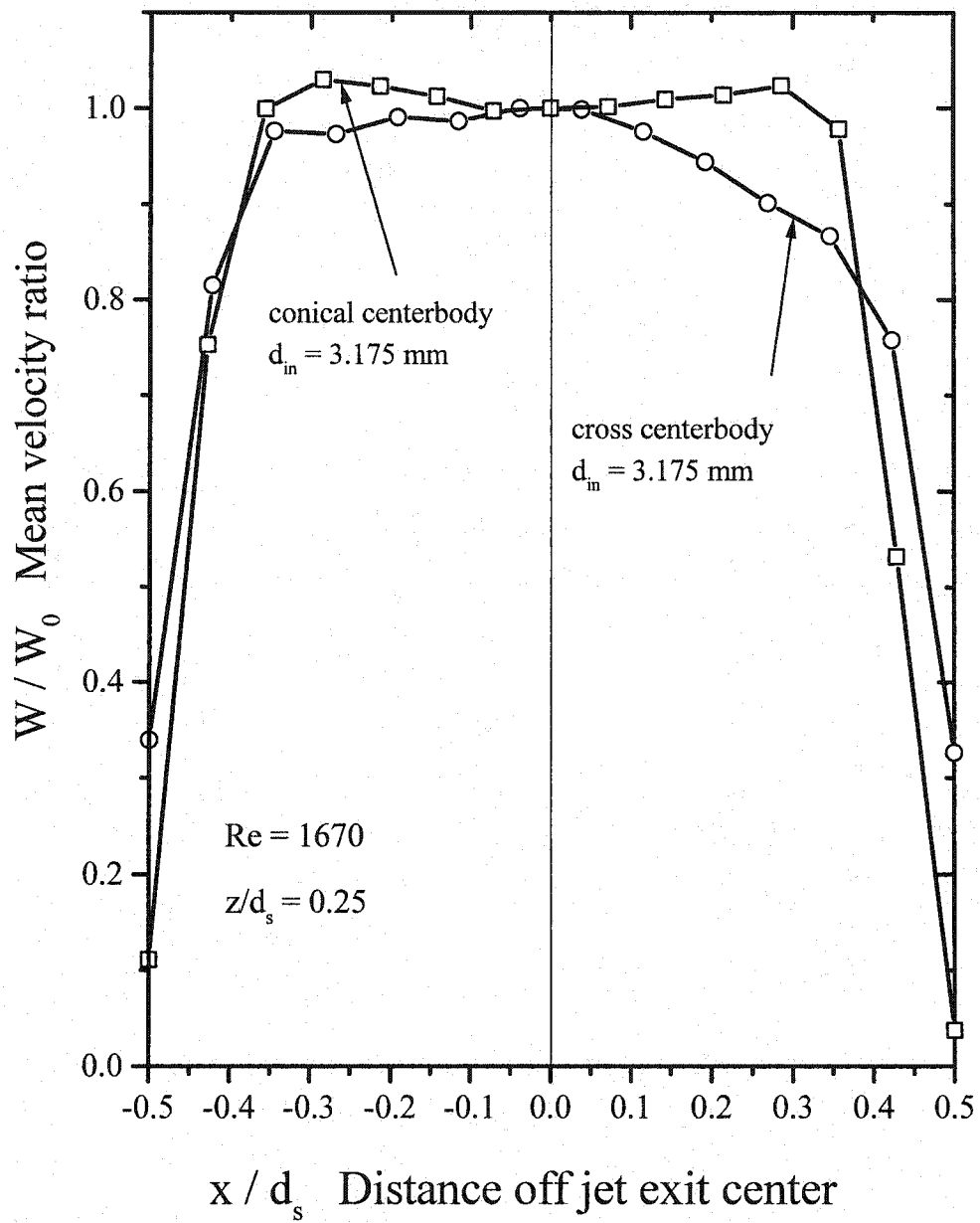


Figure 4.3 Mean velocity profile of the jet with the conical center-body is more uniform than the mean velocity profile of the jet with the cross center-body. Source diameter $d_s = 12.7$ mm.

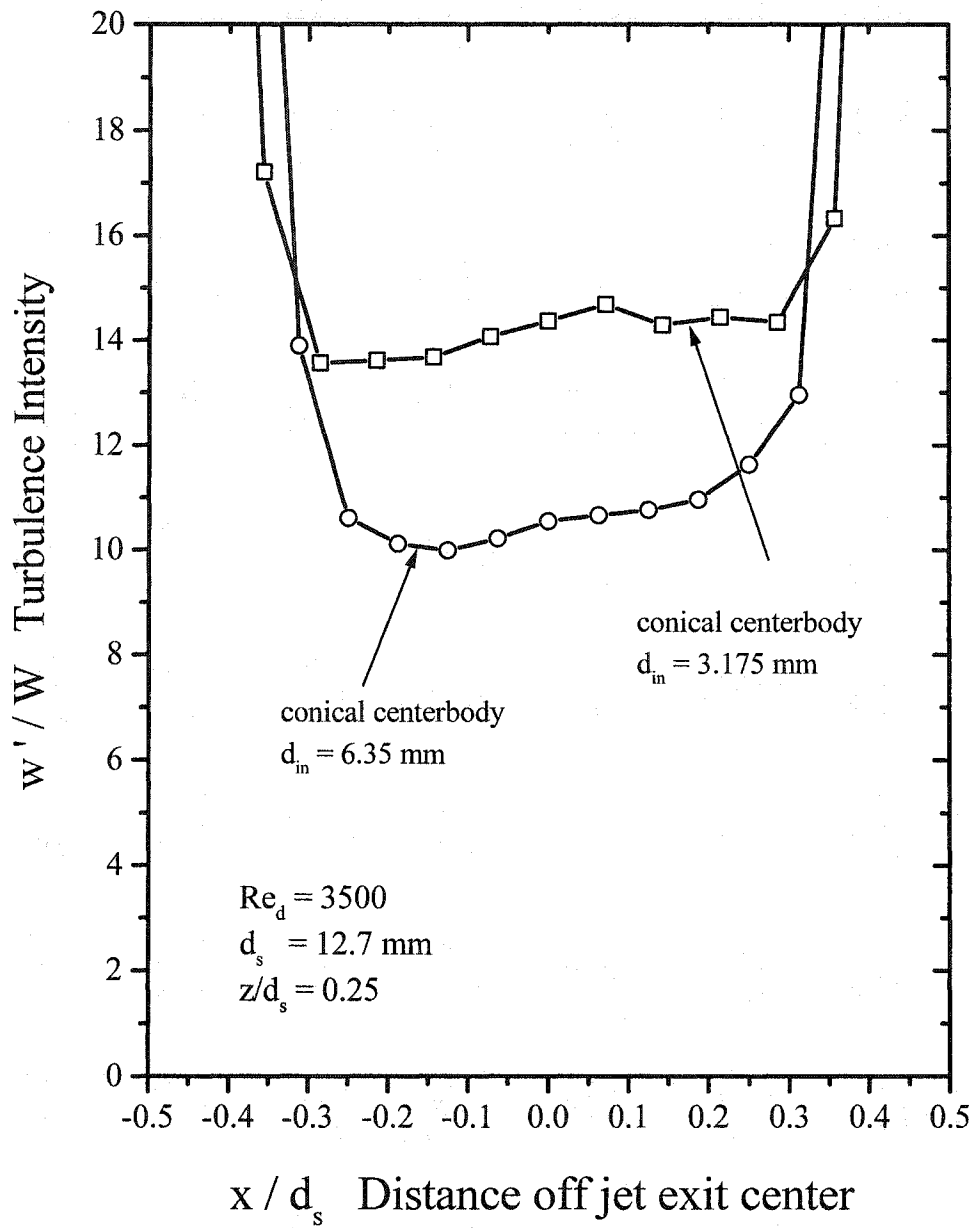


Figure 4.4 Turbulence intensity at jet exit is higher with small diameter inlet holes in the mixing chamber, $d_{in} = 3.175$ mm.

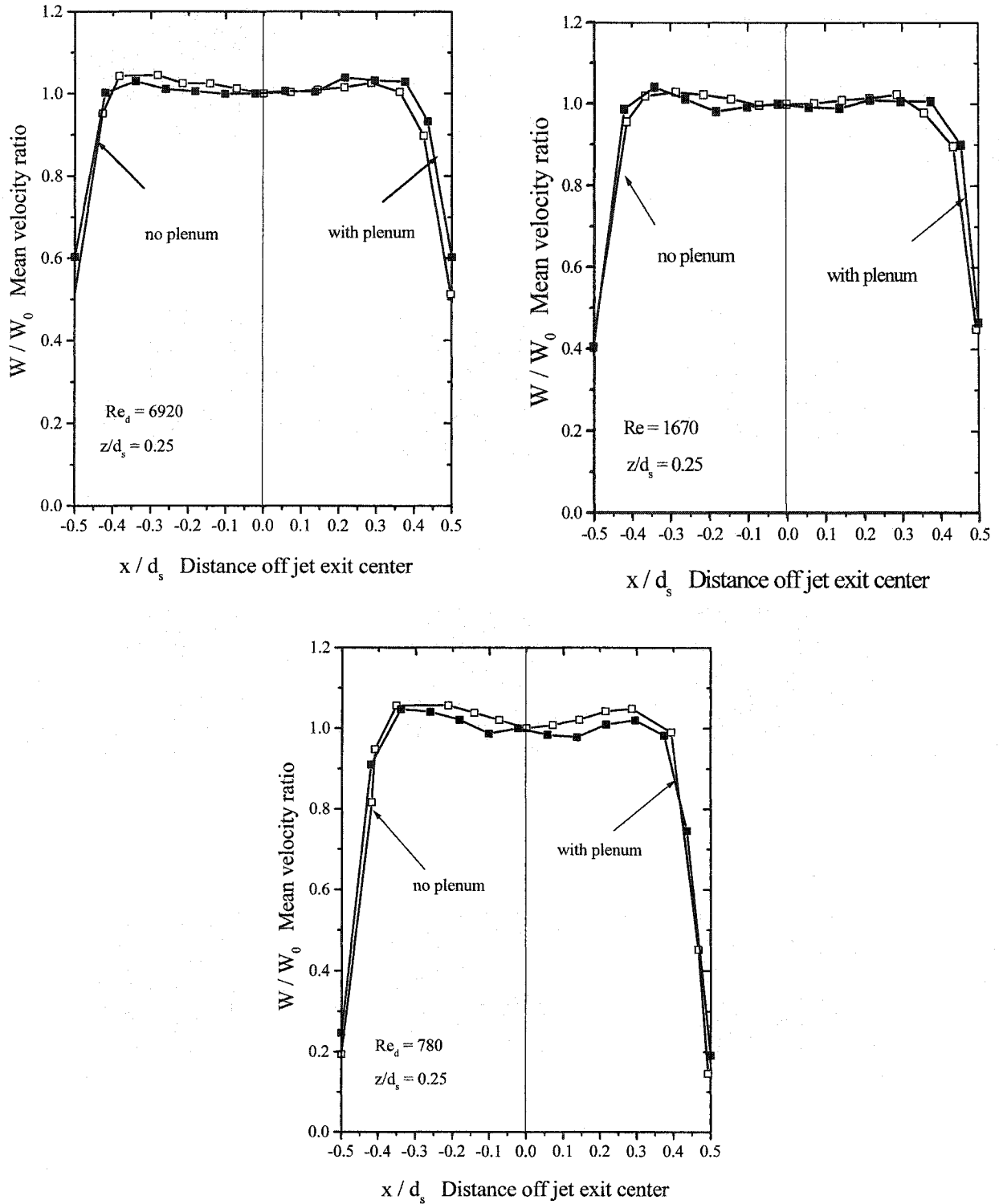


Figure 4.5 Mean velocity profiles are almost identical with and without an inlet plenum chamber. Source diameter $d_s = 12.7$ mm.

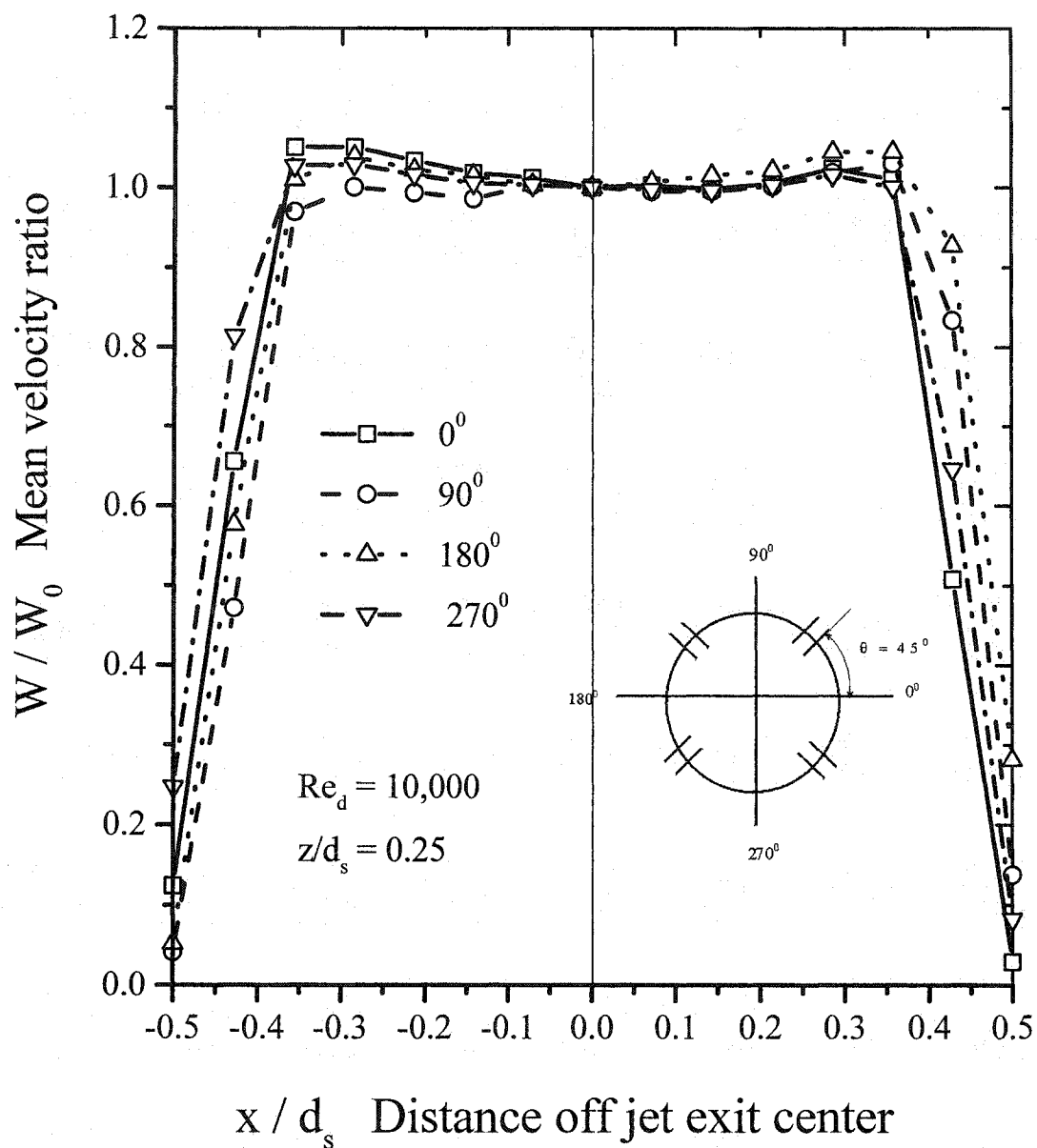


Figure 4.6 Mean velocity profiles measured at four different planes above the source are similar, which means that the jet is symmetrical. That plane is at 45° angle to the Inlet hole. Source diameter, $d_s = 12.7$ mm.

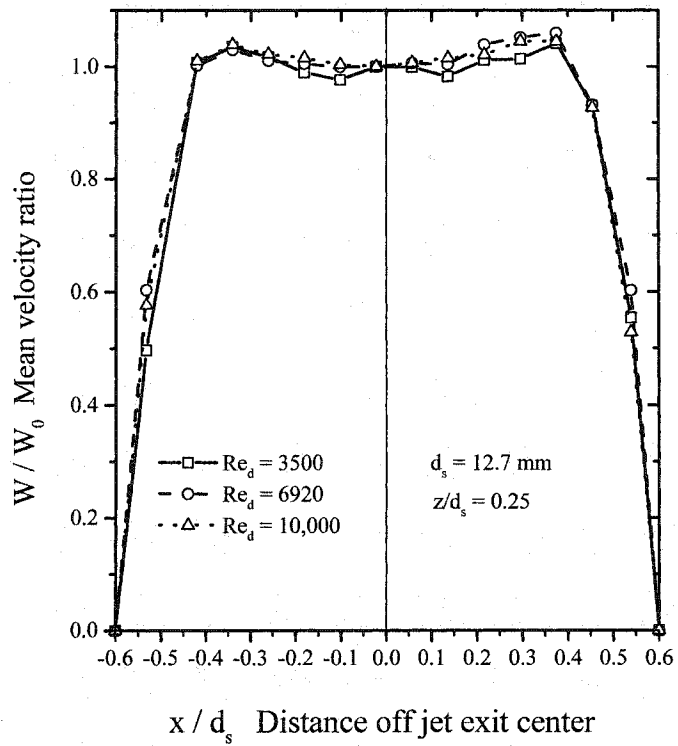
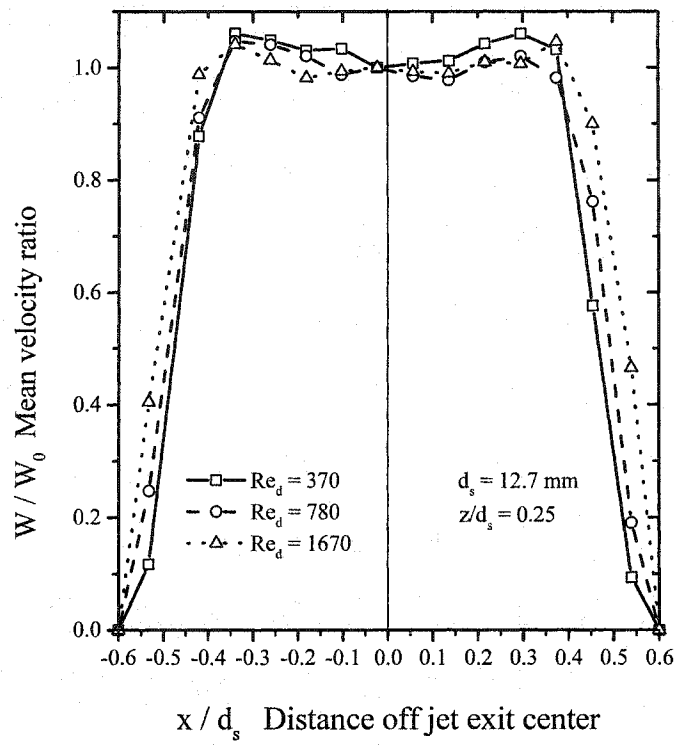


Figure 4.7 Mean velocity profiles measured for several jet Reynolds numbers show a weak dependence on Reynolds number

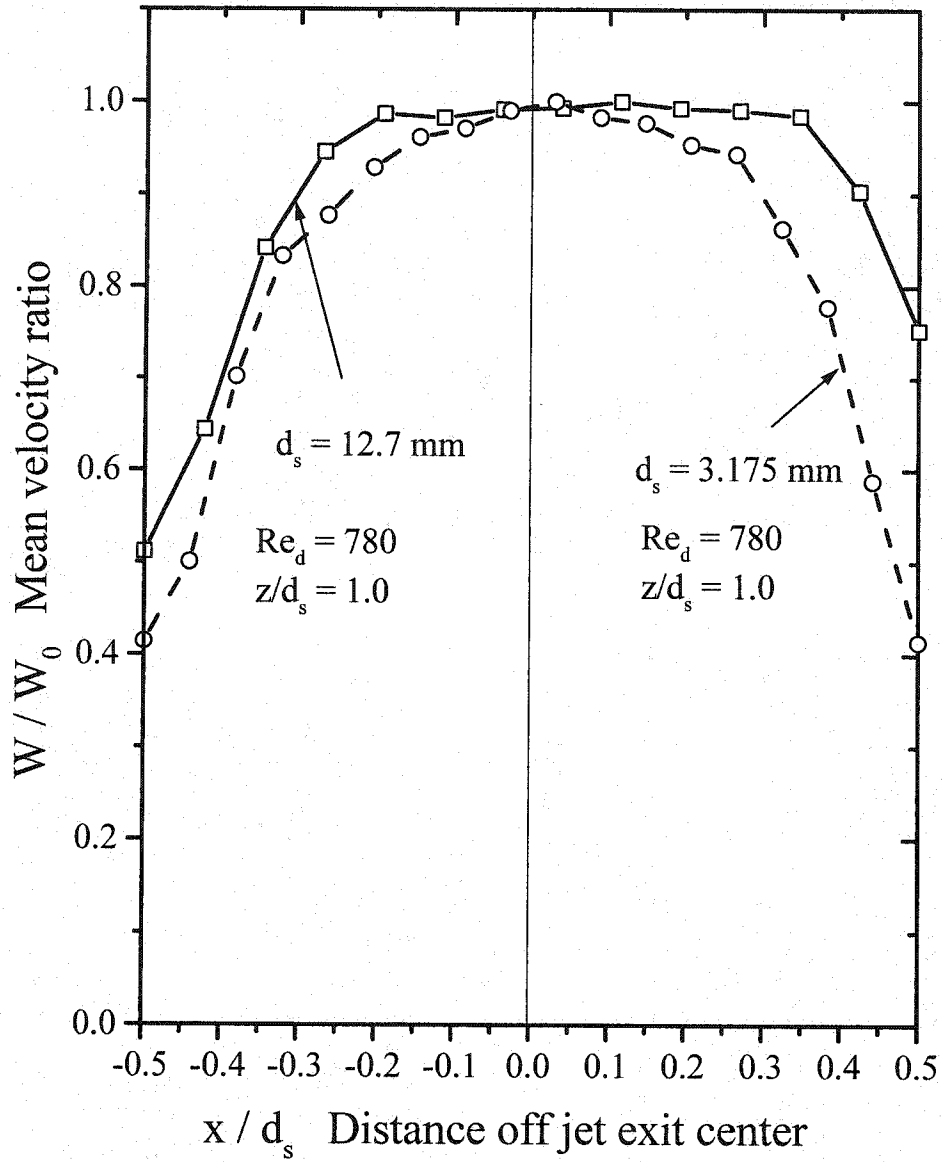


Figure 4.8 Comparison of mean velocity profiles measured at $z/d_s = 1$ with large and small source

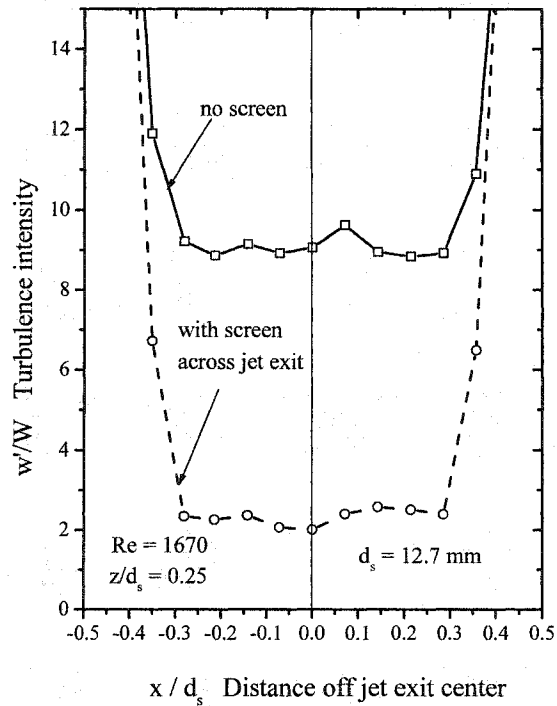
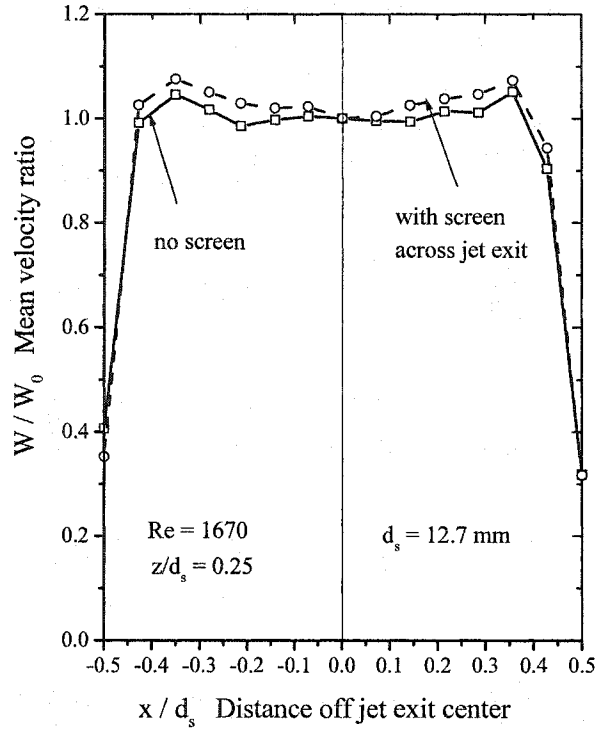


Figure 4.9 Mean velocity profiles measured with and without the exit damping screen are similar. Turbulence intensity is much lower with the screen in place.

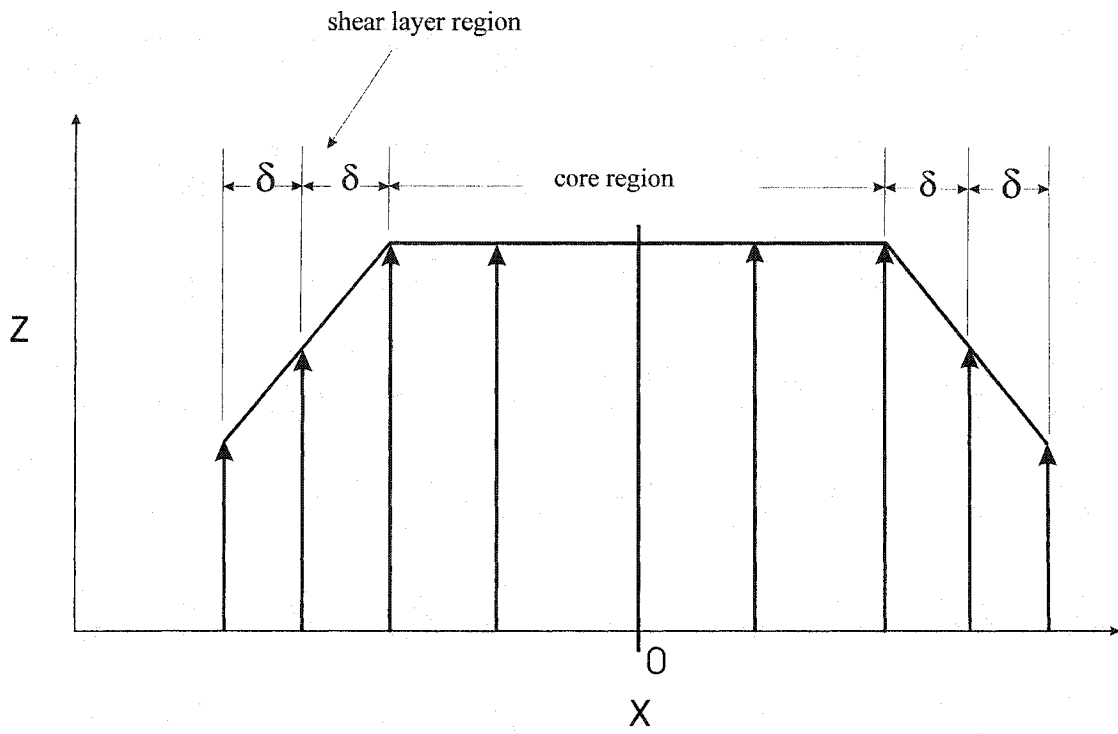


Figure 4.10 Ramp profile approximation for calculating the momentum correction factor.

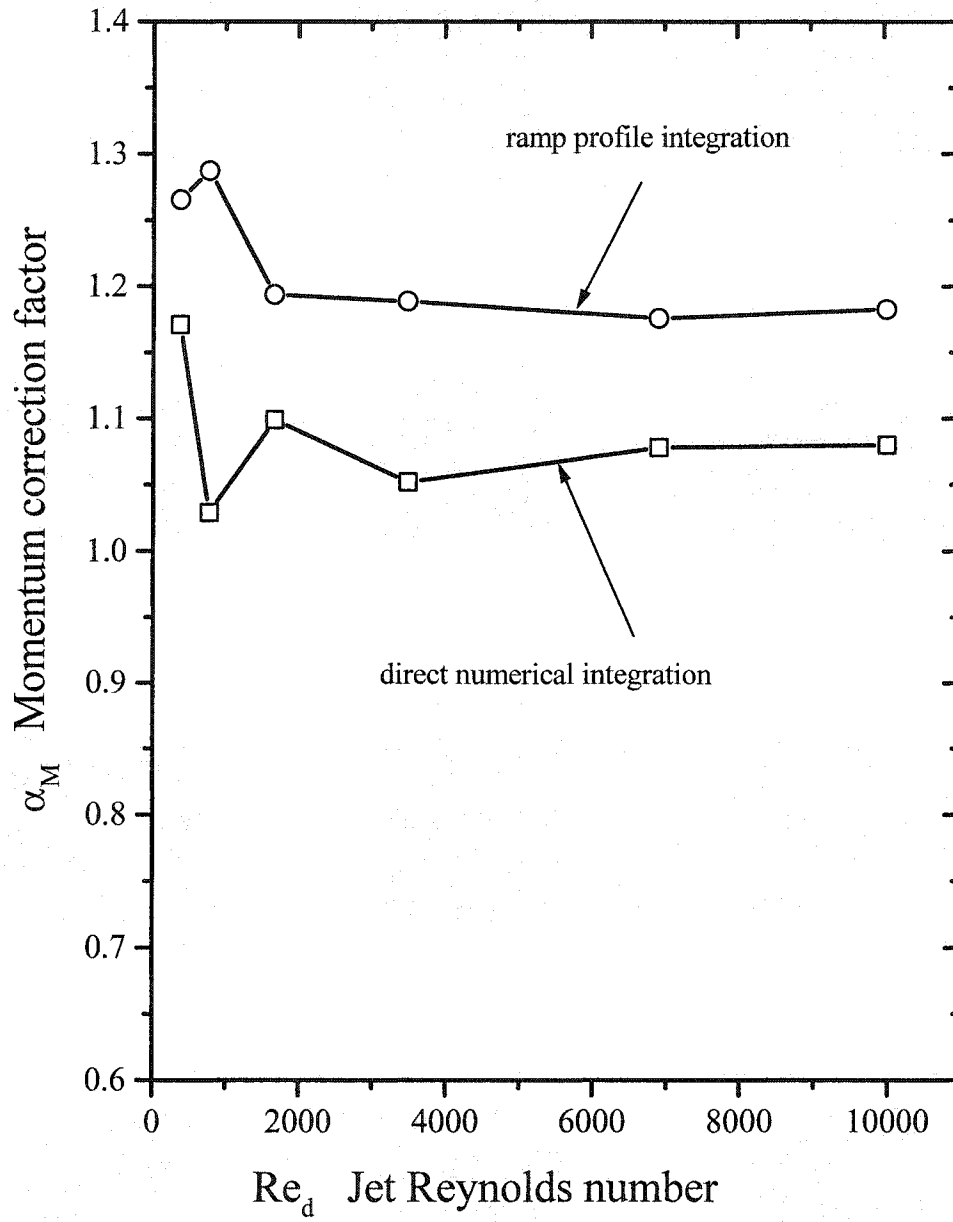


Figure 4.11 Momentum correction factor values calculated with direct numerical integration method are closer to the expected values for a turbulent top hat profile.

Table 4.1 List of LDV Experiments

	Source diameter d_s (mm)	Inlet holes diameter d_{in} (mm)	Reynolds number Re_d	z/d_s	Inlet Supply	Center body shape		
1	12.7	3.175	370	0.25	Plenum	Conical		
2	12.7	3.175	370	1	Plenum	Conical		*
3	12.7	3.175	780	0.25	Plenum	Conical		
4	12.7	3.175	780	1	Plenum	Conical		
5	12.7	3.175	1,670	0.25	Plenum	Conical		
6	12.7	3.175	1,670	1	Plenum	Conical		*
7	12.7	3.175	3,500	0.25	Plenum	Conical		
8	12.7	3.175	3,500	1	Plenum	Conical		*
9	12.7	3.175	6,920	0.25	Plenum	Conical		
10	12.7	3.175	6,920	1	Plenum	Conical		*
11	12.7	3.175	10,000	0.25	Plenum	Conical		
12	12.7	3.175	10,000	1	Plenum	Conical		*
13	3.175	0.794	150	1	Plenum	Conical		*
14	3.175	0.794	780	1	Plenum	Conical		
15	3.175	0.794	3,700	1	Plenum	Conical		*
16	3.175	0.794	6,675	1	Plenum	Conical		*
17	12.7	3.175	780	0.25	Plenum	Conical	Screen	*
18	12.7	3.175	1,670	0.25	Plenum	Conical	Screen	
19	12.7	3.175	3,500	0.25	Plenum	Conical	Screen	*
20	12.7	3.175	6,920	0.25	Plenum	Conical	Screen	*
21	12.7	3.175	10,000	0.25	Plenum	Conical	Screen	*
22	12.7	3.175	370	0.25	Tubes	Cross		*
23	12.7	3.175	780	0.25	Tubes	Cross		*
24	12.7	3.175	1,670	0.25	Tubes	Cross		

	Source diameter d_s (mm)	Inlet holes diameter d_{in} (mm)	Reynolds number Re_d	z/d_s	Inlet Supply	Center body shape		
26	12.7	3.175	375	0.25	Tubes	Conical		
27	12.7	3.175	780	0.25	Tubes	Conical		
28	12.7	3.175	1,670	0.25	Tubes	Conical		
29	12.7	3.175	3,500	0.25	Tubes	Conical		
30	12.7	3.175	6,920	0.25	Tubes	Conical		
31	12.7	3.175	10,000	0.25	Tubes	Conical		*
32	12.7	6.35	780	0.25	Tubes	Conical		
33	12.7	6.35	1,670	0.25	Tubes	Conical		
34	12.7	6.35	3,500	0.25	Tubes	Conical		
35	12.7	6.35	6,920	0.25	Tubes	Conical		
36	12.7	6.35	10,000	0.25	Tubes	Conical		
37	25.4	3.175	780	0.25	Tubes	Conical		*
38	25.4	3.175	1,670	0.25	Tubes	Conical		
39	25.4	3.175	6,920	0.25	Tubes	Conical		*

* data taken but not on thesis figures

Chapter 5

Modeling Reynolds Number Effects on Jet Source Turbulence

5.1 Introduction

A simple mathematical model has been developed to predict the turbulence intensity in the jet coming out of the turbulent source. The values obtained from this model are compared in this chapter with experimental data measured in the water channel, and to some data available in the literature. One basic idea in the study of the turbulence is that the dissipation rate of turbulence kinetic energy is independent of the fluid viscosity, ν , as long as the viscosity is sufficiently small, to make the Reynolds number sufficiently high.

5.2 A homogeneous mixing chamber model for turbulence intensity

The standard assumption of isotropy for the dissipation ε yields a value dependent on only a single spatial derivative,

$$\varepsilon_{viscous} = \frac{15}{2} \nu \overline{\left(\frac{\partial u}{\partial y}\right)^2} = 15 \nu \frac{\overline{u^2}}{\lambda_g^2} \quad (5.1)$$

The Taylor microscale of turbulence λ_g is defined by Equation 5.1.

The fundamental relationship on which many scaling arguments are based is that dissipation may be scaled by large eddy parameters to write an inviscid estimate of energy transfer rate $\varepsilon_{inertia}$ through the inertial subrange of the velocity fluctuation spectrum

$$\varepsilon_{inertia} = B_{inertia} \frac{u_s^3}{l} \quad (5.2)$$

where the turbulent velocity scale u_s for isotropic turbulence is defined as $u_s^2 = \overline{w^2}$. Now Equation 5.1 shows that the total dissipation is viscosity dependent, while Equation 5.2 shows that when dissipation is limited by the transfer rate through the inertial subrange, ε is independent of viscosity.

Wilson (private communication, 2001) developed the following equation for the dissipation inside the mixing chamber. This equation is similar to a dissipation model proposed by Norris and Reynolds (1975).

$$\varepsilon = B_{inertia} \frac{u_s^3}{l} + B_{viscous} \frac{\nu u_s^2}{l^2} \quad (5.3)$$

Equation 5.3 includes both inertial and viscous components in the dissipation equation.

The Norris and Reynolds (1975) dissipation model has been widely used in $k - \varepsilon$ turbulence closure models for CFD. For example, Lakehal et al. (2001) used Norris and Reynolds (1975) model for low Reynolds number effects in their analysis of a surface jet for film cooling of a gas turbine blade.

5.2.1 Reynolds number behavior of dissipation model

The dissipation model of Wilson (private communication, 2001), which is coincidentally similar to the dissipation model of Norris and Reynolds (1975), is independent of fluid viscosity at sufficiently high Reynolds number. Sreenivasan (1998) has collected and evaluated the relevant data and plots the graph between $\varepsilon \Lambda_f / u_s^3$ and the Taylor's microscale Reynolds number Re_{λ_g} . The dissipation data sets reviewed by Sreenivasan (1998) were compared with the values calculated from the model. To do this

some equations are transformed into the terms used by Sreenivasan (1998). Equation 5.3 can be written as

$$\frac{\epsilon l}{u_s^3} = B_{inertia} + B_{viscous} \frac{\nu}{u_s l} \quad (5.4)$$

The large eddy length scale is best defined in terms of the integral length scale of autocorrelation for u in terms of streamwise distance x . $\Lambda_f = l/1.33$ is the streamwise integral length scale of turbulence, see Hinze (1975) p. 225 & 248. Defining the Reynolds number of turbulence

$$Re_l = \frac{u_s l}{\nu} \quad (5.5)$$

Substituting Equation 5.5 into Equation 5.4

$$\frac{\epsilon l}{u_s^3} = B_{inertia} + \frac{B_{viscous}}{Re_l} \quad (5.6)$$

At high turbulence Reynolds number, Re_l , an inertial subrange exists where $\epsilon_{inertia}$ is independent of the viscosity (i.e., Re_l) at the end of the subrange the viscous dissipation $\epsilon_{viscous}$ from Equation 5.1 is equal to $\epsilon_{inertia}$ in Equation 5.2

$$\epsilon_{inertia} = \epsilon_v \quad (5.7)$$

$$\frac{B_{inertia} u_s^3}{l} = 15\nu \frac{u_s^2}{\lambda_g^2} \quad (5.8)$$

$$\frac{l}{\lambda_g} = \frac{B_{inertia}}{15} \frac{u_s \lambda_g}{\nu} \quad (5.9)$$

Transposing terms in Equation 5.8 yields an equation for the Reynolds number of large scale turbulence l ,

$$\left(\frac{u_s l}{\nu}\right)^{1/2} = \left(\frac{15}{B_{inertia}}\right)^{1/2} \left(\frac{l}{\lambda_g}\right) \quad (5.10)$$

Then, using Equation 5.9 in Equation 5.10

$$\left(\frac{u_s l}{\nu}\right)^{1/2} = \left(\frac{15}{B_{inertia}}\right)^{1/2} \left(\frac{B_{inertia}}{15}\right) \left(\frac{u_s \lambda_g}{\nu}\right) \quad (5.11)$$

$$\left(\frac{u_s l}{\nu}\right) = \left(\frac{B_{inertia}}{15}\right) \left(\frac{u_s \lambda_g}{\nu}\right)^2 \quad (5.12)$$

Substituting Equation 5.12 into Equation 5.4

$$\frac{\epsilon l}{u_s^3} = B_{inertia} + \frac{15 B_{viscous}}{B_{inertia} \left(\frac{u_s \lambda_g}{\nu}\right)^2} \quad (5.13)$$

Substituting $l=1.33 \Lambda_f$ into Equations 5.13 and simplifying yields

$$\frac{\epsilon \Lambda_f}{u_s^3} = \frac{B_{inertia}}{1.33} + \frac{11.3 B_{viscous}}{B_{inertia} Re_{\lambda_g}^2} \quad (5.14)$$

where Re_{λ_g} is the microscale Reynolds number based on u_s , the Taylor micro scale λ_g , and kinematic viscosity ν . Note that the $\epsilon_{viscous}$ depends on $Re_{\lambda_g}^{-2}$ in Equation (5.14) and to Re_d^{-1} in Equation 5.28 (see on page 78).

Figure 5.2 shows that by adjusting the two empirical constants $B_{inertia}$ and $B_{viscous}$, Equation 5.14 is in very good agreement with the experimental data reviewed by Sreenivasan (1998). As shown in Figure 5.2, at high values of Taylor microscale Reynolds number, with $Re_{\lambda_g} \geq 100$, the dissipation is almost constant and at low Reynolds number there is a sharp change in dissipation, which means dissipation is highly dependent on viscosity. In Figure 5.2, the empirical values of constants $B_{inertia}$ and

$B_{viscous}$ used in the lower line are 0.55 and 22 respectively and in the upper lines are 0.8 and 32. In both curve fits to the DNS (direct numerical simulation of Navier stokes equation) data, the value of $B_{viscous}$ was found to be 40 times larger than $B_{inertia}$.

Norris and Reynolds (1975) studied the flow near the wall at low Reynolds number and they found that the viscous "constant" $B_{viscous}$ was only a factor of two larger than the inertial constant $B_{inertia}$.

5.2.2 Applying the dissipation model to mixing chamber

In the mixing chamber model developed for the present study, it is assumed that the dissipation is dominated by shear layers in the jets coming into the mixing chamber. Therefore the inlet hole diameter d_{in} can be used as the turbulence length scale, where d_{in} is the diameter of the four holes ejecting the jets into the mixing chamber. The large eddies length scale l is written as

$$l = B_l d_{in} \quad (5.15)$$

where B_l is the length scale constant. Substituting Equation 5.15 into Equation 5.3

$$\varepsilon = B_{inertia} \frac{u_s^3}{B_l d_{in}} + B_{viscous} \frac{\nu u_s^2}{B_l^2 d_{in}^2} \quad (5.16)$$

As shown in Figure 5.1 the turbulence kinetic energy balance in the mixing chamber is

$$\left(\begin{array}{c} \text{Turbulence} \\ \text{KE flux out} \end{array} \right) - \left(\begin{array}{c} \text{Turbulence} \\ \text{KE flux in} \end{array} \right) = \left(\begin{array}{c} \text{Pr oduction inside} \\ \text{the mixing chamber} \end{array} \right) - \left(\begin{array}{c} \text{Dissipation in the} \\ \text{mixing chamber} \end{array} \right) \quad (5.17)$$

It is assumed that the four jets entering the mixing chamber carry no turbulence K.E. with them, so that the second term in Equation 5.17 is zero.

Equation 5.17 can be written as

$$3 \left(\frac{u_s^2}{2} \right) \rho Q_{out} = \rho \nabla \mathbb{P} - \rho \nabla \varepsilon \quad (5.18)$$

where ∇ is the volume of the mixing chamber. From a mean kinetic energy balance the production (\mathbb{P}) of turbulence kinetic energy, by the number N_{in} jets, entering the mixing chamber is

$$\mathbb{P} = \frac{\rho \left(Q_{in} N_{in} \frac{U_{in}^2}{2} \right)}{\rho \nabla} \quad (5.19)$$

Substituting Equations 5.16 & 5.19 into Equation 5.18 and simplifying the terms yields

$$3 \frac{u_s^2}{2} Q_{out} = Q_{in} N_{in} \frac{U_{in}^2}{2} - \nabla \left(B_{inertia} \frac{u_s^3}{B_l d_{in}} + B_{viscous} \frac{\nu u_s^2}{B_l^2 d_{in}^2} \right) \quad (5.20)$$

From a mass balance

$$Q_{in} N_{in} = Q_{out} \quad (5.21)$$

Substituting Equation 5.21 into Equation 5.20 and arranging the terms

$$3 \frac{u_s^2}{2} Q_{out} + \frac{B_{inertia}}{B_l} \frac{u_s^3 \nabla}{d_{in}} + \frac{B_{viscous}}{B_l^2} \frac{\nu u_s^2 \nabla}{d_{in}^2} = Q_{out} \frac{U_{in}^2}{2} \quad (5.22)$$

from Equation 5.21

$$U_{in} = \frac{1}{N_{in}} \left(\frac{d_s}{d_{in}} \right)^2 \quad (5.23)$$

The jet Reynolds number based on the jet nozzle diameter is

$$Re_d = \frac{U_s d_s}{\nu} \quad (5.24)$$

For the present study the mean velocity scale is taken to be the velocity from the surface jet exit so, $U_s = W_s$. From Equation 5.24, viscosity ν can be expressed as

$$v = \frac{U_s d_s}{\text{Re}_d} \quad (5.25)$$

Substituting Equations 5.23 & 5.25 into Equation 5.22 and simplifying the terms yields

$$u_s^2 \left(\frac{3Q_{out}}{2} + \left(\frac{B_{inertia}}{B_l} \frac{u_s \nabla}{d_{in}} \right) + \left(\frac{B_{viscous}}{B_l^2} \left(\frac{U_s d_s}{\text{Re}_d} \right) \frac{\nabla}{d_{in}^2} \right) \right) = Q_{out} \frac{1}{N_{in}^2} \left(\frac{d_s}{d_{in}} \right)^4 \frac{U_s^2}{2} \quad (5.26)$$

divide by $U_s^2 Q_{out}$ on both sides of Equation 5.26

$$\frac{u_s^2}{U_s^2} \left(\frac{3}{2} + \left(\frac{B_{inertia}}{B_l} \frac{u_s \nabla}{Q_{out} d_{in}} \right) + \left(\frac{B_{viscous}}{B_l^2} \left(\frac{U_s d_s}{\text{Re}_d} \right) \frac{\nabla}{Q_{out} d_{in}^2} \right) \right) = \frac{1}{2N_{in}^2} \left(\frac{d_s}{d_{in}} \right)^4 \quad (5.27)$$

Substituting $Q_{out} = A_s U_s$ into Equation 5.27, where A_s is the area of the jet nozzle and U_s is the velocity of the jet coming out of the jet nozzle.

$$\frac{u_s^2}{U_s^2} = \frac{\frac{1}{N_{in}^2} \left(\frac{d_s}{d_{in}} \right)^4}{3 + \left(\frac{2B_{inertia}}{B_l} \frac{\nabla}{A_s d_{in}} \right) \frac{u_s}{U_s} + \left(\frac{2B_{viscous}}{B_l^2} \frac{d_s \nabla}{A_s d_{in}^2} \right) \frac{1}{\text{Re}_d}} \quad (5.28)$$

From Equation 5.28 turbulence intensity can be calculated, $B_{inertia}$, $B_{viscous}$ and B_l are adjustable empirical constants. The values of $B_{inertia} = 0.8$ was set from widely used representations of the internal subrange. The remaining two constants, $B_{viscous}$ & B_l , were calculated by fitting the predicted turbulence intensity curve to the experimental data. Figure 5.3 shows the comparison between the predicted turbulence intensity from Equation 5.28 and the measured values of the turbulence intensity. As shown in Figure 5.3, the mathematical model (with two empirical constants) agreed very well with experimental measurements. The empirical values of the constants are $B_{inertia} = 0.8$, $B_{viscous} = 5.0$ and $B_l = 0.1$ respectively. In the mixing chamber dissipation model in

Equation 5.3, the viscous constant is about 6 times the value of the inertial constant, well within the range from 2.0 to 40 for the ratio $B_{viscous}/B_{inertia}$ found elsewhere in the literature.

In Figure 5.3, there is a good agreement between the predicted values of turbulence intensity using Equation 5.28 and the experimental data when $d_{in}=3.175$ mm. Equation 5.28 predicts 25% less turbulence intensity when $d_{in} = 6.35$ mm. When a 20% lower value of d_{in} was used in Equation 5.28 (dotted line in Figure 5.3), there was good agreement between the predicted and experimental values of turbulence intensity. As shown in Figure 5.4, for the sharp-edged large inlet holes with $d_{in} = 6.35$ mm the length of these holes into the mixing chamber was only 1.0 hole diameter. Certainly, this distance was not enough for the flow to mix inside the holes, and eventually the effective diameter d_{eff} was less than the actual size of the inlet holes. On the other hand in case of the sharp-edged small holes with $d_{in} = 3.175$ mm, the length was 2.0 hole diameters. This was probably enough to mix the fluid inside the holes and could produce a uniform exit profile. For these small holes, the effective diameter would probably still be smaller than the inlet diameter, but it was assumed for simplicity that $d_{eff} = d_{in}$ (that is $C_c = 1.00$) for the small holes. The coefficient of area contraction was calculated as $C_c = 0.64$ for the large holes and $C_c = 1.00$ for the small holes.

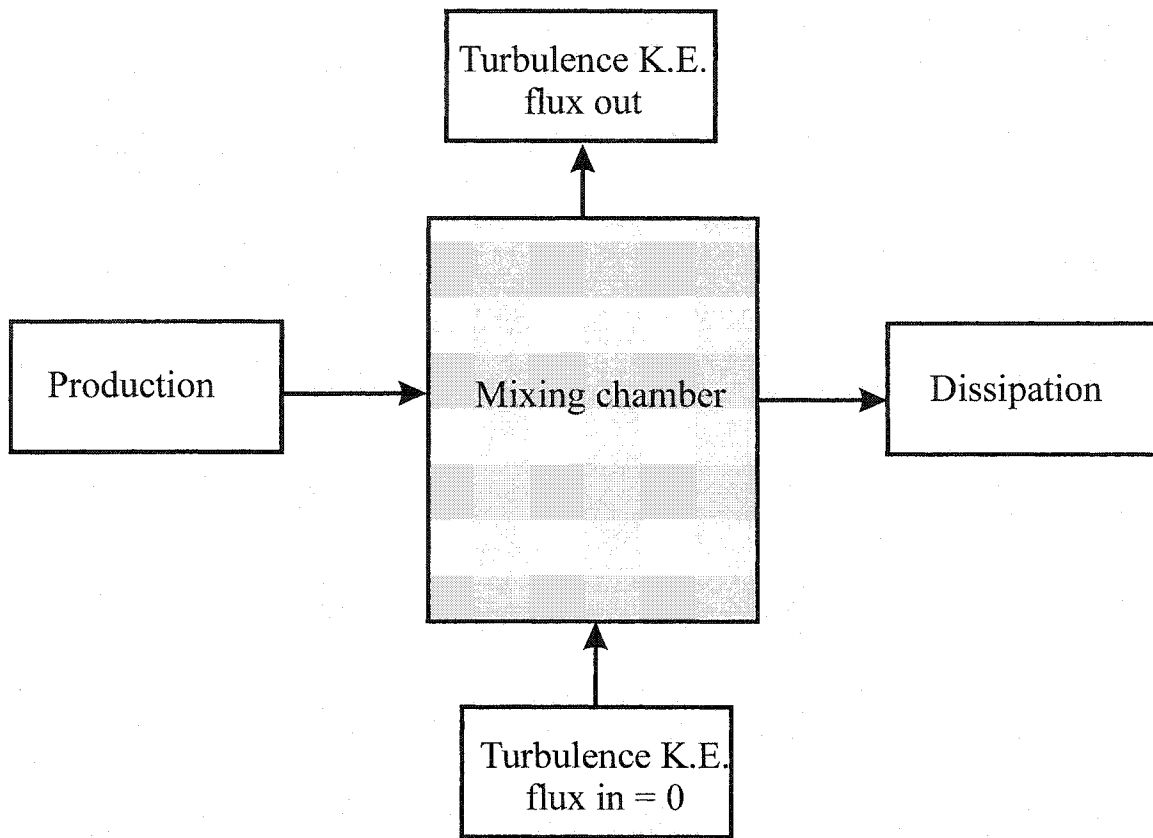


Figure 5.1 Turbulence kinetic energy and mass balance flow diagram for the mixing chamber upstream of the surface jet nozzle.

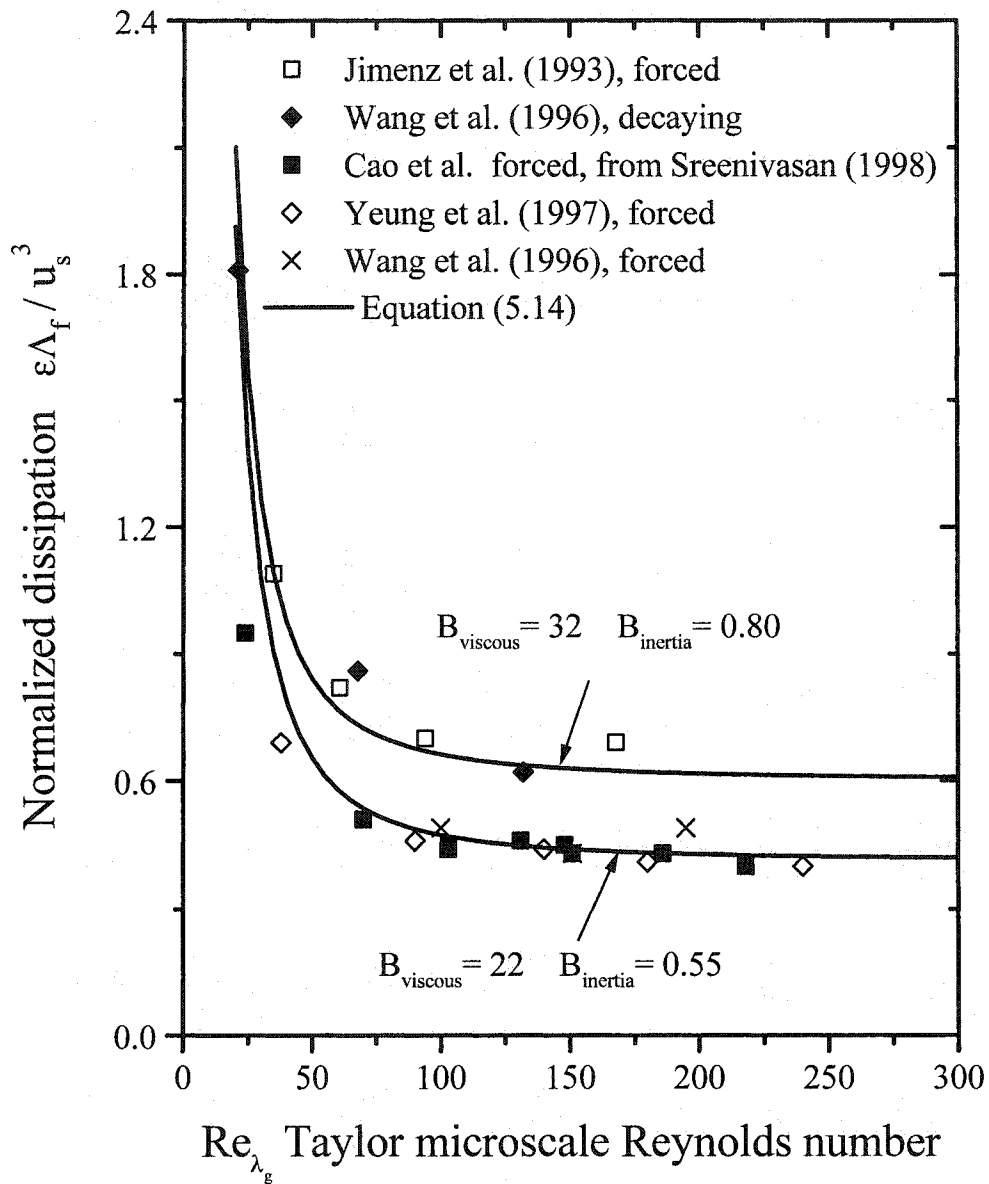


Figure 5.2 Dependence of dissipation on the viscosity for this model compared to the DNS (direct numerical simulation) studies of forced (boundary layer) and decaying (grid) turbulent flows reviewed by Sreenivasan (1998).

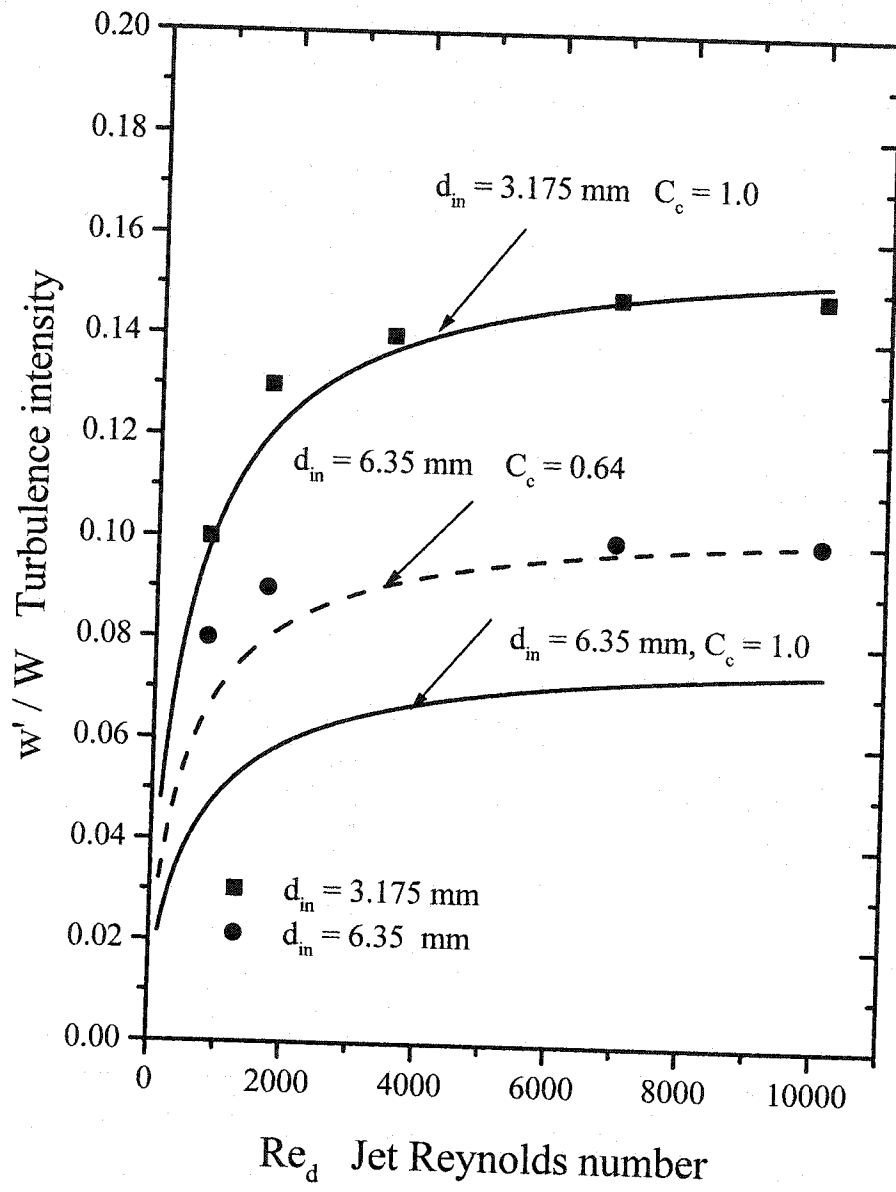


Figure 5.3 Turbulence intensity variation with Jet Reynolds number using Equation 5.28 with $B_{inertia} = 0.80$, $B_{viscous} = 5.0$ and $B_1 = 0.10$; and experimental data for two sizes of inlet jet holes, and varying jet contraction coefficient for the large holes.

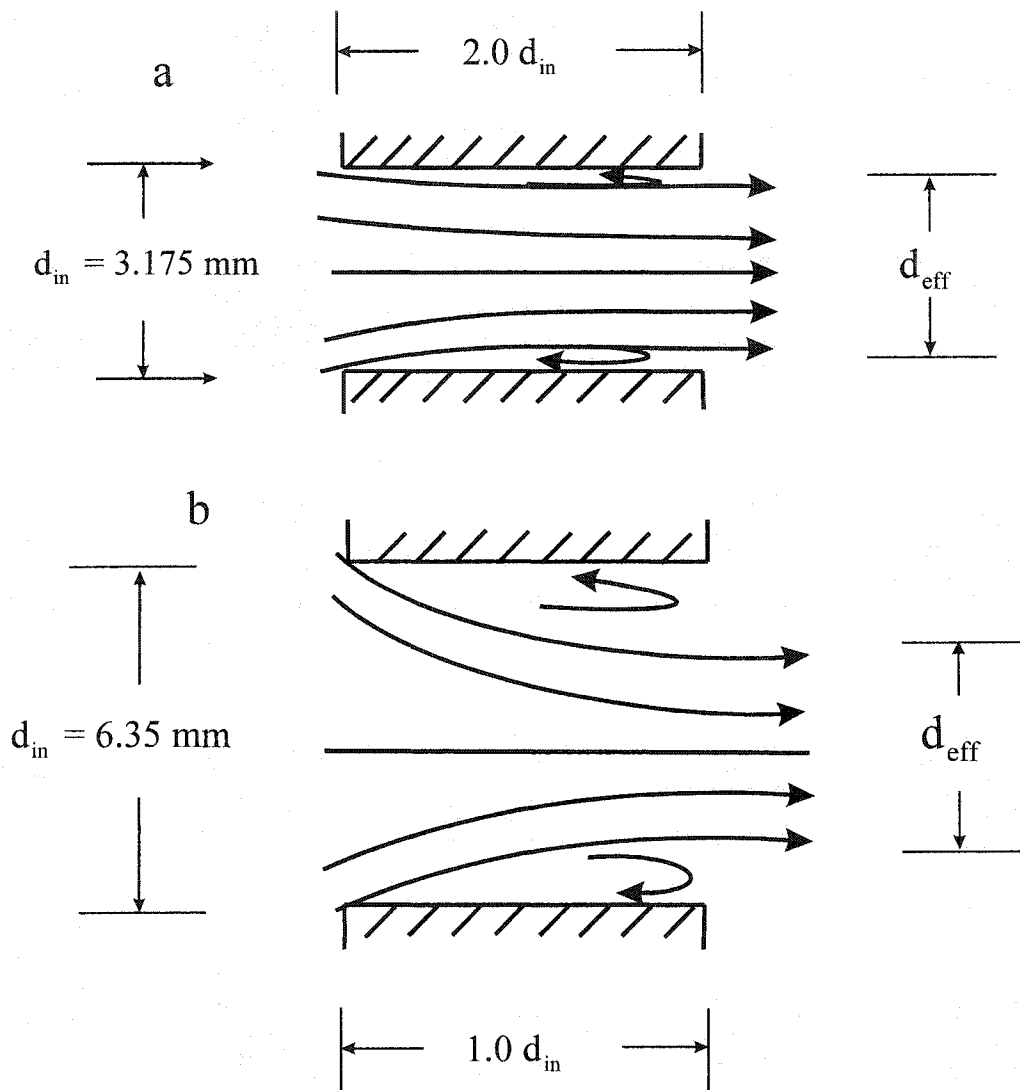


Figure 5.4 Enlarged view of the inlet holes with assumed flow separation at the exit of the large diameter holes producing an area contraction coefficient $C_c = 0.8^2 = 0.64$. a) Small inlet holes, b) Large inlet holes.

Chapter 6

Comparison of plume rise model to the data

6.1 Introduction

The trajectories of a turbulent jet in cross flow have been studied by numerous investigators, for example Keffer and Baines(1963), Pratte and Baines (1967), Hoehne and Luce (1970), Kamotani and Greber (1972) and Johnston and Wilson (1997). They have shown that the main parameter influencing the trajectory is the velocity ratio between the jet and the crossflow. In this study, velocity ratio and Reynolds number effects on the plume trajectory were investigated.

The centerline trajectory of the plume was determined from the average intensity of 1800 images of the jet. These images were recorded at the rate of 6 images per second for 300 seconds. A video camera was used to acquire those images. The trajectory measured from the image of average intensity was found to agree with the image of average concentration calculated by converting the intensity image into the concentration. Johnston and Wilson (1997) and Smith and Mungal (1997) used this technique to determine the plume trajectory.

Table 6.1 shows all the experiments taken to determine the plume trajectory.

6.2 Interrelation effects from Reynolds number, downwash, velocity ratio and entrainment coefficient on plume rise

Jet exit Reynolds number Re_d , downwash, jet to crossflow velocity ratio and air entrainment coefficient have interrelated effects on plume rise. These interrelated effects

are discussed in the following sections. The values of these interdependent parameters in this chapter are the last (successful) iteration in this trial and error process.

6.3 Validation of measurement techniques

Effects of Reynolds number, velocity ratio and downwash can be small and will be detectable only if experiments have a very small repeatability error. Repeatability of data for a surface jet is shown in Figures 6.1 & 6.2 and there is roughly 1-5% difference in plume rise between these two data sets. There was an interval of 100 operational hours of testing between the two data sets. The good agreement between these two data sets confirms the precision of the measurement techniques. Figure 6.3 shows the comparison between this data and the measurements of Johnston and Wilson (1997) for a stack plume using the same water channel facility, with a stack exit Reynolds number of 1800. Only the data with Reynolds number close to 1800 are compared to their experiments. Although the techniques used in both studies were entirely different there is very good agreement between these two data sets.

6.4 Effects of varying entrainment coefficient to predict plume trajectories.

The choice of entrainment coefficient for a plume has large effects on predicting its trajectory. The trajectory-averaged entrainment coefficient β is discussed in section 2.2. Some investigators, such as Hoult and Weil (1972) and Weil (1988) suggest that the entrainment coefficient should be a constant, $\beta=0.6$, while others Briggs (1975), suggest that β should have some dependence on the jet to crossflow velocity ratio M . Fay, Escudier and Hoult (1970) found a dependence on the velocity ratio up to $M = 1.2$,

after which they suggested β was constant. Johnston and Wilson (1997) found a strong dependence of β on the velocity ratio M . They suggested that $\beta = 0.80$ at $M = 0$, and $\beta = 0.30$ at $M \rightarrow \infty$.

In this study, the entrainment coefficient was varied as a function of the velocity ratio, M , and Reynolds number, Re_d . The reason for varying β with the velocity ratio is that as M increases, more of the rise of the plume is near vertical and β will be smaller. The entrainment coefficient β should eventually be $\beta \sim 0.1$ for $M \rightarrow \infty$, where the high velocity exit jet behaves like a jet into stagnant fluid ($M \rightarrow \infty$ as $W_s \gg U_s$). Therefore introducing a dependence on M is a simple way of varying the entrainment coefficient β . The reason for varying β with the Reynolds number is that as the Reynolds number increases, the jet becomes more turbulent and entrains more ambient fluid, which increases the entrainment coefficient β .

Figures 6.4, 6.5 & 6.6 show the comparison between the experimental data and the momentum rise equation (Equation 2.21) with no surface pressure downwash correction. The entrainment coefficient values used to match the data are much larger than the values for equivalent stack plumes. The value of β found in the stack plume studies were between 0.4 to 1.0. From this, it is concluded that the predictions of the momentum rise of a surface jet require some downwash correction due to low pressure on the downstream surface from the jet exit hole. As shown in Figure 6.4 the predicted value of β was too large in the case of $M=1$ but at higher value of M such as $M=16$ the predicted values of β were reasonable. This makes sense, because at high jet to crossflow velocity ratios the jet escapes from the low pressure region near the wall and

the downwash effects are almost negligible, for details of the downwash model see Chapter 2, Section 2.5.

6.5 Downwash velocity correction

A downwash velocity correction model was developed in Chapter 2 to be used in the plume rise equation. See Section 2.5 for details. Equation 2.50 gives the correction to plume rise as

$$\Delta h_{downwash} = B_3 x^{1-n} \quad (6.1)$$

From Chapter 2, the non-dimensional plume rise equation for a fully bent over non-buoyant momentum jet, accounting for jet wake pressure-induced downwash is

$$\frac{h}{d_s} = \left(\frac{3}{4\beta^2} M^2 \frac{x}{d_s} \right)^{1/3} - B_3 \left(\frac{x}{d_s} \right)^{1-n} \quad (6.2)$$

The values for the downwash coefficient, B_3 , and wake decay exponent, n , were determined experimentally. These two values are interrelated and the best pair of B_3 , and n was obtained by curve fitting the experimental data. Figures 6.7 to 6.9 show some of these values obtained by curve fitting the data to Equation 6.2. As discussed in section 2.5 the downwash effects are the most pronounced at low jet to crosswind velocity ratio, so the $M = 1$ case is shown here. In Figures 6.7 & 6.8 the same value of $B_3 = 0.20$ was found for two different values of $n = 1/3$ and $n = 1/2$. In Figure 6.9 the best fit was $B_3 = 0.10$ when $n = 2/3$. As shown in Figures 6.7, 6.8 and 6.9, when $n = 1/2$ minimum values for the best fit entrainment coefficients were obtained. From this range of $1/3 < n < 2/3$, a wake decay exponent of $n = 1/2$ was selected as the most physically

realistic. This is the same value as the theoretical exponent for decay of velocity deficit in two dimensional wake.

In the current model, it is assumed that the jet emerging from the ground level source is the flow "obstacle" that causes the low-pressure area zone. It is then reasonable to assume that the downwash coefficient B_3 would be a function of the velocity ratio.

The function for B_3 was determined experimentally. The empirical function chosen for B_3 is

$$B_3 = 0.5(1 - e^{-0.5M}) \quad (6.3)$$

As shown in Figure 6.10, from velocity ratios of $M=1$ to $M=4$, B_3 for the surface jet has a sharp rise varying from 0 to 0.43, but above a velocity ratio of $M \geq 8$ it stays

around 0.5. The model for stack jets used in Johnston and Wilson (1997) shows an entirely different trend. Their model shows a sharp decrease in B_3 with increasing M .

As discussed earlier, the values of B_3, n and β are interrelated, and Equation 6.3 was obtained by using $n=1/2$ to provide the minimum value of entrainment coefficient β .

The downwash coefficient B_3 depends on the entrainment coefficient values, β , and B_3 was adjusted to get realistic β values.

6.6 Effects of entrainment coefficient on predicting plume trajectories with downwash correction

As discussed in the previous section the appropriate values of B_3 and n were determined and then these values are used in Equation 6.2 to determine the predicted values of plume trajectory with downwash correction. Figures 6.8, 6.11 & 6.12 show the

comparison of the predicted plume trajectories and the experimental data of the large source at different velocity ratios. Figures 6.13 & 6.14 show a comparison between small source data and the predicted plume rise trajectories. The β values are very realistic, compared to the values of β calculated without any downwash correction. The predicted trajectories in Figures 6.12 & 6.14 are in better agreement with the experimental data as compared to Figures 6.5 & 6.6. In order to show the Reynolds number effects on the plume trajectory independent of velocity ratio, β was normalized by the high Reynolds number entrainment coefficient β_∞ at the largest measured Re_d for that M . (The "infinity" is an optimistic symbol, and in one case it was at $Re_d=1700$!).

6.6.1 Reynolds number effects on entrainment coefficient

As shown in Figures 6.15 the normalized entrainment coefficient β/β_∞ varies with Reynolds number. A function was obtained by an empirical fit in the data

$$\frac{\beta}{\beta_\infty} = \frac{1}{1 + \frac{150}{Re_d}} \quad (6.4)$$

A slightly better fit was possible by changing the Reynolds number exponent but here the objective was to show the trend. Figure 6.15 shows that from Reynolds number 200 to 4000 there is about a 40% increase in the entrainment coefficient, whereas from Reynolds number 4000 to 10000 the increase in entrainment coefficient is only 2%. Therefore it is obvious that at the higher Reynolds number range, Reynolds number effects are negligible on the plume trajectory and at lower Reynolds numbers entrainment coefficient is a strong function of Re_d .

6.6.2 Reynolds number Effects on Plume Rise

Figure 6.16 show the increase in plume height with the increase in velocity ratio. From Equation 6.2, a new function h_{\max}/d_s can be calculated by substituting the maximum measured value $x/d_s = 20$ and using the highest Reynolds number with $\beta = \beta_{\infty}$

$$\frac{h_{\max}}{d_s} = \left(\frac{15}{\beta^2} M^2 \right)^{1/3} - 4.5 B_3 \quad (6.5)$$

Figure 6.16 shows the comparison between the measured and predicted values of plume rise (h_{\max}/d_s) calculated from Equation 6.5, with the maximum experimental Reynolds number shown beside the data point.

Figure 6.17 shows the effect of Reynolds number on plume rise. The plume rise h is normalized by h_{\max} . From the plume rise Equation 6.2.

$$\frac{h}{h_{\max}} \propto \frac{1}{\left(\frac{\beta}{\beta_{\infty}} \right)^{2/3}} \quad (6.6)$$

Substituting Equation 6.4 into Equation 6.6

$$\frac{h}{h_{\max}} = \left(1 + \frac{150}{Re_d} \right)^{2/3} \quad (6.7)$$

The Equation 6.7 is a derived equation, and not a direct empirical equation. Figure 6.17 shows that the curve obtained from the Equation 6.7 is in good agreement with the experimental data. From Reynolds number 200 to 4000, the decrease is 50% but from $Re_d = 4000$ to $Re_d = 10,000$ the decrease is about 5%. It is concluded from these results that for $Re_d > 4000$, the change in plume rise is negligible with changing Reynolds number at a fixed velocity ratio M .

6.6.3 Jet exit to crosswind velocity ratio effects on entrainment coefficient

To determine the entrainment coefficient dependence on the velocity ratio, β values were varied so the theoretical predictions for $M = 1$ to 16 would match the experimental data. A function was fit to those values of entrainment coefficients.

Figure 6.18 is a plot showing the entrainment data and the function used to predict β_{∞} .

$$\beta_{\infty} = 1.1 \left(\frac{1 + 0.063 M^2}{1 + 0.14 M^2} \right) \quad (6.8)$$

This function was found by an empirical fit. From Equation 6.8, $\beta_{\infty} = 1.1$ at $M = 0$ and $\beta_{\infty} = 0.51$ at $M \geq 16$. The empirical function used by Johnston and Wilson (1997), in their study of stack jets, is also shown in Figure 6.7. The difference for their stack jet and the surface jet in the present study was probably due to that fact that the Johnston and Wilson (1997) data was only for $Re_d = 1800$, whereas in the present study, data were collected for a wide range of Reynolds numbers. The dotted curve in Figure 6.18 is from Briggs (1984) for stack jets, added as an afterthought in editing the thesis. Briggs' curve comparison was done only after all functions were determined, and no adjustments were made to fit the present study β_{∞} to Briggs' (1984) equation. We were relieved to find that the curve from the Briggs' (1984) equation is actually a slightly better fit to the data than the empirical equation obtained in the present study.

6.6.4 Effects of initial turbulence on the plume trajectory

As discussed in Chapter 4, considerable time and effort were devoted to building a turbulent jet source. The question is, "How important are the effects of the initial jet turbulence on the plume trajectory?" As shown in Figure 4.9 the initial jet turbulence can

be reduced using a fine mesh exit screen without changing the jet velocity profile shape. Data were collected at different velocity ratios and various jet Reynolds numbers. Figures 6.19, 6.20 & 6.21 show the comparison of the jet trajectories with and without the exit screen. The jet produced from the source with no screen had about 10-15 % turbulence intensity, whereas the jet produced with the screen on the source had about 2-3% turbulence intensity. As expected, the jets with higher initial turbulence intensity have less plume rise, probably because they entrain more ambient fluid than jets with an exit screen that have low turbulence intensity. The difference between the two trajectories is roughly $\Delta h = 0.50 d_s$, except at $M = 2$ where they are almost the same, as shown in Figure 6.20. The conclusion that may be from this is that if the source used in the scale model is laminar (low turbulence), the extra rise is only $\Delta h = 0.50 d_s$.

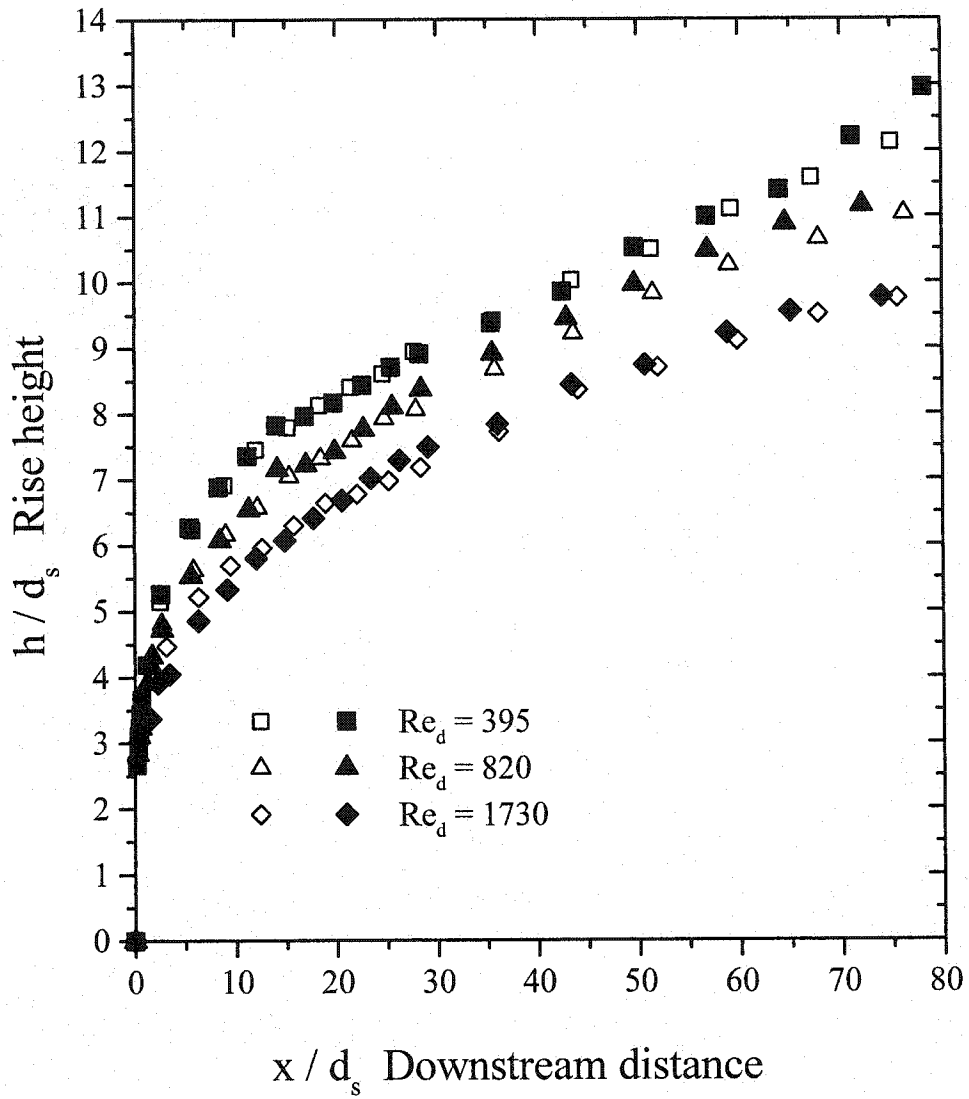


Figure 6. 1 Repeatability of data measured at velocity ratio, $M = 4$, with a 30 day interval between experiments with open and closed symbols.

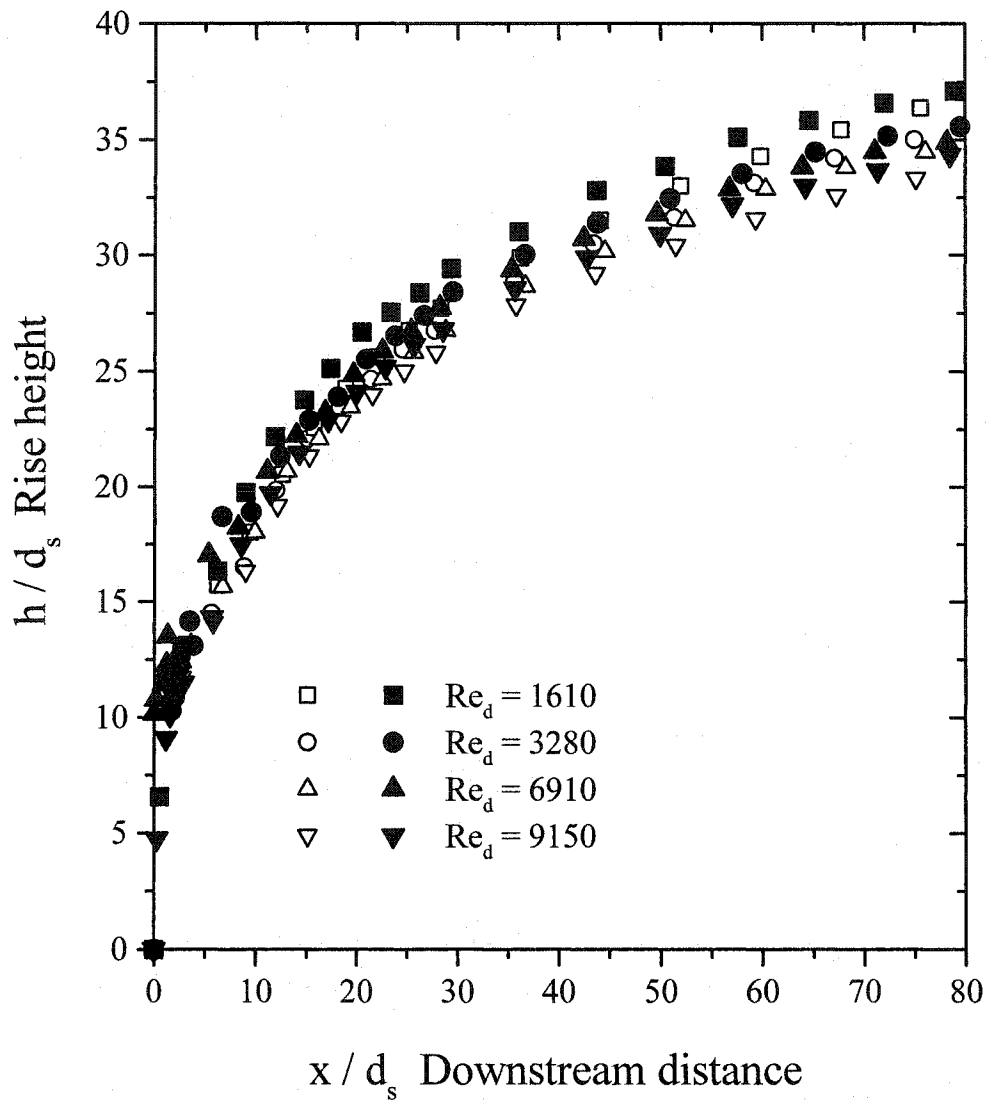


Figure 6.2 Repeatability of data measured at velocity ratio, $M=16$, with a 30 day interval between experiments with open and closed symbols.

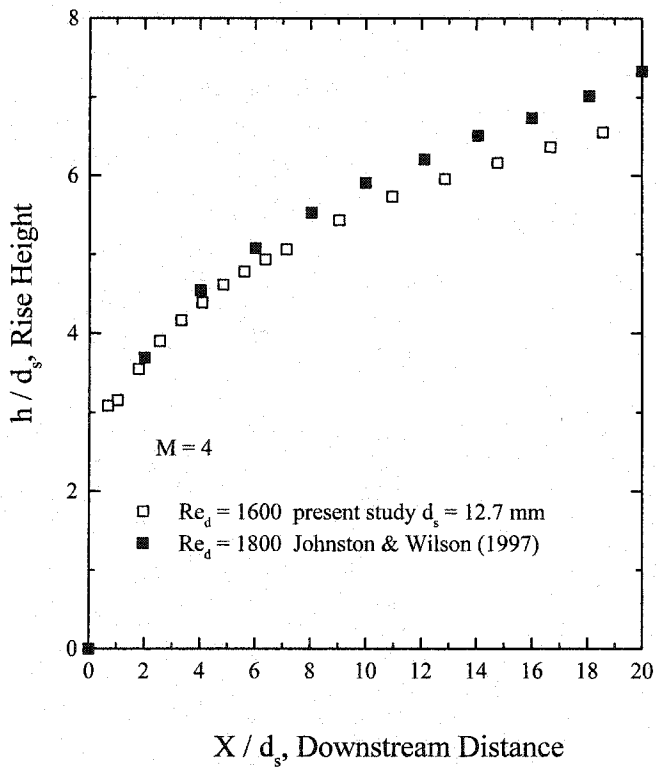
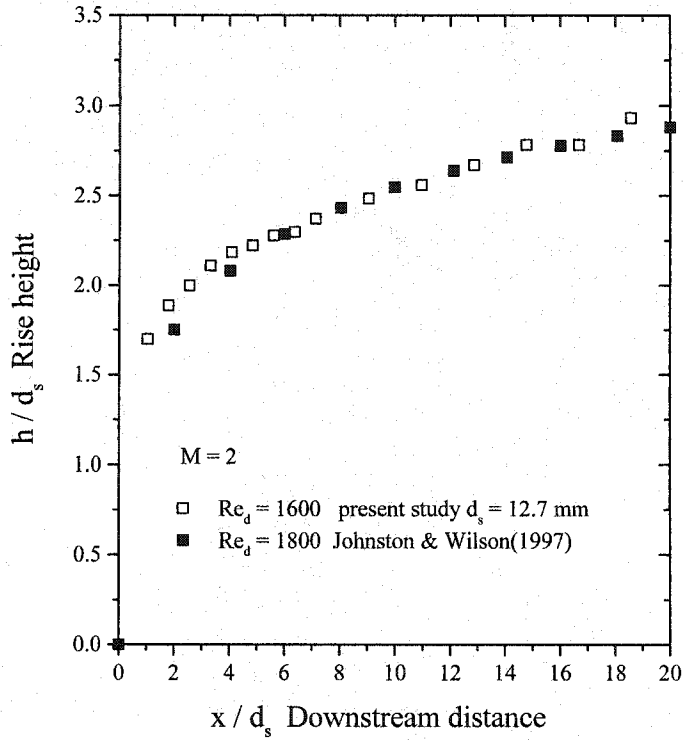


Figure 6. 3 Large source comparison between the present study data on a surface jet and measurements of Johnston and Wilson (1997) for a stack plume.

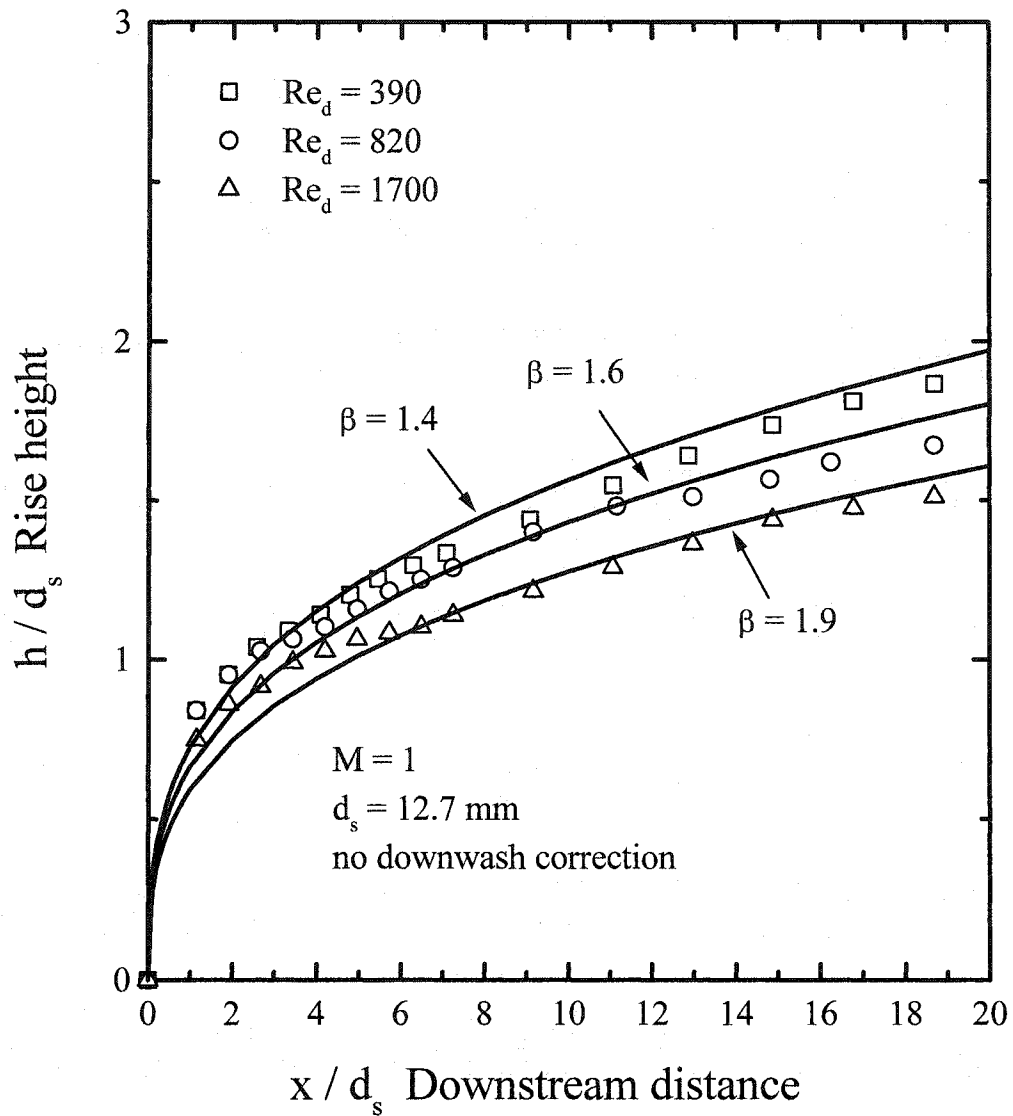


Figure 6.4 Large source comparison between experimental data and the momentum rise equation (Equation 2.21) with no downwash correction. β values are much too large if no downwash correction is used.

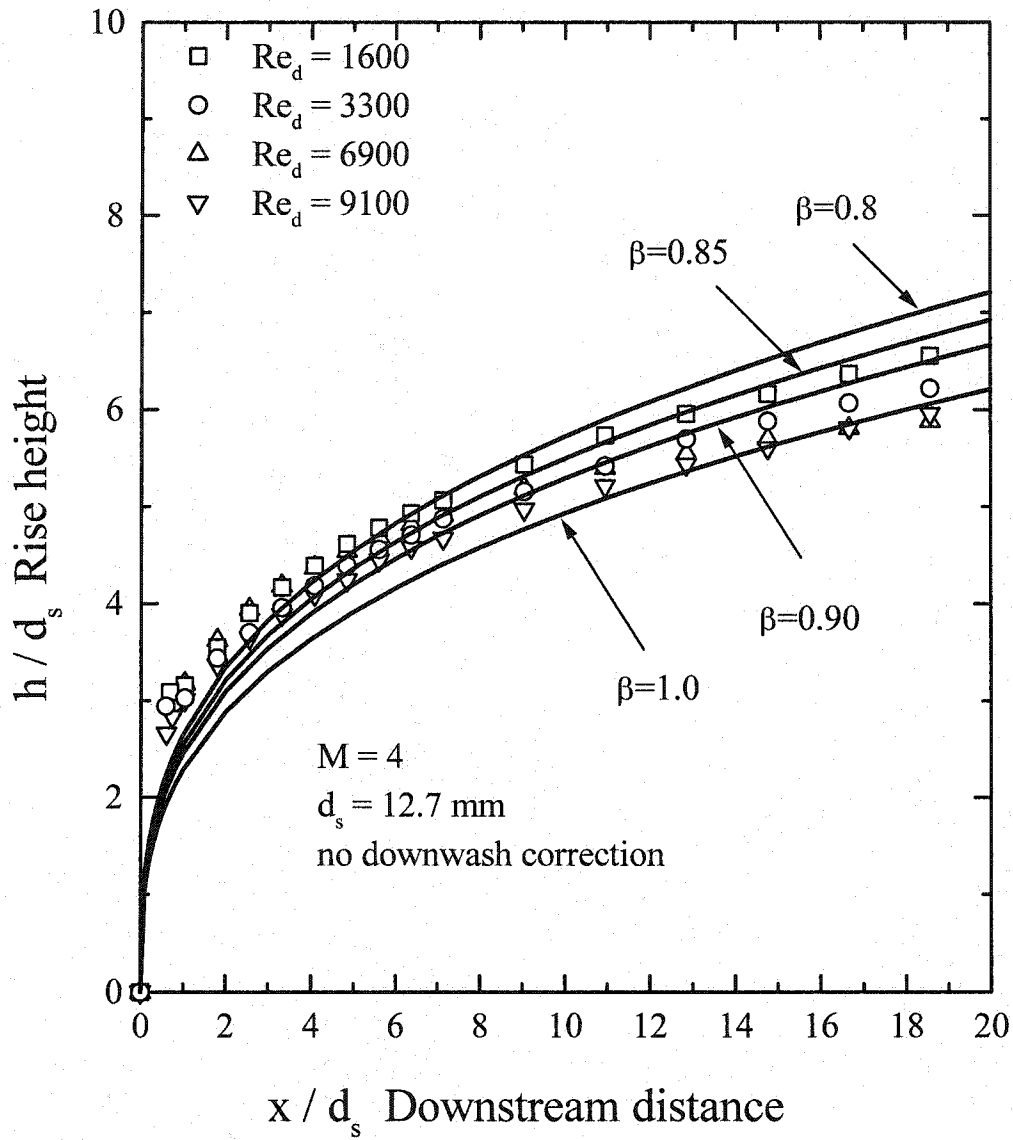


Figure 6.5 Large source comparison between experimental data and the momentum rise equation (Equation 2.21) with no downwash correction. β values are much large if no downwash correction is used.

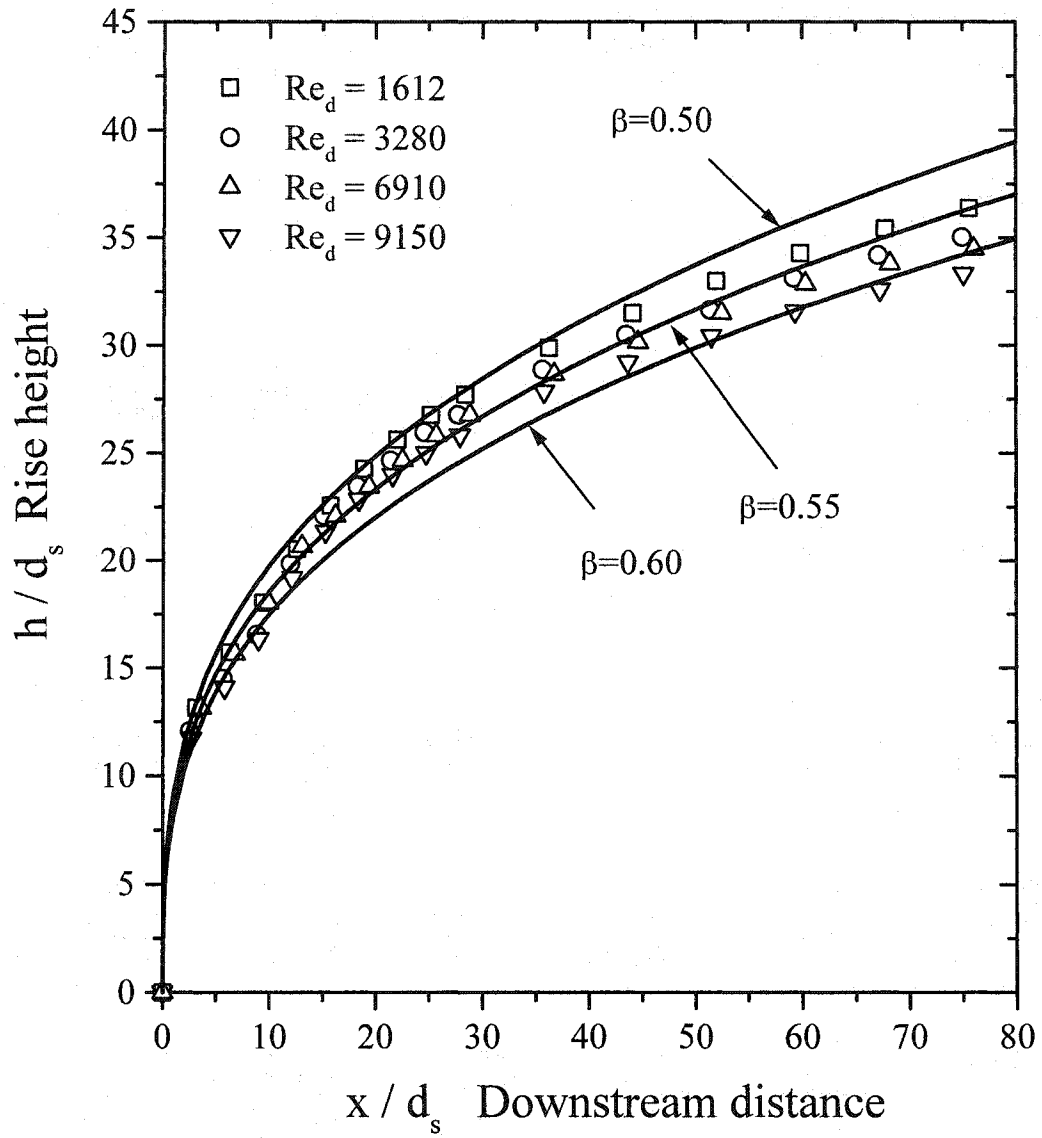


Figure 6.6 Small source comparison between experimental data and the plume rise equation (Equation 2.21) with no downwash correction. β values appear reasonable although no downwash correction is used.

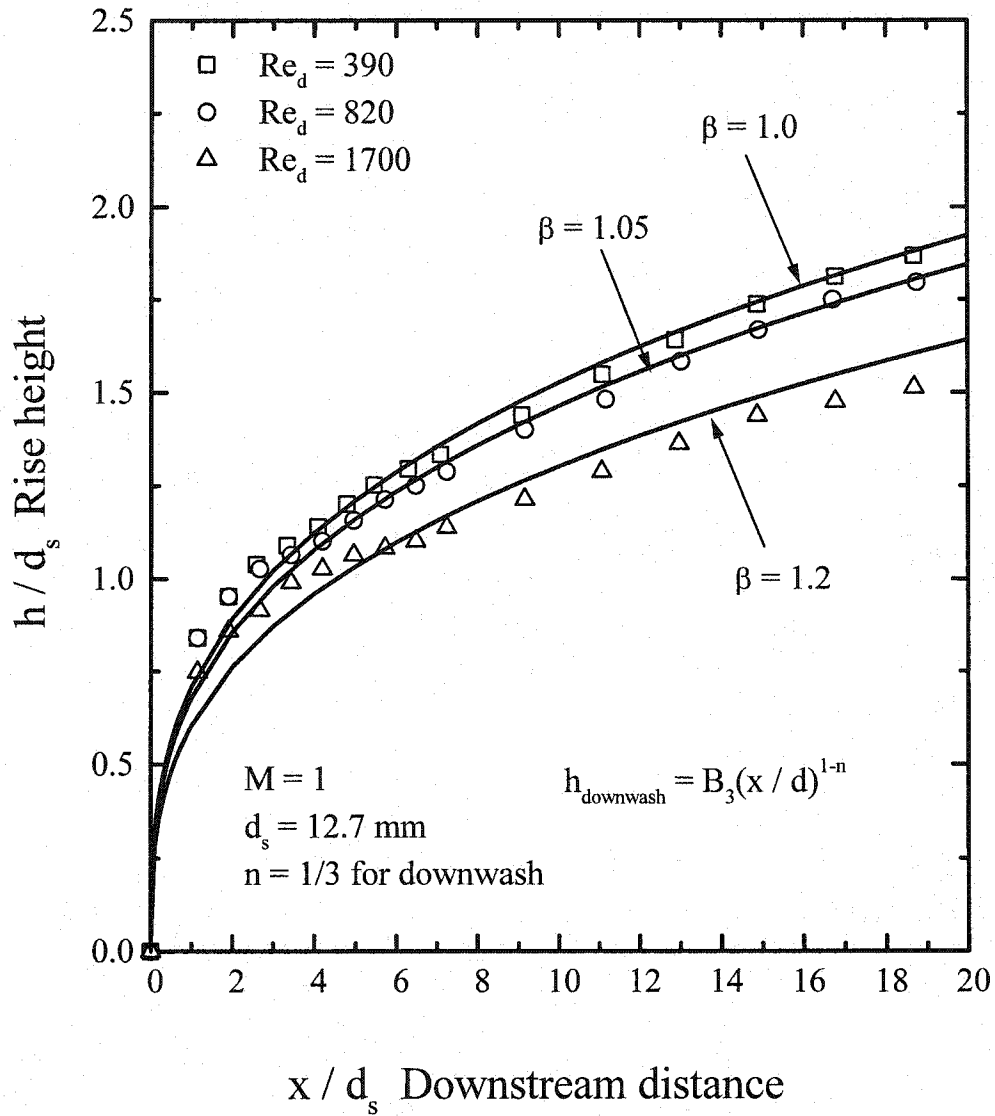


Figure 6.7 Comparison between experimental data and the plume rise equation with downwash correction (Equation 6.2). Wake decay exponent $n = 1/3$, $B_3 = 0.20$ at $M = 1$.

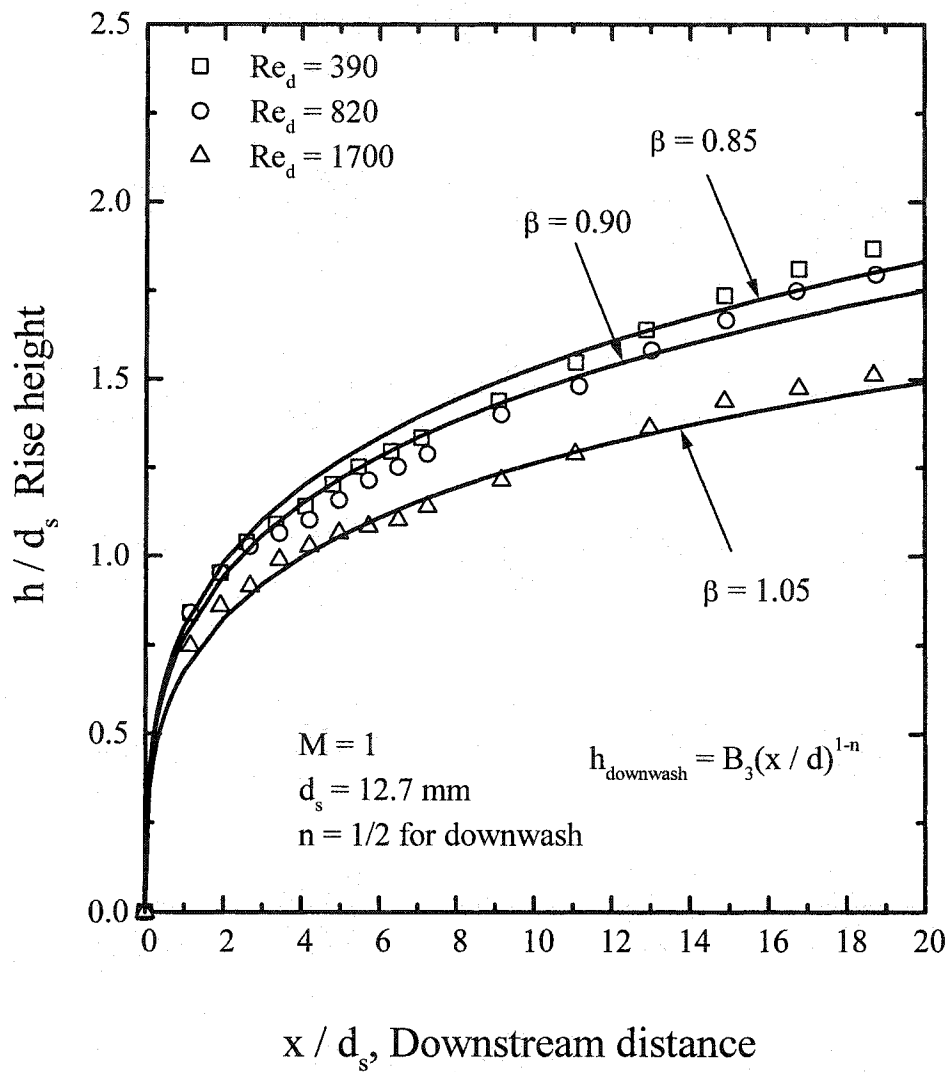


Figure 6.8 Comparison between experimental data and the plume rise equation with downwash correction (Equation 6.2). Wake decay exponent $n = 1/2$, $B_3 = 0.20$ at $M = 1$.

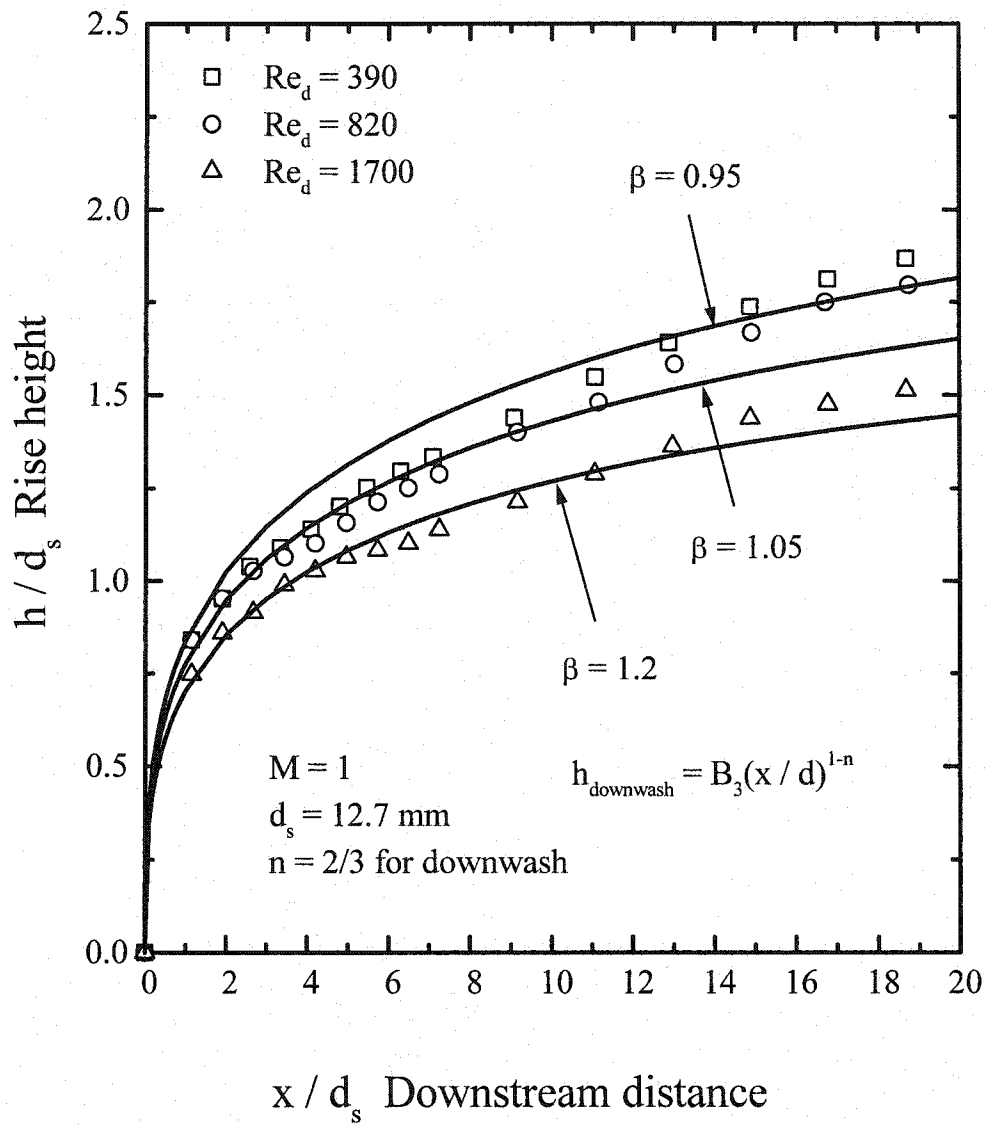


Figure 6.9 Comparison between experimental data and the plume rise equation with downwash correction (Equation 6.2). Wake decay exponent $n = 2/3$, $B_3 = 0.10$ at $M = 1$.

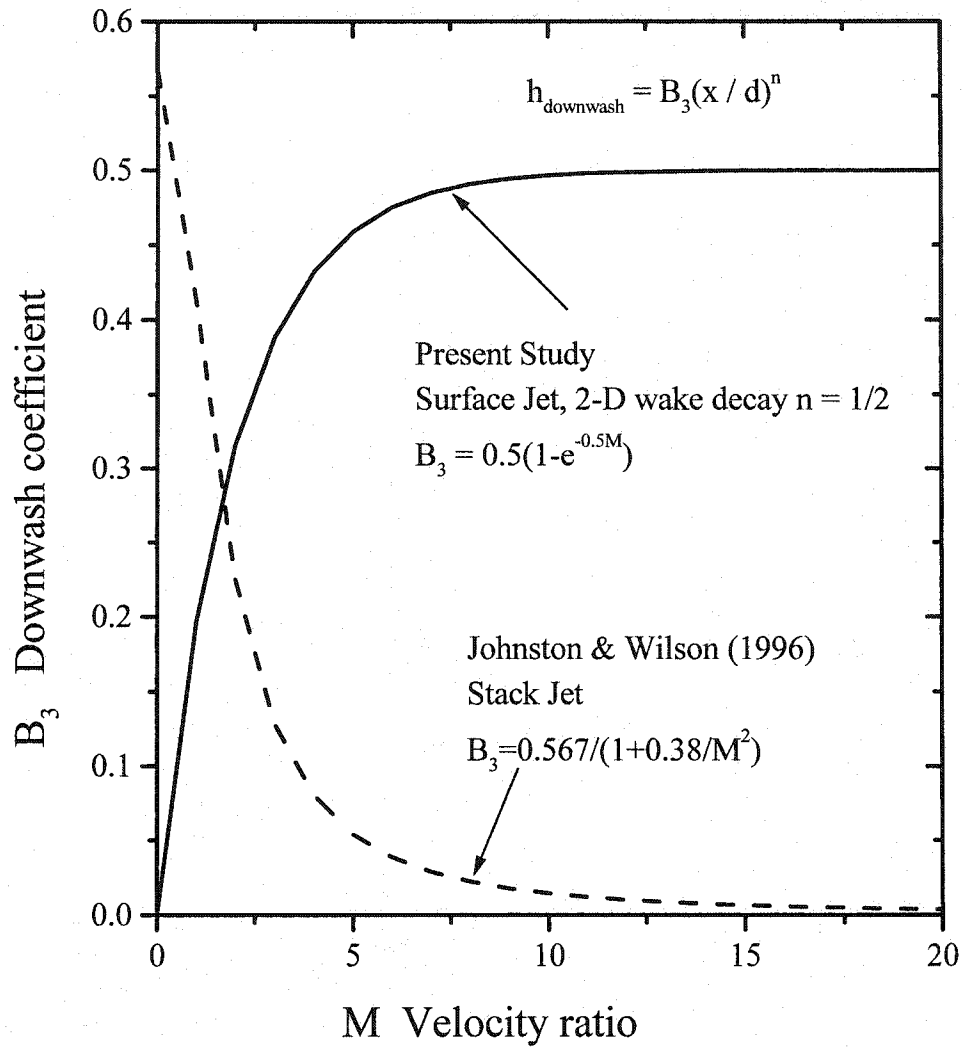


Figure 6.10 In the present study the downwash correction coefficient in Equation 2.50 increases exponentially with increasing velocity ratio.

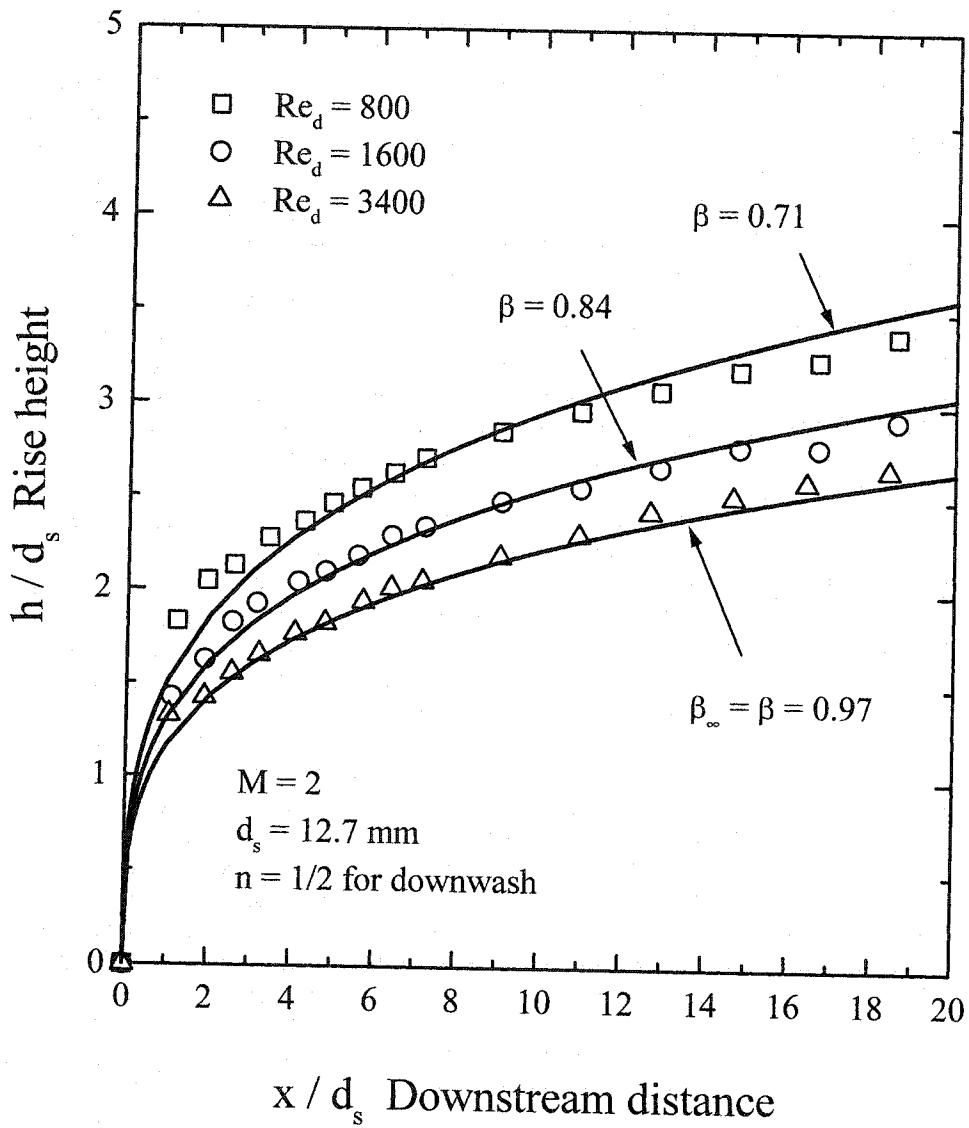


Figure 6.11 Large source comparison between experimental data and the plume rise equation with downwash correction (Equation 6.2), with $B_3 = 0.32$.

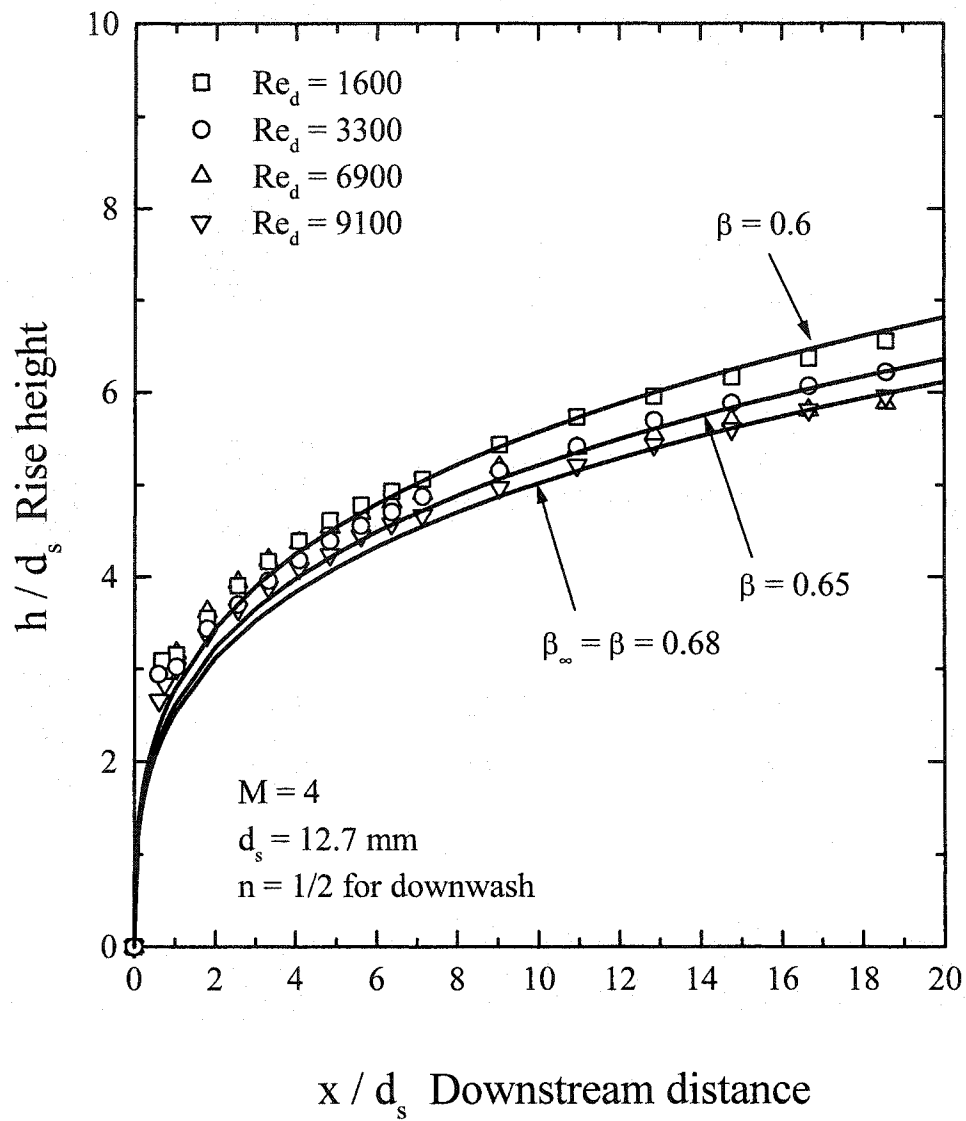


Figure 6.12 Large source comparison between experimental data and the plume rise equation with downwash correction (Equation 6.2). $B_3 = 0.43$

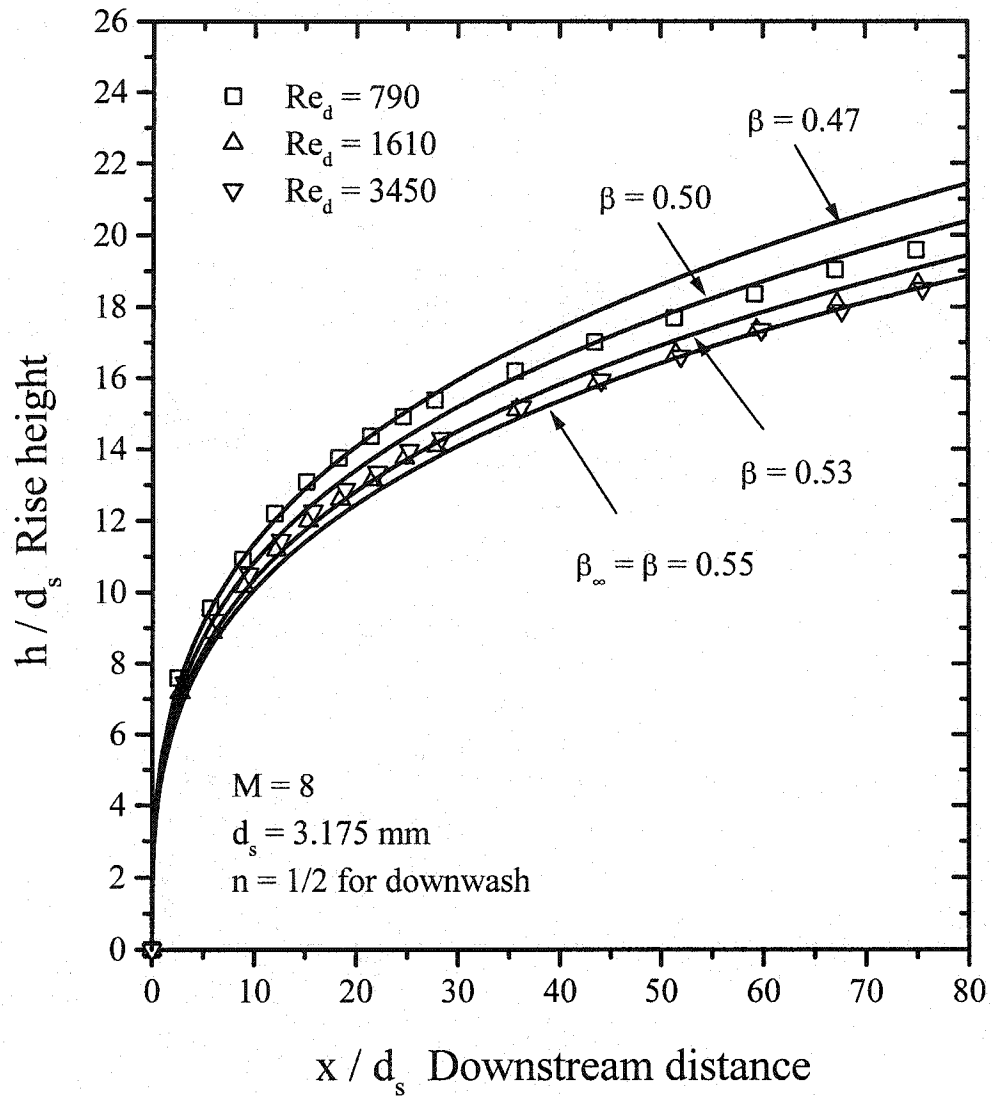


Figure 6.13 Small source comparison between experimental data and the plume rise equation with downwash correction (Equation 6.2), $B_3 = 0.49$.

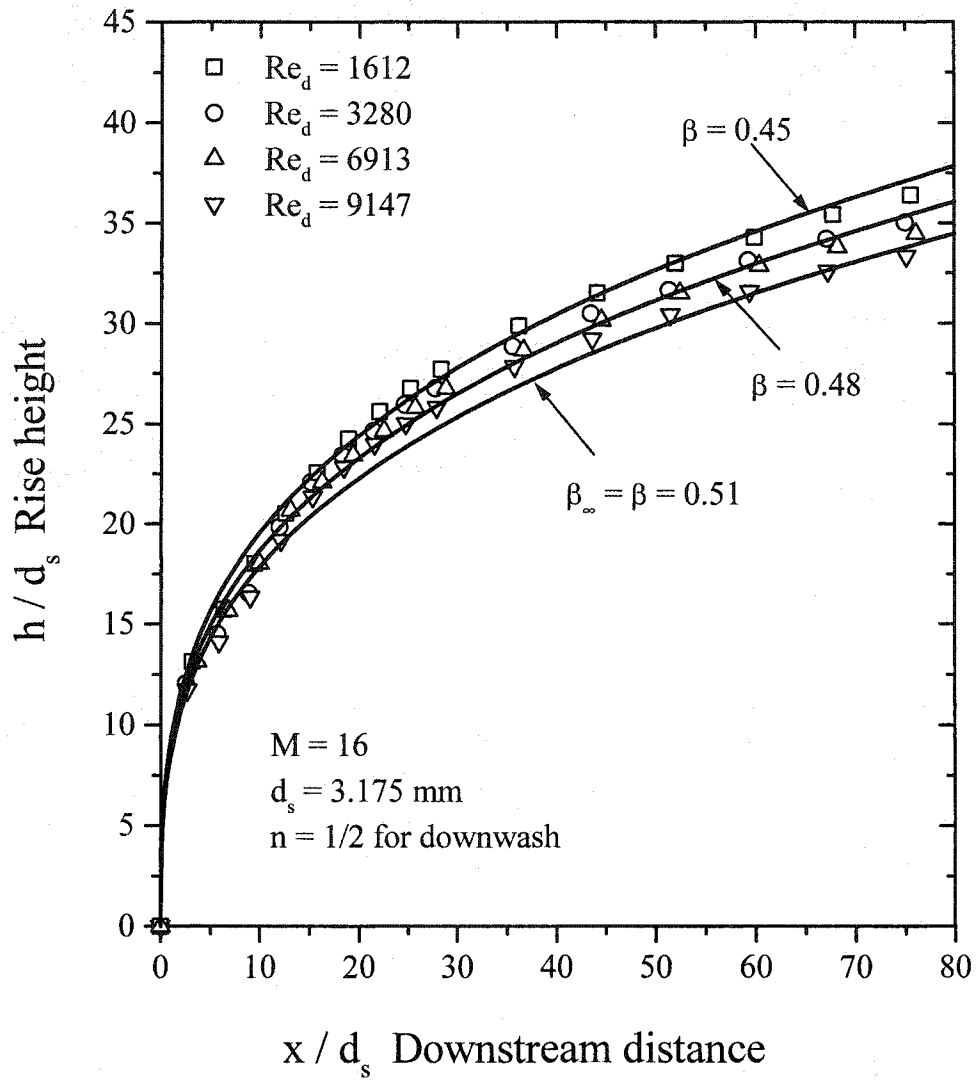


Figure 6.14 Small source comparison between experimental data and the plume rise equation with downwash correction (Equation 6.2), $B_3 = 0.50$

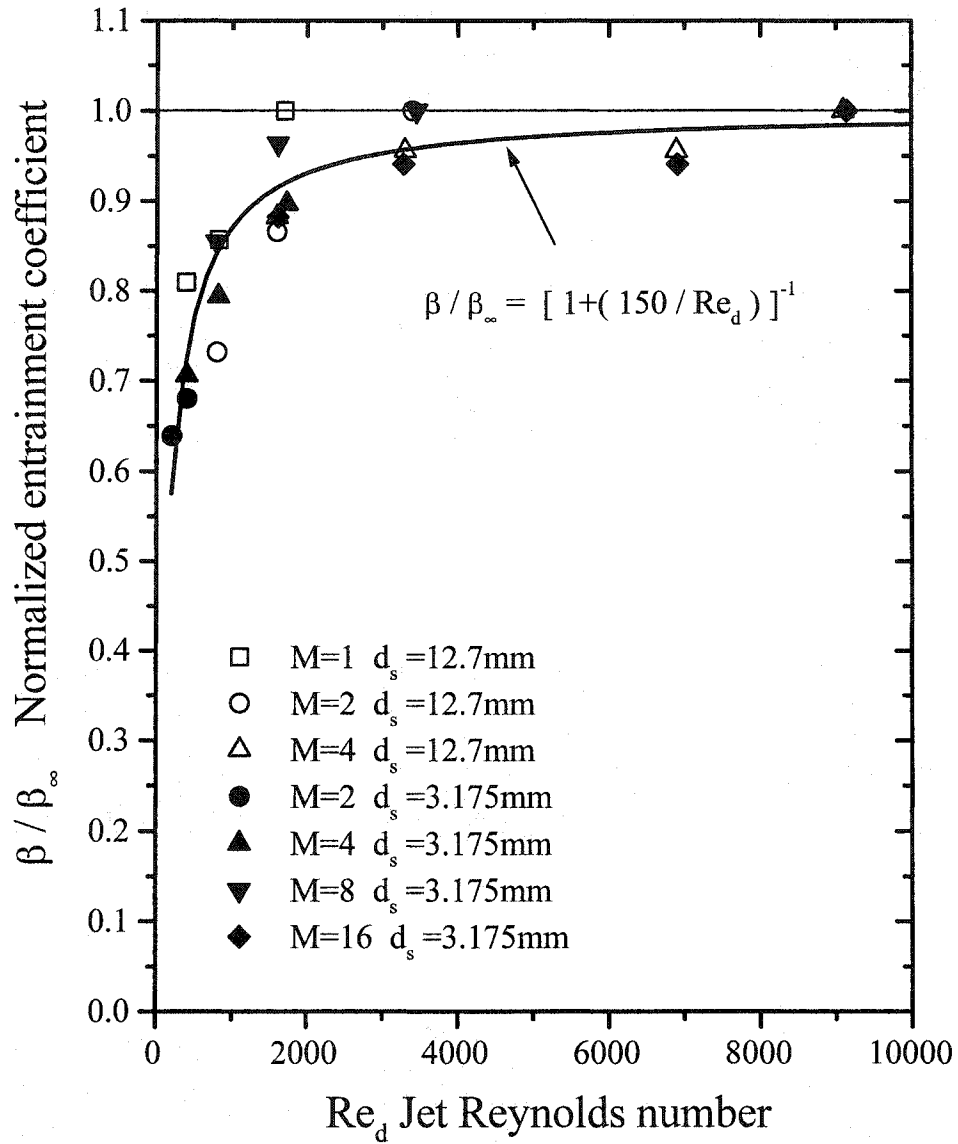


Figure 6.15 Effect of Reynolds number on entrainment coefficient normalized by the high Reynolds entrainment coefficient β_{∞} at the largest measured Re_d for that M .

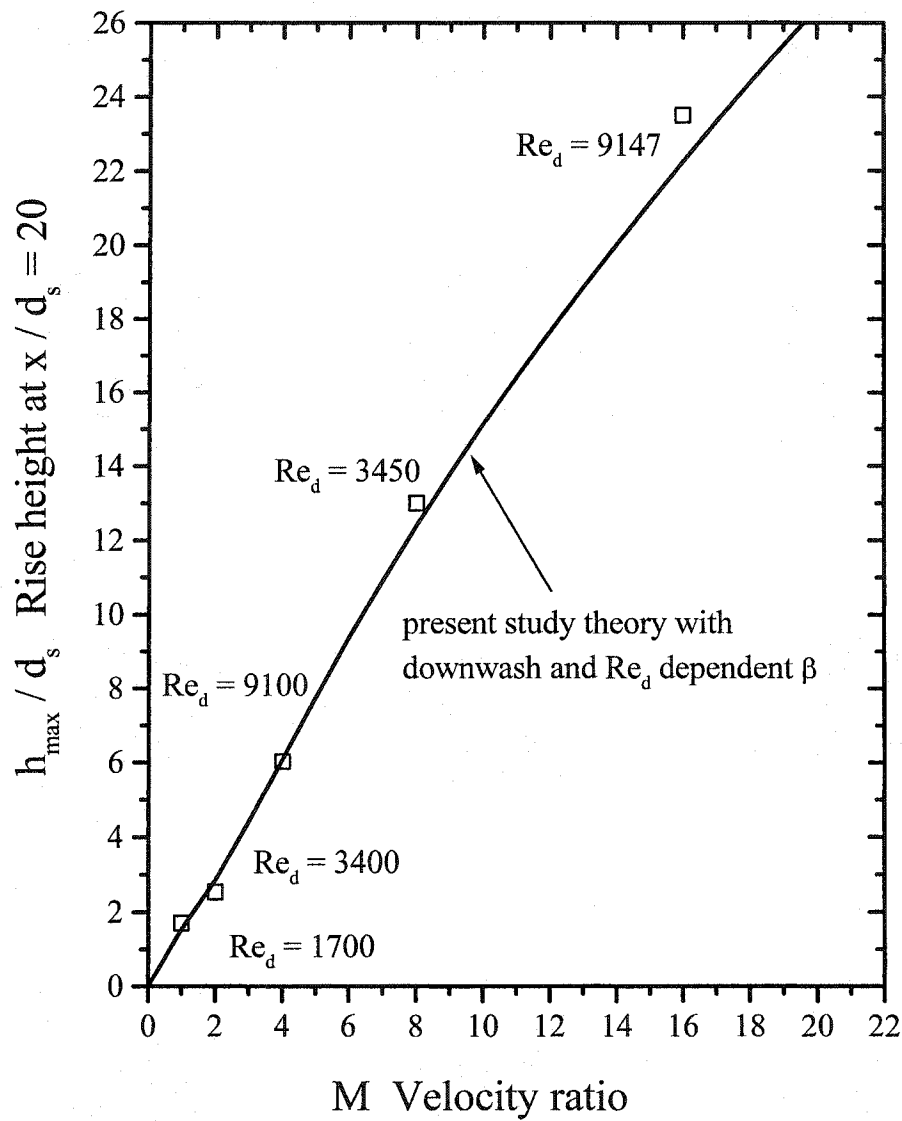


Figure 6.16 Plume rise height increases with the increase in the velocity ratio. The measured and predicted height are at the maximum experimental Reynolds number shown besides the data point. $h_{\max}/d_s = (15\beta^{-2} M^2)^{1/3} - 4.5B_3$. Note that because β varies with M , h_{\max} varies approximately linearly as $M^{1.0}$ rather than as $M^{2/3}$.

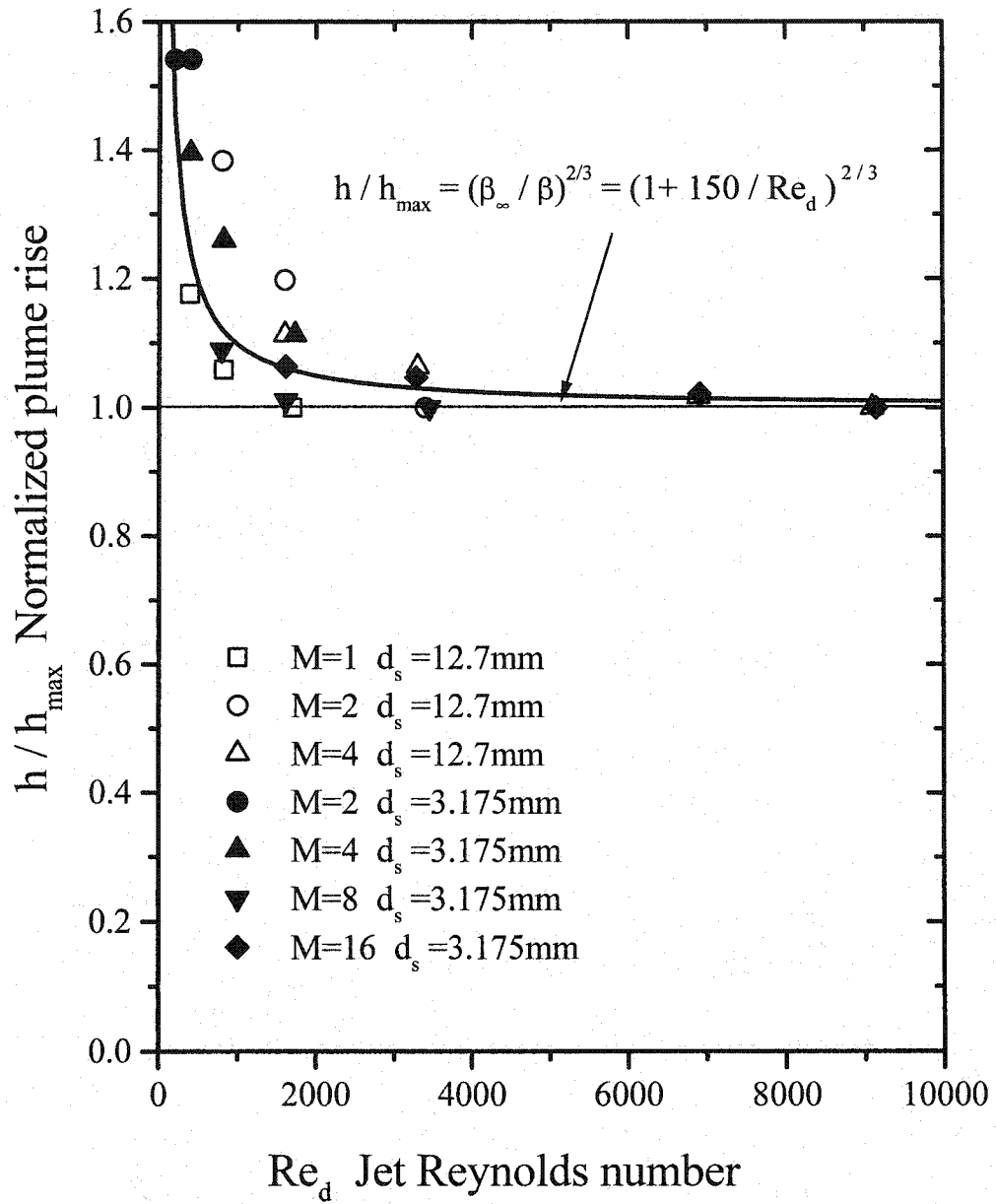


Figure 6.17 Effects of Reynolds number on plume rise.

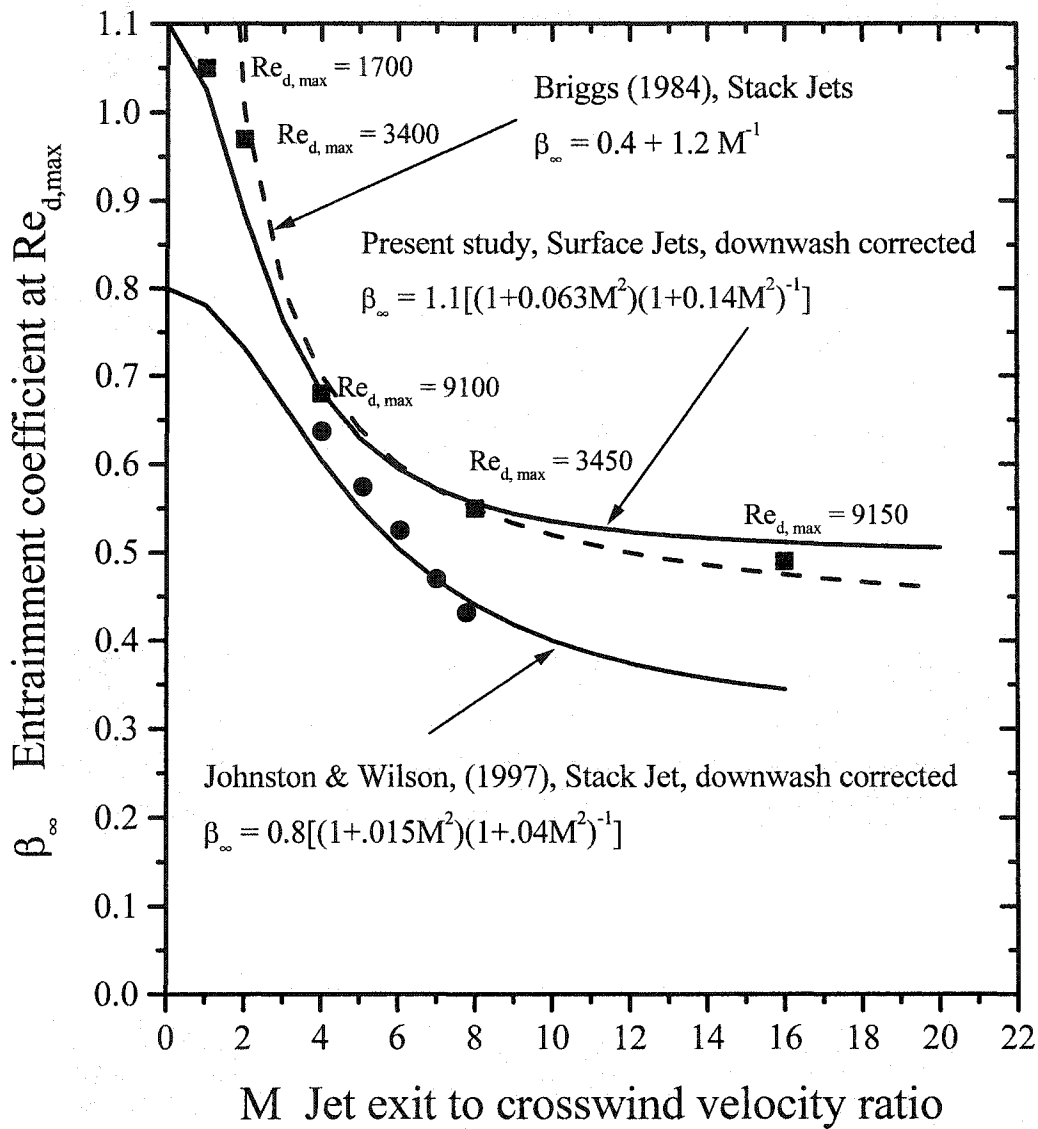


Figure 6. 18 Entrainment coefficient decreases as velocity ratio M increases. Measurements of Johnston and Wilson (1997) shown as solid circle; present study as solid squares.

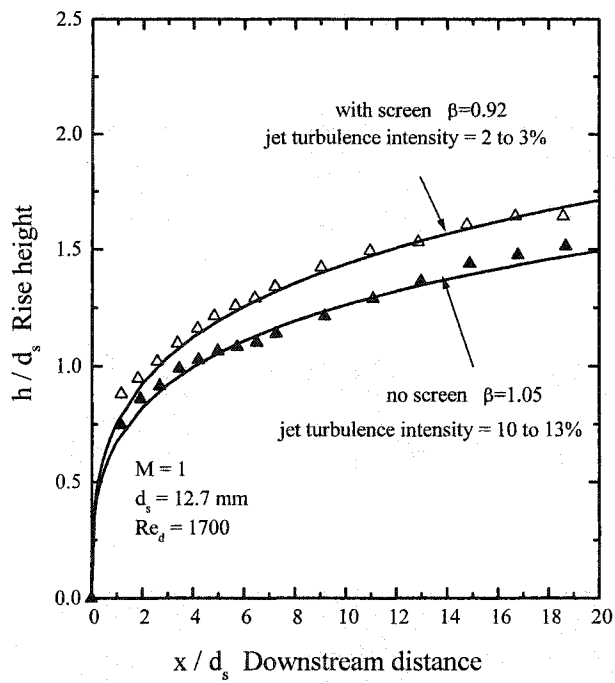
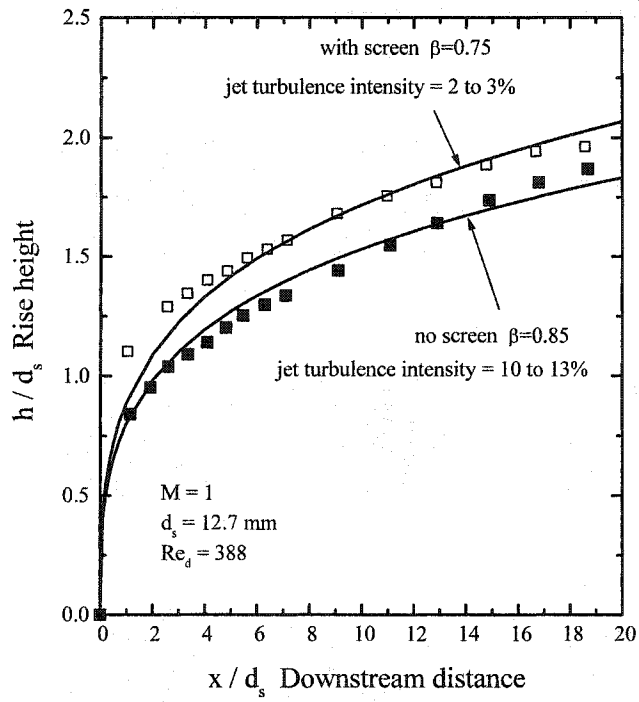


Figure 6.19 Effects of jet turbulence on the plume trajectory.

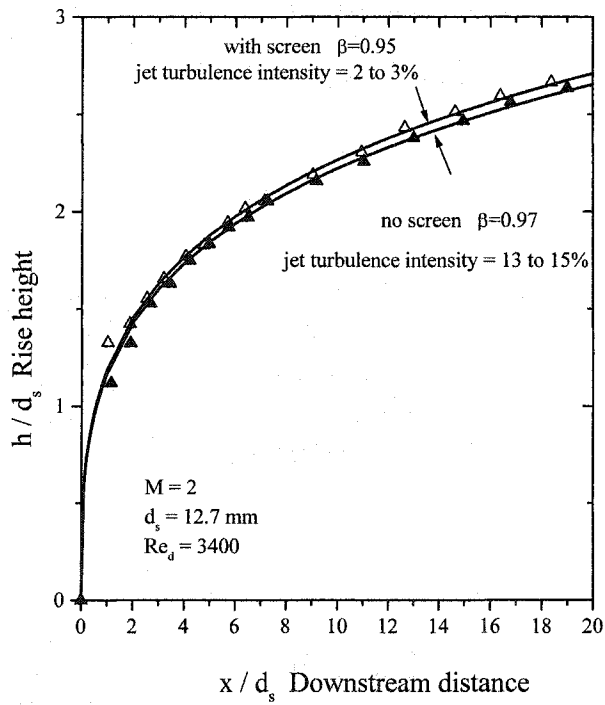
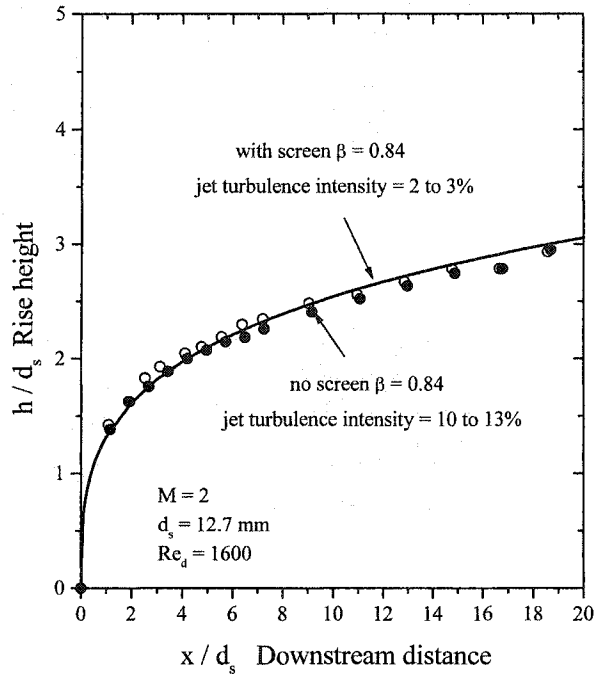


Figure 6.20 Effects of jet turbulence on the plume trajectory.

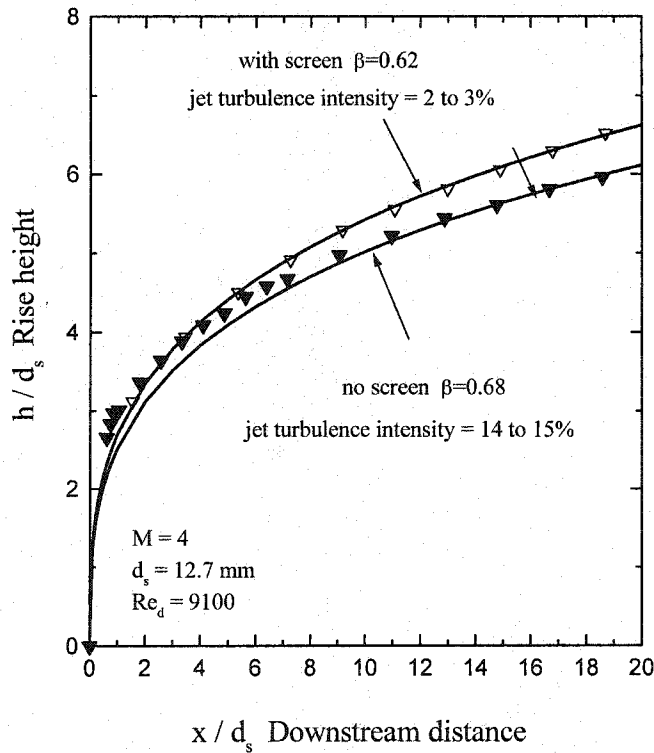
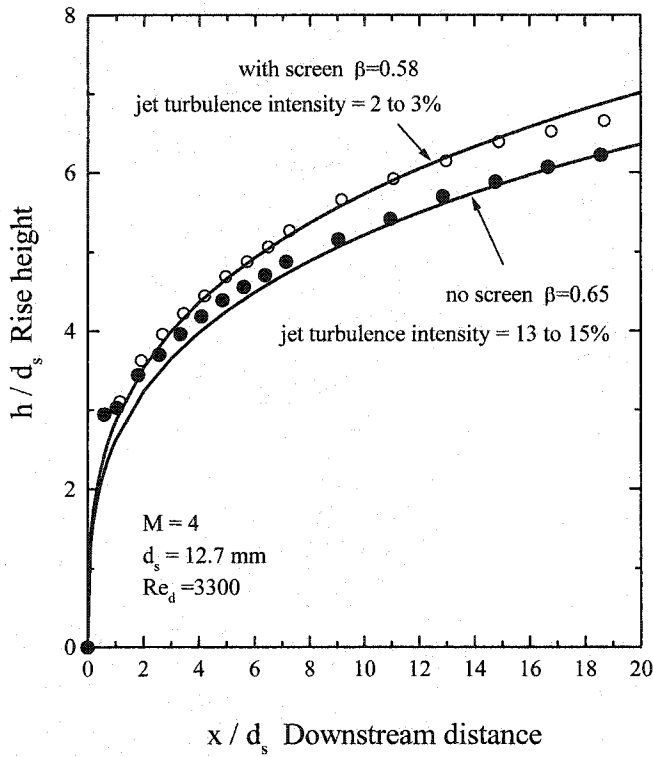


Figure 6.21 Effects of jet turbulence on the plume trajectory.

Table 6.1 List of Flow Visualization Experiments

	Source diameter d_s , mm	Reynolds number Re_d	Velocity Ratio M	Number of instantaneous image	
1	12.7	390	1	200	*
2	12.7	820	1	200	*
3	12.7	1700	1	200	*
4	12.7	800	2	200	*
5	12.7	1600	2	200	*
6	12.7	3400	2	200	*
7	12.7	1600	4	200	*
8	12.7	3300	4	200	*
9	12.7	6900	4	200	*
10	12.7	9100	4	200	
11	12.7	390	1	1200	*
12	12.7	9100	4	1200	
13	12.7	820	1	1800	
14	12.7	1700	1	1800	
15	12.7	800	2	1800	
16	12.7	1600	2	1800	
17	12.7	3400	2	1800	
18	12.7	1600	4	1800	
19	12.7	3300	4	1800	
20	12.7	6900	4	1800	
21	12.7	9100	4	1800	
22	12.7	390	1	2400	
23	12.7	9100	4	2400	
24	3.175	100	1	1800	*
25	3.175	200	1	1800	*
26	3.175	430	1	1800	*

	Source diameter d_s , mm	Reynolds number Re_d	Velocity Ratio M	Number of instantaneous image	
27	3.175	200	2	1800	*
28	3.175	400	2	1800	*
29	3.175	865	2	1800	*
30	3.175	400	4	1800	*
31	3.175	820	4	1800	*
32	3.175	1,730	4	1800	*
33	3.175	790	8	1800	
34	3.175	1,610	8	1800	
35	3.175	3,450	8	1800	
36	3.175	1,612	16	1800	
37	3.175	3,280	16	1800	
38	3.175	6,913,	16	1800	
39	3.175	9,147	16	1800	

* data taken but not on thesis figures

Chapter 7

Summary, Conclusions and Recommendations

7.1 Summary and conclusions

The primary objective of this research was to determine Reynolds number effects on plume trajectory from scaled-down water jets in a water channel crossflow. In order to study these effects, a large scale and a small scale model of a vertical surface jet from turbulent source were designed, built and tested over a wide range of Reynolds numbers in water channel experiments.

7.1.1 Plume rise and downwash model

In Chapter 2, the plume rise model used in this thesis was developed and an equation for the rise of a plume was derived. The key approximations used in the model were that

- The plume is "fully bent-over" with its axis parallel to wind direction for its entire rise; and has a circular cross section in the plane perpendicular to its axis.
- The density difference between the plume fluid and the ambient fluid is negligible (no buoyant plumes).
- The free stream (crossflow) velocity is constant, and the bent-over plume is carried downstream at the ambient fluid speed, U_a .
- Plume trajectory is not affected by the ambient turbulence.
- Entrainment coefficient, β , is the same constant for all plume cross-section locations.

The effects of trajectory-averaged entrainment coefficient on predicted plume trajectories were considered. A physically realistic spatially varying downwash velocity W_d model is introduced in the plume rise equation. The physical model for observed downwash is that the low-pressure area behind the plume affects the plume's ability to rise. The emerging vertical jet produces a low-pressure wake, which acts like an obstacle in the path of the ambient fluid.

7.1.2 Experimental methods and techniques

In Chapter 3, the experimental method and equipment used to simulate and measure the plume trajectory and velocity profiles were discussed. Details of the water channel facility, the Laser Doppler Velocimeter and the methods used to measure the jet velocity profiles and turbulence intensity were discussed. Jet trajectory measurement techniques were explained using a laser sheet lighting dye trace fluorescence flow visualization technique. Images were collected by a Hitachi KP-M1 CCD monochrome (black and white) video camera. The analog signal from the camera was digitized by a computer video board (Matrox Pulsar version 1.0). Each of these techniques provided valuable data such as mean velocity, turbulence intensity and plume centerline concentration.

7.1.3 Design of a turbulent jet source

In Chapter 4, a turbulent jet source was developed to produce a turbulent jet with a flat exit velocity profile that was relatively independent of the jet Reynolds number. The objective was to design a source with an easy reproducible inner geometry, which would be easy to design at any scale to produce the same jet exit profile and turbulence

intensity regardless the size of the source and the flow rate. In the present study, several different design options were built and tested. Simplicity was an important factor in the source design because with a simple design it was easy to build a larger or smaller source with exactly the same geometry. The results from the large and the small source were compared to see if the scaling geometric of the source mixing chamber and inlet distribution plenum had any effects on the jet properties. The jet produced by the source had approximately 10-15% turbulence intensity as the velocity ratio with the cross flow varied from 1 to 16. The jet velocity profiles were weakly dependent on the jet Reynolds number and they were almost the same. The effects of jet turbulence on the mean velocity exit jet profiles were studied for the "large" ($d_s = 12.7$ mm) source. The jet turbulence intensity was reduced from 10-15% to 2-3% without changing the mean velocity exit jet profiles.

7.1.4 Modeling Reynolds Number Effects on Jet Source Turbulence

In Chapter 5, a homogeneous mixing chamber model was developed to predict the turbulence intensity in the jet coming out of the turbulent source. Reynolds number behavior of dissipation model was discussed and that dissipation model was applied to mixing chamber. The values obtained from this model were compared with the experimental data measured in the water channel, and to the data available in the literature. In the mixing chamber dissipation model in the present study, the ratio of the viscous dissipation constant to the inertia constant, $B_{viscous}/B_{inertia}$, was about 6, well within the range from 2.0 to 40 for that ratio found elsewhere in the literature. The coefficient of area contraction of the incoming jets was estimated as $C_c = 0.64$ for the

large inlet holes ($d_{in} = 6.35$ mm, 1 diameter long) into the mixing chamber and $C_c = 1.00$ for the small inlet holes ($d_{in} = 3.175$ mm, 2 diameter long) into the mixing chamber.

7.1.5 Comparison of plume rise model to data

Chapter 6 presented the analysis of the plume rise model. The plume rise model was compared with the experimental data. It was found that the jet exit Reynolds number Re_d , downwash, jet to crossflow velocity ratio and air entrainment coefficient had interrelated effects on plume rise. In this thesis, an entrainment coefficient, which is the function of the velocity ratio and the jet Reynolds number, was used. The experimental data clearly shows that the plume experiences downwash along its entire trajectory. The downwash velocity model was robust in its prediction of the plume trajectories, matching the experimental data very closely. Downwash coefficient was found to be a function of velocity ratio. Reynolds number effects on the plume trajectory were studied. A discussion of the effects of the Reynolds number on the entrainment coefficient and plume rise was conducted.

At low Reynolds number, $Re_d = 200$ to 4000 , there was a 40% increase in the entrainment coefficient but by $Re_d \geq 4000$ the increase in entrainment coefficient was only 2%. In the higher Reynolds number range, Reynolds number effects are negligible on the plume trajectory and at very low Reynolds numbers entrainment coefficient is a strong function of Re_d . Similarly, at lower Reynolds number, such as $Re_d = 200$ to 4000 , there was 50% decrease in the plume rise but at $Re_d \geq 4000$ the decrease is only 5%. It was concluded from these results that for $Re_d > 4000$, viscous effects have a negligible

effect on plume rise at a fixed velocity ratio M . Jet exit to crosswind velocity ratio effects on entrainment coefficient were studied.

Effects of initial turbulence on the plume trajectory were studied by reducing the initial turbulence in the jet from 10%-15% to 2%-3% with a fine mesh exit screen without changing the jet velocity profile. The results show that reducing the initial turbulence in the jet without changing its velocity profile causes a less than one source diameter increase in the plume trajectory rise.

7.2 Recommendations

- The strong surface downwash effects on the surface jets should be incorporated in the current regulatory dispersion models for jet released hazard assessment.
- In future a more thorough study of the inside geometry of the turbulent jet source should be performed to quantify its effects on the jet velocity profiles and turbulence intensity.
- Concentration measurements should be made to calculate the added mass acceleration effects on entrainment coefficient. Further study should be done to collect the data, which would be useful for the dilution calculations.
- A complimentary study should examine the Reynolds numbers effects on plume trajectories from a vertical stack source.

References

- Alton, B. W., Davidson, G. A. and Slawson, P. R., (1993), Comparison of measurement and integral model predictions of hot water plume behaviour in a cross flow. *Atmospheric Environment*, 27A, 589-598.
- Andreopoulos, J. and Rodi, W., (1984), Experimental investigation of jets in a crossflow, *J. Fluid Mech.*, 138, 93-127.
- Briggs, G.A. (1975), *Plume Rise Predictions. Lectures on air pollution and environmental impacts analysis*, D.A. Haugen, Ed., American Meteorology Society, Boston, 59-111.
- Bryant, L.W. and Cowdrey C.F., (1955), Effects of velocity and temperature of discharge on the shape of smoke plumes from a funnel or chimney experiments in a wind tunnel, *Proc. Inst. Mech. Engrs.*, 169, 371-384.
- Callaghan, E.E, and Ruggeri, R.S., (1951), A general correlation of temperature profiles downstream of a heated air jet directed perpendicularly to an air stream, NACA TN 2466.
- Davidson, G.A., (1989), Simultaneous trajectory and dilution predictions from a single integral plume model, *Atmospheric Environment*, 23, 341-349.
- Davidson, G.A. and Slawson, P.R., (1982), Effective source flux parameters for use in analytical plume rise models, *Atmospheric Environment*, 16, 223-227.
- Escudier, M.P. and Maxworthy, T. (1973), On the motion of turbulent thermals, *J. Fluid. Mech.*, 61, 541-552.
- Fabris, Ian, (1998), M.Sc. Thesis, University of Alberta, Edmonton, Alberta.
- Fay, J.A., Escudier, M.P. and Hault, D.P., (1970), A correlation of field observations of plume rise. *Journal of the Air Pollution Control Association*, 20, 391-397.
- Fric, T.F. and Roshko, A. (1994), Vortical structure in the wake of a transverse Jet. *Journal of Fluid Mechanics*, 279, 1-47.
- Haniu, H. and Ramaprian, B.R., (1989), Studies on two dimensional curved nonbuoyant jets in cross flow. *Trans. ASME I : J. Fluids Eng*, 111, 78-86.
- Hinze J.O., (1975), *Turbulence*, Second edition, McGraw Hill.

- Hoehne, V. O., and Luce, R. G., (1970), The effects of velocity, temperature and molecular weight on flammability limits in wind-blown jets of hydrocarbon gases. American Petroleum Institute, 56-70, 1057-1081.
- Hoult, D.P., Fay, J.A. and Forney, L.J. (1969), A Theory of plume rise compared with field observations. Journal of the Air Pollution Control Association, 19, 585-590.
- Hoult, D.P., and Weil, J.C., (1972), Turbulent plumes in a laminar cross flow, Atmospheric Environment, 6, 513-531.
- Jimenez, J., Wray, A.A., Saffman, P.G. and Rogallo, (1993), R.S.. The structure of intense vorticity in homogeneous isotropic turbulence, Journal of Fluid Mechanics. 255,65.
- Johnston, C.R., (1996), M.Sc. Thesis, University of Alberta, Edmonton, Alberta.
- Johnston, C.R. and Wilson, D.J., (1997), A vortex pair model for plume downwash into stack wakes. Atmospheric Environment. 31, 13-20.
- Kamotani, Y. and Greber, I., (1972), Experiment on a turbulent jet in a cross flow., AIAA J. 10:1425-1429
- Keffer J. F. and Baines W. D. (1963), The round turbulent jet in a cross wind, J. Fluid Mech. 15, 481-496.
- Lakehal D., Theodoridis G.S. and Rodi W., (2001), Three dimensional flow and heat transfer calculations of film cooling at the leading edge of a symmetrical turbine blade model. Int. J. of Heat and fluid flow, 22, 113-122.
- Majeski, A.J., (2000), M.Sc. Thesis, University of Alberta, Edmonton, Alberta.
- Morton, B.R., Taylor, G.I., and Turner, J.S., (1956), Turbulent gravitational convection from maintained and instantaneous sources, Proceedings of the Royal Society, Series A, 234, 1-23.
- Neiman, O., (1979) M.Sc. Thesis, University of Alberta, Edmonton, Alberta
- Norris, L.H. and Reynolds, W.C., (1975), Turbulent channel flow with a moving wavy boundary. Report FM-10, Dept. of Mech, Eng., Stanford University.
- Patrick, M. A., (1967), Experimental investigation of the mixing and penetration of a round turbulent jet injected perpendicularly into a transverse stream, Trans. Instn. Chem. Engrs.. 45,16-31.

- Pratte, B. D., and Baines, W. D., (1967), Profiles of the round turbulent jet in a cross flow, Proceedings of ASCE, Journal of Hydraulic Division. 93:53-63.
- Rodi, W. and Schevere, G., (1986), Scrutinizing the $k-\epsilon$ turbulence model under adverse pressure gradient conditions. Journal of Fluids Engineering ASME Trans. 108, 174-179.
- Sergio, Coelho, L. V., and Hunt, J. C. R. , (1988), The dynamics of the near field of strong jets in crossflows, J. Fluid Mech., 200, 95-120.
- Smith, S. H. and Mungal, M. G., (1998), Mixing structure and scaling of the jet in crossflow, J. Fluid Mech., 357, 83-122.
- Sreenivasan, K.R., (1998), An update on the energy dissipation rate in isotropic turbulence., Physics Fluids, 10, 528-829.
- Snyder, W.H. and Lawson, Jr., R.E., (1991), Fluid modeling simulations of stack tip downwash for neutrally buoyant plumes. Atmospheric Environment, 25A, 2837-2850.
- Walker, D.A, (1987), A fluorescence technique for measurement of concentration in mixing liquids. J. of Physics E: Scintific Instruments. 20, 86-94.
- Wang, L.P., Chen, S, Brasseur, G.J. and Wyngard J.C., (1996), Examination of hypothesis in the Kolmogorov refined turbulence theory through high resolution simulations. Journal of Fluid Mechanics. 309,113.
- Weil, J.C. (1988), Plume Rise, Chapter 3 in Lectures in air pollution modelling, A. Venkatram and J.C. Wyngaards Eds., American Metereology Society, Boston, 119-166.
- Yeung, P.K. and Zhou, Y., (1997), On the universality of Kolmogorov constant in numerical simulations of turbulence. Physics Rev. E, 56, 1746.